Nitrogen-Doped Carbon Nanofibers as Pt-Free Catalyst in the Oxygen Reduction Reaction

A study of iron nanoparticles as N-CNF

catalyst on different supports

Anne Helene Barsnes

ABSTRACT

A new approach was tested as nitrogen-doped carbon nanofibers (N-CNFs) were synthesized by using uniformly sized iron nanoparticles (FeNPs) on two different support as their growth catalyst. The N-CNFs are designed as a new catalyst for the oxygen reduction reaction (ORR) in a fuel cell. The aim was to establish working methods for a more homogeneous system which would give the possibility to study the effect of different parameters in-depth in future work.

Different samples of FeNPs were first produced in order to achieve the largest possible size with a homogenous distribution. The N-CNFs were then grown by utilizing the chemical vapor deposition method for 24 h. Both FeNPs and iron nitrate were used to impregnate two samples each with expanded graphite and vulcan carbon as their support. Scanning transmission electron microscopy (S(T)EM) was used to confirm the presence of N-CNFs and determine their structure, whereas x-ray photoelectron spectroscopy was used to confirm the incorporation of nitrogen. Finally, the ORR potential and the reduction pathway were determined by a three-electrode system to be between 0.88 V and 0.92 V for all samples. The system contained a reversible hydrogen electrode as a reference electrode and platinum foil as counter electrode.

Despite the uniform starting system, all samples exhibit great diversity of both N-CNFs structure and size. The most abundant structures were bamboo, fishbone and multi-walled carbon nanotubes. FeNPs impregnated on vulcan carbon (200Vu24h) exhibited both the highest activity and onset potential towards the ORR compared to the other samples. This is attributed to the relative short N-CNFs with bamboo structure and high surface area. The results also indicate that there is no correlation between neither the amount of nitrogen nor amount of quaternary-N and pyridinic-N and the activity above a certain nitrogen amount.

SAMMENDRAG

Platina (Pt) er et mye brukt materiale til katalysatoren for den elektrokjemiske reduksjonen av oksygen (ORR) i brenselceller. Siden Pt både er ustabil i reaksjonen og dyr, har det i løpet av de siste årene blitt forsket på alternative materialer. I denne oppgaven har nitrogendopede karbonnanofibre (N-CNFs) blitt syntetisert fra jern impregnert på karbonbærer, og blitt testet på aktivitet for ORR. Ved å bruke jernnanopartikler (FeNPs) med en homogen størrelsefordeling, har målet vært å lage et homogent startsystem for kartlegging av andre påvirkningsfaktorer.

Forskjellige FeNPs ble produsert, og prøven med den største og mest uniforme størrelsesfordelingen ble brukt som grokatalysator. To prøver med vulcan-karbon som bærer og to prøver med ekspandert grafitt som bærer ble impregnert med henholdsvis de valgte FeNPs og jernnitrat. N-CNFs ble så syntetisert ved hjelp av kjemisk dampavsetning (chemical vapor deposition, CVD) i 24 h. Strukturen og størrelsen av fibrene ble analysert ved hjelp av et elektronmikroskop (scanning transmission electron microscope, S(T)EM) og innlemmingen av kvartært og pyridinsk nitrogen ble bekreftet av røntgenfotonelektronspektroskopi (x-ray photoelectron spectroscopy, XPS). Spenningen og reduksjonsmekanismen ble målt i et tre-elektrode system bestående av en reversibel hydrogenelektrode som referanseelektrode, og platinafolie som motelektrode.

Til tross for det uniforme startsystemet produserte alle prøvene ulike N-CNFs både i struktur og størrelse. De mest vanlige strukturene var bambus (bamboo), fiskebein (fishbone) og flerveggede karbonnanotuber (multi-walled carbon nanotubes, MWCNTs). Begge vulcan-prøvene viste høyere aktivitet enn ekspandert grafitt, og vulcan med impregnerte FeNPs viste både høyest aktivitet og høyest startpotensial. Dette kan forklares ut fra korte N-CNFs med bambusstruktur og høyt overflateareal. Resultatene har også vist at hverken den totale mengden nitrogen eller mengden av henholdsvis kvartært og pyridinsk nitrogen, bidrar til økt aktivitet over et visst nivå.

Preface

This master thesis is has been written on behalf of Department of Chemical Engineering at the Norwegian University of Science and Technology during the spring semester of 2015.

Magnus Rønning has supervised this thesis and is thanked for guidance, support and good words even when nothing was working. Additional thanks is given to both co-supervisors Navaneethan Muthuswamy and Marthe Emelie Melandsø Buan. Navaneethan Muthuswamy has provided much valuable knowledge regarding the S(T)EM and TPO analysis. Marthe Buan performed both the BET and the XPS experiments, and also assisted with the electrochemical measurements. Navaneethan Muthuswamy and Marthe Buan have been a great resource with helping me to interpret and discussing my results together with answering my many questions. Last, Gurvinder Singh is thanked for the in-depth knowledge regarding the iron nanoparticle synthesis, lending me his set-up at NanoLab, and his patience when teaching me the synthesis. All students of the catalysis group are also to be thanked for support, assistance and laughter in stressing times.

I declare that this is an independent work according to the exam regulations of the Norwegian University of Science and Technology.

Trondheim, 8. June 2015

_____

Anne Helene Barsnes

CONTENTS

LIST OF FIGURES

List of Tables

LIST OF ABBREVIATION

BET   Brunauer, Emmet and Teller
CNF   Carbon nanofiber
CNT   Carbon nanotube
CPS   Counts per second
CVD   Chemical vapor deposition
EXAFS   Extended x-ray absorption fine structure
FeNP   Iron nanoparticle
GC   Gas chromatography
MS   Mass spectrum
MWCNT   Multi-walled carbon nanotube
N-CNF   Nitrogen-doped carbon nanofiber
NP   Nanoparticle
ORR   Oxygen reduction reaction
PEMFC   Proton exchange membrane fuel cell
RHE   Reversible hydrogen electrode
RSF   Relative sensitivity factor
S(T)EM   Scanning transmission electron microscope
SWCNT   Single walled carbon nanotube
TGA   Thermogravimetric analysis
TPO   Temperature Program Oxidation
VGCF   Vapour grown carbonfiber
XPS   X-ray photoelectron spectroscopy
XRD   X-ray diffraction

LIST OF SYMBOLS

$at\%$	$\%$	Percentage atomic concentration
B	$\circ$	Width at half-peak height
d_{hkl}	nm	Distance between two adjacent lattice planes
e	C	Electron charge
E_0	V	Standard cell potential
E	V	Cell potential
E_b	V	Binding energy of a photoelectron
E_{kin}	V	Kinetic energy of a photoelectron
EORR	V	Electrochemical onset reduction potential
$e\phi_{spec}$	V	Work function of the spectrometer
ΔG°	$\mathrm{kJ\,mol^{-1}}$	Standard formation energy
G	$\mathrm{kJ\,mol^{-1}}$	Formation energy
hv	V	Energy of a photoelectron
I_i	mA	Current of item i
k		Constant close to 0.9
k_i	$\mathrm{s^{-1}}$	rate constant
L	nm	Size of the crystallites
n		Integer
N	$\%$	Collection efficiency of the ring electrode
N_A	$\mathrm{mol^{-1}}$	Avogadros number
P_0	mmHg	Saturation pressure
P	mmHg	Partial pressure
p_i	Pa	Partial pressure of component i
R	$\mathrm{J\,K^{-1}\,mol^{-1}}$	Gas constant
T	K	Temperature
V_0	$\mathrm{cm^3}$	Volume adsorbed at monolayer coverage
V_a	$\mathrm{cm^3}$	Volume absorbed at P

$wt\,\%$	%	Weight percent
θ	°	Diffraction angle
λ	nm	X-ray wavelength
φ	V	Standard electron potential
χ		ratio of desorption rate constants

CHAPTER 1

INTRODUCTION

The first fuel cell dates back to about 1839, and platinum (Pt) has since then been the preferred catalyst for both the anode and cathode reaction. As a catalyst, Pt is the key role in a working fuel cell. It catalyzes the reaction on the electrode, and thus making the fuel cell working. Despite the age of the fuel cell, the fuel cell has never been fully commercialized, and there are three majors reasons for this: the unsolved catalytic problems regarding the usage of Pt as a catalyst for the ORR reaction, the significant amount of Pt used in the cathode catalyst, and the high cost of Pt. However, with the oil reserves shrinking, fuel cells might provide a good alternative power source in the future. Particular the automobile industry is interested in a fuel cell that is reliable and stable enough to be mounted in a car.

A fuel cell with hydrogen (H_2) and oxygen (O_2) as fuels converts chemical energy to electricity through two major reactions: the hydrogen oxidation at the anode and the oxygen reduction reaction at the cathode. Both the anode and cathode are the electrodes, which combined with an electrolyte compose a fuel cell [1]. Carbon nanofibers (CNFs) are a carbon nanostructure that resembles graphene and they have shown promising results as an alternative catalyst for the oxygen reduction reaction (ORR) in fuel cell.

Based on the kinetics, it is the ORR reaction that is the slowest reaction and hence the targeting goal when optimizing the energy conversion efficiency of a fuel cell. Additionally, the Pt electrodes are vulnerable to both time-dependent drift and CO activation, making them desirable to replace [2]. With the worlds reserves of Pt estimated to consist of about $40\,000\,t$, 667 millions cars could be supplied with fuel cells by assuming an average amount of $61\,g$ Pt per $85\,kW$ fuel cell. Even by reducing the amount of Pt used per fuel cells, all Pt will not be available for automotive fuel cells and only about 180 tons is produced per year [1]. Hence, a

scarcity of Pt is inevitable and with the recorded problems with sluggish kinetics, low selectivity and poor durability the research for a new ORR catalyst has naturally expanded over the last couple of years [3].

Discovering the C_{60} fullerene in 1985 marks the start of the research of nanostructured carbon [4]. There are many different carbon nanostructures, but most structures are base on the same structural unit: a single-layer graphene sheet that is either rolled or flat. During the last century, there has been a enormous progress, which is illustrated by the granting of the Nobel price in 2010 to Curl, Kroto and Smalley on their research on graphene. Over the years, the carbon nanostructures have been industrialized and found applications in plastic reinforcement, conductive phase and others. Research has also been conducted to see if they are suitable for other applications, including as a catalyst in fuel cells.

With the understanding that nitrogen-doped carbon nanostructures (N-CNFs) could be used as an alternative catalyst the drive to develop a new catalyst for the ORR has increased furthermore [2]. As the research regarding carbon nanostructures as a catalyst for the ORR reaction is still ongoing, not all parameters and their influence have been fully understood. It has been proven that carbon nanofibers show the best activity when they are dispersed on a support, have an active metal attached and are doped with nitrogen. During the last years, it has been accepted that iron (Fe) is the metal that promotes the best activity together with the incorporation of certain nitrogen groups [3]. As a results, the new catalysts are often refer to metal-free catalyst even though they contain metal.

In 2012 the EU granted the project FREECATS: Doped carbon nanostructures as metal-free catalysts funding from the 7th Framework Program "to develop new metal-free catalysts, either in the form of bulk nanomaterials or in hierarchically organized structures both capable to replace traditional noble metal-based catalysts in catalytic transformations of strategic importance". The project is split into five workspaces, including a work space for catalytic testing and optimization with the main object to test materials developed in an earlier stage (N-CNFs) for the ORR for use in a proton exchange membrane fuel cell (PEMFC) [5].

This thesis is part of the mentioned workspace and has been focusing on comparing the effect of using iron nanoaparticles (FeNPs) and iron nitrate as the metal source in the synthesis of N-CNFs. By using iron nanoparticles, it is possible to controll their size and thus creating a homogeneous and well characterized starting system for the synthesis. The hypothesis is, that this system will create uniform N-CNFs, giving the possibility to isolate the effects of other parameters and studying them in-depth.

The first chapter provides a general introduction of the theory of fuel cells, iron

nanoparticles, carbon nanofibers and the effect of nitrogen-doping and iron. Then follows an introduction to the theoretical aspects behind the characterization techniques used, before the experimental part and results are presented. Last, a discussion briefly discusses the results obtained and gives recommendations for further work.

Appendix A gives a numerical example of the calculation of the iron loading, Appendices B and C provides detailed graphs for each sample from the temperature programmed oxidation and x-ray diffraction respectively. Appendix D illustrates enlarged particle size distributions that have been compressed in Chapter 5. Appendix E presents additional scanning transmission electron microscope pictures from the samples both before and after growth of the N-CNFs and Appendix F detailed graphs for each sample from the electrochemical measurements. Last, Appendix G gives the risk assessment performed on the experiments conducted at Department of Chemical Engineering, Department of Materials Science and Engineering, and Nanolab.

CHAPTER 2

THEORY

2.1 Fuel cells

In either 1839 or 1842 Sir William Grove described the first fuel cell, a gaseous voltaic battery based on Schönbeins findings, which converted chemical energy stored in compounds into electrical energy. The concept of fuel cells has since been developed further by varying parameters like electrodes, electrolytes, operation temperatures and fuel used. Siemens invention of the dynamo in 1866-1867 put the development of fuel cells on hold as it provided electrical energy more efficiently and on a larger scale. In the 1950's the fuel cell made a comeback within spaceflight, but were soon dismissed as the need of high purity of gases and the highly corrosive liquid electrolytes used proposed too severer challenges. During the oil crisis in the early 1970's the fuel cell gained a new boost, and some of the state-of-art fuel cells were developed. This is a proton exchange membrane fuel cell (PEMFC) and is still a state-of-art fuel cell in use today [1].

In 2011 the EU decided to reduce the CO_2-emission by 80% to 95% according to the 1990 levels within 2050 [6, 7]. This has pushed the demand for developing renewable and CO_2 neutral energy and technology, and fuel cells have been predicted to be one amongst many other promising candidates, as alternatives for the internal-combustion engine within the automobile industry.

There are many different types of fuel cells that all converts chemical energy to electrical energy through mainly different reactions and electrolytes. This report focuses on a PEMFC, and hence only this type of fuel cell is described in detail below.

Proton exchange membrane fuel cells

The proton exchange membrane fuel cell (PEMFC) consist of an anode and cathode (also called electrodes) separated by a membrane, and the concept and components are illustrated in Figure 2.1. Hydrogen (H_2) gas and oxygen (O_2) gas flow over current collectors and are respectively oxidized at the anode and reduced at the cathode. The released electrons from H_2 provide electricity by flowing through an exterior circuit before they reduce O_2 at the cathode and react to form liquid water (H_2O) together with the hydrogen protons (H^+) diffused through the proton exchange membrane (PEM) which is located in the heart of the MEA. Besides being a end product, the liquid water is also used to conduct protons through the membrane and moisturize it. The current collectors are bipolar plates in order to be able to stack cell in series, illustrated in Figure 2.2, and thus create greater voltages than $0.7\,V$ which corresponds to a single cell. A PEMFC is called a low temperature fuel cell that operates at temperatures ranging from $50\,°C$ to $100\,°C$. As mentioned before, a fuel cell converts chemical energy into electricity and has traditionally a high energy conversion efficiency ranging from $40\,\%$ to $60\,\%$. If the waste heat is captured for use, a maximum efficiency of $85\,\%$ can been achieved. This is one of the main advantages of fuel cells, as it is not limited by the Carnot efficiency compared to the lower thermomechanical energy conversion [1, 8, 9].

Reactions - Thermodynamics and Kinetics

When H_2 gas is pumped onto the anode, the gas is oxidized and hence split into its composition electrons and protons as given by reaction (2.1). Since the proton exchange membrane is not electrically conductive and only allows the passing of the conduction of ions, H^+ ions, the electrons are forced through an exterior circuit, creating an electromotive force. Both electrons and protons end up at the cathode where O_2 gas is reduced to form liquid H_2O, reaction (2.2). Reaction (2.2) is often referred to as the oxygen reduction reaction (ORR). The total reaction is displayed by reaction (2.3) and the concept is displayed in Figure 2.1 [1, 8, 11, 12].

$$H_2 \longrightarrow 2\,H^+ + 2\,e^- \qquad \varphi_0 \equiv 0\,V \tag{2.1}$$

$$O_2 + 4\,e^- + 4\,H^+ \longrightarrow 2\,H_2O \qquad \varphi_0 = 1.229\,V \tag{2.2}$$

$$2\,H_2 + O_2 \longrightarrow 2\,H_2O \qquad \Delta\varphi_0 = 1.229\,V \tag{2.3}$$
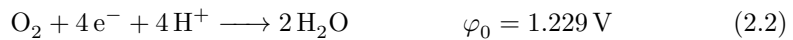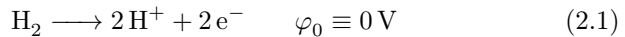
The reaction displayed in (2.2) is called the four-electron pathway. In acidic conditions the ORR can also proceed through a two-electron pathway as shown in reaction (2.4). Oxygen is first reduced to hydrogen peroxide and then further reduced to form H_2O (the last step is not shown in (2.4)) [13]. It is the reaction (2.2) that is desired, as it produces water. In addition H_2O_2 could damage the membrane, and H_2O is easier to handle with as an end produc in comparison to H_2O_2 in a portable fuel cell. H_2O_2

$$O_2 + 2\,e^- + 2\,H^+ \longrightarrow 2\,H_2O_2 \quad \varphi_0 = 0.67\,V \tag{2.4}$$
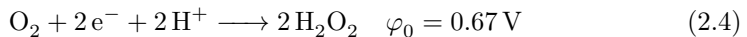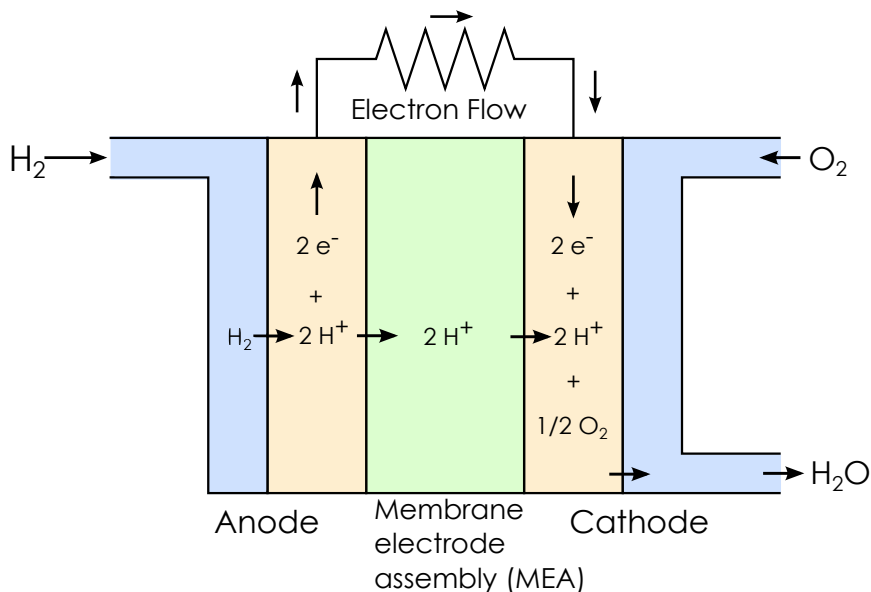
Figure 2.1: A simplified figure of a fuel cell consisting of two electrodes (anode
and cathode) separated by an membrane electrode assembly (MEA).
Hydrogen is oxidized at the anode into electrons and protons. The
electron travel through an exterior circuit providing elecetricity, while
the protons diffuse through the membrane. After the electrons and
the protons have traveled through an exterior circuit and the mem-
brane respectively, they reduce oxygen at the cathode with water as
the end product.

The standard electron potential, φ, for reaction (2.1) is defined to be $0\,\text{V}$ and used
as a reference point for all electrode potentials. $\Delta\varphi_0$ in reaction (2.3) is the differ-
ence between the standard cathode and anode electron and also called the standard
cell voltage E_0. The standard cell voltage or a single hydrogen-oxygen fuel cell is
thus $E_0 = \Delta\varphi_0 = 1.229\,\text{V}$. E_0 is a theoretical value and denotes the voltage when
no electrical energy is withdrawn from the fuel cell. Once electricity is withdrawn,
losses in voltage will occur for several reasons; ohmic losses several places, e.g. in
the porous electrodes, membrane and chemical contact, mass-transfer losses and
kinetic losses due to the occurring reactions. Both the ohmic and the mass-transfer
losses can be addressed through improvements in both the electrodes and the mem-
branes. The kinetic losses are however governed by both the catalyst material and
its structure and the reaction conditions. This results in an operating cell voltage
about $0.6\,\text{V}$ to $0.7\,\text{V}$. The fuel cell voltage and efficiency are also temperature and
pressure dependent, and the optimal conditions are low temperature and low pres-
sure [1, 9].
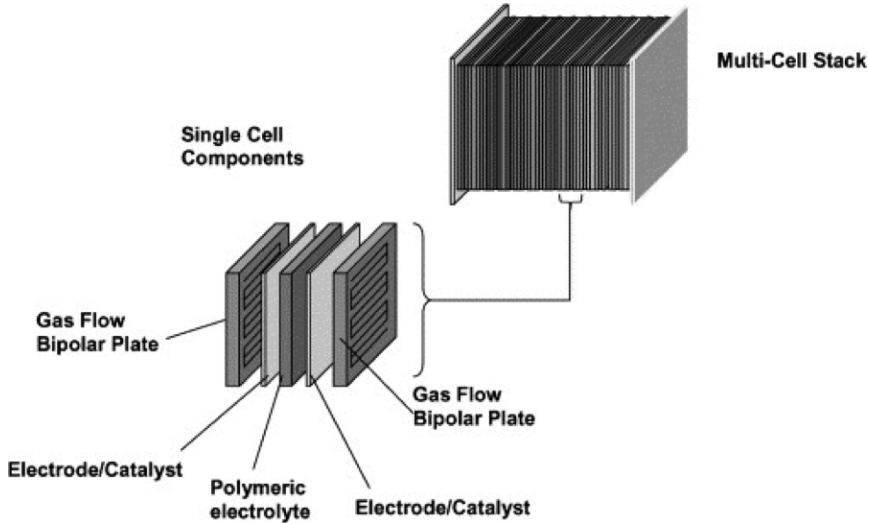
Figure 2.2: Several fuel cells in a stacked arrangement to create a multi-cell stack
fuel cell [10].

The membrane electrode assembly consist of a gas diffusion layer (GDL) and a
catalyst layer, traditionally consisting of Pt supported on carbon (e.g. vulcan car-
bon) on each site separated by a proton exchange membrane at the middle, and
is illustrated in Figure 2.3. An electrode is thereby defined as consisting of a gas
diffusion layer and a catalyst layer, and spans hence from the surface of the gas
channel to the surface of the proton exchange membrane [8]. Comparing the two
electrode reactions (2.1) and (2.2), it is the ORR that limits the conversion mainly
due to kinetic losses at the catalyst layer. As the ORR catalyst layer also demands
the most Pt, the ORR catalyst layer (from now on called catalyst) has been the
main objective when optimizing the fuel cell for commercializing.

Pt as a catalyst material has over the years also shown to be a less reliable catalyst
especially for the oxidation of O_2. It has been reported about sluggish kinetics,
problems due to low corrosion resistance and [14, 11] However, the obtained elec-
trode potential for Pt has long been undefeated attracting researchers to search for
a new catalyst containing less Pt [15, 16].

Ideally, a new catalyst would obtain the same electrode potential for the ORR
as the Pt catalyst. Moreover, the catalyst needs to have a high corrosion resis-
tance, about 40 000 h to 60 000 h, to be commercially competitive. The corrosion
is mainly due to the use of O_2 as a fuel, acid as the electrolyte and oxidation of
the carbon support [15]. By using acid as the electrolyte, mass transfer and ohmic
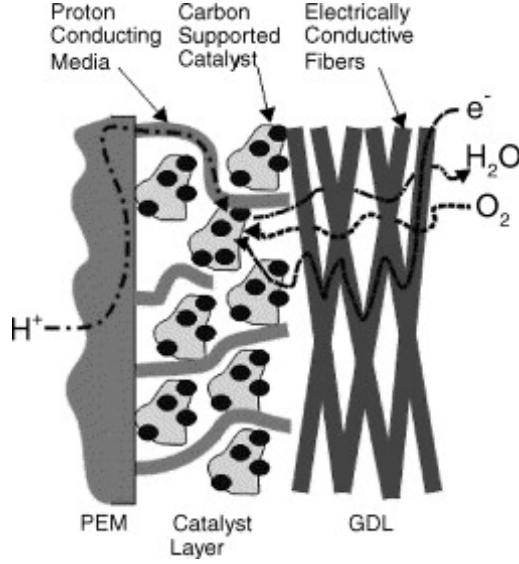
Figure 2.3: The oxygen reduction reaction side of the membrane electrode assembly. The protons (H^+) travel through the polymer electrolyte membrane (PEM) via the proton conduction media into the catalyst layer. There they react together with the electrons, e^-, and the oxygen (O_2) from the gas diffusion layer (GDL) on a carbon supported catalyst to form water (H_2O). The water is then transported out via the GDL [8].

losses can be diminished and only kinetic losses are to be handled [1].

Electrochemical potential

Nernst equation (2.5) calculates the voltage generated by a fuel cell, and is for this fuel cell given by Equation (2.3).

$$\Delta G = \Delta G^\circ + RT \ln \left(\frac{p_{H_2O}}{p_{H_2}\sqrt{p_{O_2}}} \right) \tag{2.5}$$

Here ΔG is the formation energy in $kJ\,mol^{-1}$, ΔG° the free formation energy in $kJ\,mol^{-1}$, R the gas constant, T the temperature in K, and p_i the partial pressure of the component i in Pa. During one circuit, two electrons are passed through the exterior circuit and creating one water molecule. By dividing (2.5) by the charge associated with one mole of water, $-2eN_A$, the potential for the fuel cell can be found as displayed by Equation (2.6) [12].

$$E = E_0 - \frac{RT}{2eN_A} \ln \left(\frac{p_{H_2O}}{p_{H_2}\sqrt{p_{O_2}}} \right) \tag{2.6}$$

Here, E is the cell potential in V, E_0 the standard cell potential in V, e the electron charge which is defined to be $1.6 \cdot 10^{-19}$ C and N_A the Avogadro constant which is defined to be $6.02 \cdot 10^{-23}$ mol^{-1}. As mentioned above, the cell potential for one hydrogen-oxygen fuel cell is 1.229 V and independent of the catalyst used.

2.2 Carbon nanofibers

With the discovery of carbon nanostructures, the search of a new ORR catalyst has advanced and many alternatives have been proposed. Carbon nanofibers (CNFs) are inexpensive to synthesis in comparison with Pt. By additionally doping the CNFs with nitrogen (N-CNFs) and introducing Fe as a transition metal for both growth and activity, the new catalyst has obtained similar activities for the ORR as the Pt catalyst supported on carbon [11, 13, 17]. The catalyst used in this project consist of N-CNFs grown on either iron nanoparticles (FeNPs) or iron particles from iron nitrate. All compounds and their effects are described in this and the following sections.

CNFs is a collective term for many different structures, and consist of carbon atoms that are linear aligned in threads. They exhibit a characteristic with good flexibility and are recognized with an aspect ratio (length/diameter) greater than 100. CNFs are considered as a 1-D form of carbon and both their structure and properties resemble closely other forms of carbon, as e.g. crystalline three-dimensional graphite. Because of their high specific area, flexibility, high mechanical strength, the CNFs have numerous applications as e.g. supports, reinforcing fillers in polymeric composites and photocurrent generators in photochemical cells [18].

Carbon nanofiber structures

As mentioned before, CNFs is a collective term for many different structures. The main types synthesized in this thesis are illustrated in Figure 2.4. As all CNFs are synthesized by the same conditions (Sections 2.5 and 4.3), the only difference among the displayed structures are their chemical structure. The main structures are: carbon nanotubes, platelet, fishbone, bamboo, ribbon, stacked cup and thickened fibers [19].

Figure 2.4a and 2.4b illustrate two type of carbon nanotubes (CNT), single walled nanotube (SWCNT, Figure 2.4a) and multi-walled nanotube (MWCNT, Figure 2.4b). CNTs are a special substructure of CNFs, as they are considered to be an allotropic carbon form: "the graphene layers are rolled up in cyllindrical form with the plane parallel to the fiber growth axis, and no other element besides the transition metal is required to stabilize the strucutre" [19]. In the SWCNT, the tube only consist of one tube, whereas the MWCNT consist of multiple tubes with a diameter ranging from 10 nm to 100 nm.

(a) Single Wall
       NanoTube

(b) Multi Wall
       Nanotube

(c) Platelet

(d) Platelet (Spiral)

(e) Fishbone hollow core

(f) Fishbone Solid

(g) Ribbon

(h) Stacked Cup
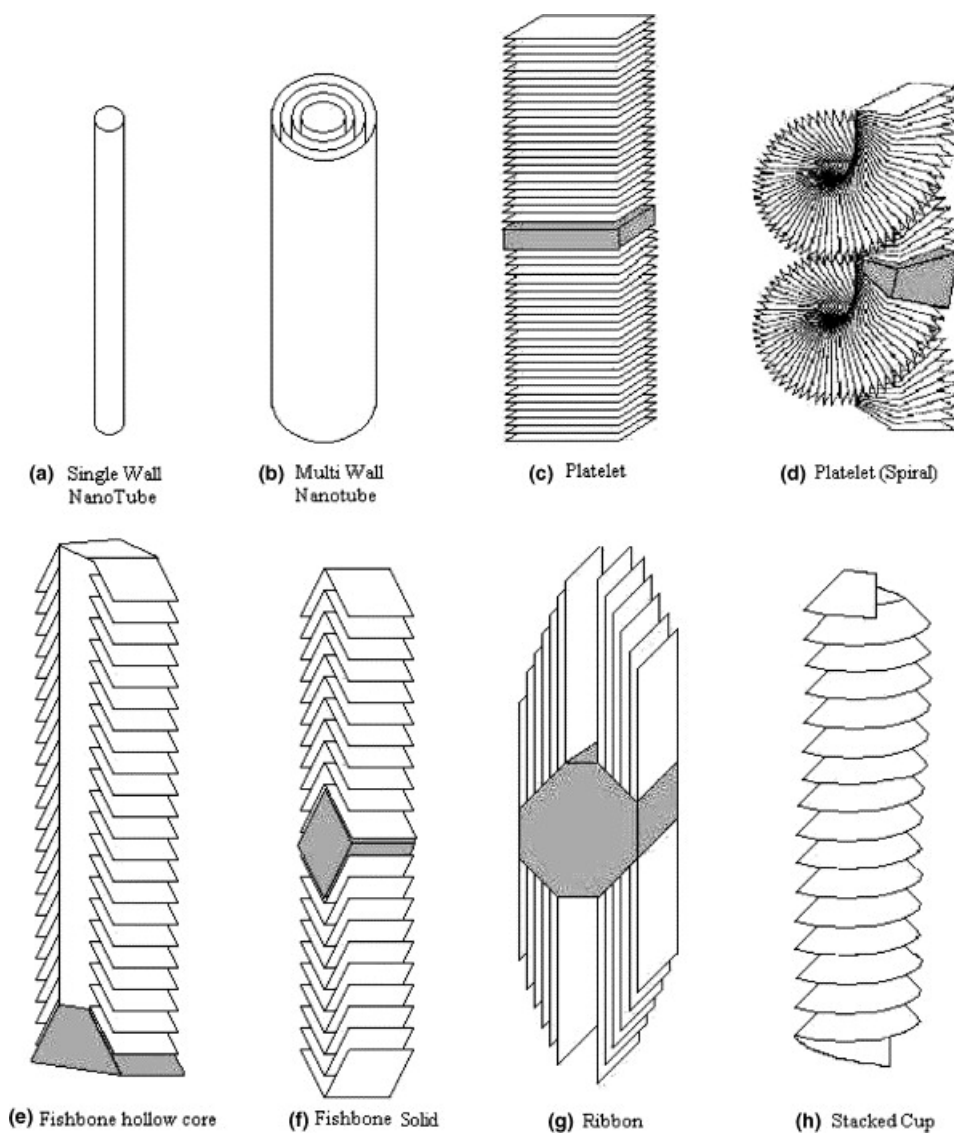
Figure 2.4: Schematic presentation of the the main structures for carbon
nanofibers. The darker particle presents the most likely position of
the transition metal [19].
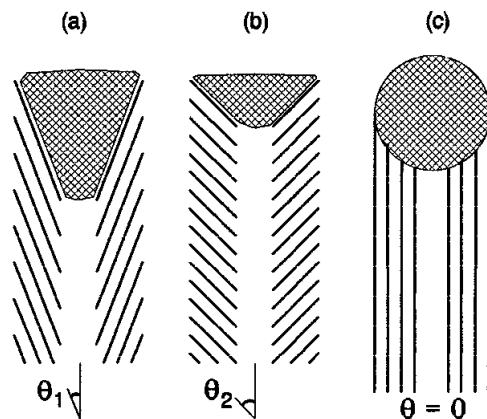
Figure 2.5: Hydrogen concentration in the fiber affects the structure of the grown fiber. An increase in concentration causes the angle between the graphite layers and the fiber growth axis (θ) to increase. (a) and (b) illustrate two fishbone structures with a hollow core and different angles (c) illustrates a multi-walled carbon nanotube [20].

With the platelet structure illustrated in Figure 2.4c, the graphene layers (or platelets) are perpendicular to the fiber growth axis and need to contain a significant amount of both hydrogen and other heteroatom for stabilization. The spiral version of the platelet structure (Figure 2.4d) have the same requirements as the platelet structure. As indicated by both Figure 2.4c and 2.4d the transition metal is often found in the middle of the structure, resulting in bidirectional fibers if the particles are not on a support.

As with the platelet structure, there are also two categories of the fishbone structure: fishbone hollow core (Figure 2.4e) and fishbone solid (Figure 2.4f). Both structure have graphene layers are stacked regular asloped to the fiber growth axis. Although the fishbone solid structure also is referred to as "herringbone", the term fishbone will be used [15]. Both structures are dependent on the presence and concentration of hydrogen: an increase in hydrogen concentration causes the angle between the graphite layers and the fiber growth axis to increase [20, 21]. This phenomena is illustrated in Figure 2.5. The ribbon structure (Figure 2.4g) resembles the carbon nanotube by consisting of parallel graphene layers to the fiber growth axis as the carbon nanotubes, but with unrolled layers in contrast to cylindrical. Due to the similarity, it is are often difficult to distinguish between MWCNTs and the ribbon structure in S(T)EM images.
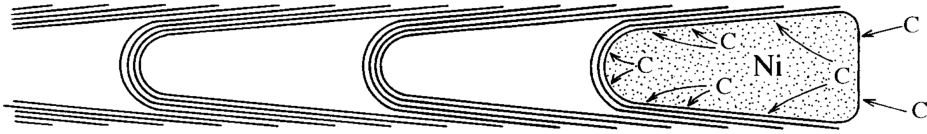
Figure 2.6: Schematic presentation of the bamboo structure including the diffusion pathways of carbon on the transition metal particle [23].

Figure 2.4h illustrates a continuous graphene layer twinned along the fiber growth axis. This results in a twisted cone arrangement along the fiber growth axis with an internal hollow core [19]. The metal particles found in these structures are often found within the fiber with a stretched structure, suggesting that they are molten [22]. As with the ribbon structure, the stacked cup resembles the bamboo in S(T)EM images and it can be difficult to distinguish between them.

Figure 2.6 illustrates another structure which is not illustrated in Figure 2.4, the bamboo structure. This structure resembles the fishbone structure, but the graphene layers are organized in linear hollow compartments instead of regularly asloped to the fiber growth axis. Each compartment consist of about 20 graphene sheets and they are spaced regulary between each other. The metal particle on top of the structure adsorbes the carbon vapour, and the carbon diffuses through the metal particle and out on the bottom and the side. This results in each compartment adopting the drop like shape of the particle on top. After about 20 graphene sheets the metal particle is probably pushed out due to stress accumulated in the compartment from the segregation of carbon [23].

Each structure presented above may be coated with amorphous carbon after it has been formed. The process is taking place by non-catalytic CVD, resulting in thickened carbon nanofibers. Thickened CNFs can grow large in diameter are referred to as vapor-grown carbon fibers (VGCF) when having a diameter greater than $500\,\mu m$.

The structure of the CNFs enables semi-conducting behavior as they have chemically active end planes on both on the inner and outer surfaces of the fibers. This leads to different characteristics compared to carbon nanotubes, making CNFs also usable as supporting materials for catalyst, reinforcing fillers in polymeric composites, and photocurrent generators in photochemical cells [24].
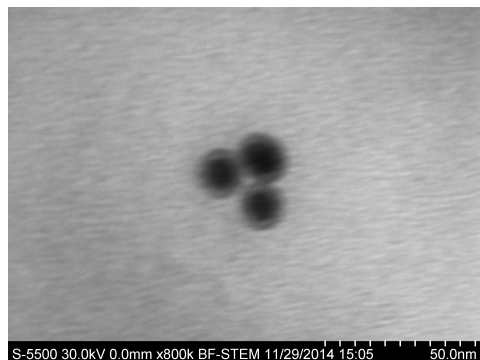
Figure 2.7: An illustration of shell-core FeNPs with an approximate size of about 6 nm to 10 nm.

2.3 Iron nanoparticles

Iron nanoparticles (FeNP) are magnetic particles ranging in the size of 5 nm to 20 nm with an highly symmetric body, illustrated in Figure 2.7. They are produced with a narrow size distribution making them perfect as a catalytic site for creating a homogeneous system in the growth of N-CNFs. FeNPs are used within a wide range of areas like engineering and material science, but are most common in life science fields such as biotechnology and biomedical [25, 26].

There are two main methods to synthesis FeNPs which can either be conducted in gas phase or solution: top down and bottom up. In the top down synthesis bulk material is broken down into nano-sized structures particles, whereas the FeNPs are build up atom-by-atom or molecule-by-molecule in the bottom up synthesis. The bottom up synthesis is more commonly used and includes various methods, among other thermal decomposition, co-precipitation reaction, and hydrothermal and high temperature reactions. It is important to produce FeNPs with a homogeneous composition and narrow size distribution as their properties highly depend on the the magnetic grain size, morphology and composition [25]. In this thesis, the FeNPs have been produced through thermal decomposition, and thus this method is described in detail below.

Thermal decomposition involves the decomposition of an organometallic compound in a high-boiling organic solvent containing a stabilizing surfactant. Common organometallic precursors are among others iron(0)pentacarbonyl ($Fe(CO)_5$), iron-tri-acetylacetonate ($Fe(acac)_3$) and $FeCup_3$ where Cup stands for N-nitrosophenyl-hydroxylamine. $Fe(CO)_5$ consist of an Fe in zerovalence and undergoes an intermediate metal formation before it oxidizes if a mild oxidant is added, whereas $Fe(acac)_3$ leads directly to iron oxides (Fe_2O_3). Common solvent used include

phenyl ether, octadecene, 1-hexadecene and 1-octadecene, and are chosen due to their high boiling temperature [26]. As surfactants fatty acids are used (e.g. oleic acid and olylamine) and they are often adsorbed as a protective layer around the FeNP, creating repulsive forces which are mainly steric. This keeps the single FeNPs separated and preventing them from agglomerating due to their magnetic nature and the van-der-Waals attractive forces . FeNPs with a stabilizing agent around are often referred to be core-shell particles [25, 27].

2.4 Impregnation

Impregnation is a common method used to transfer and disperse the precursor of the catalytically active site, here the FeNP, over the support. The term impregnation is tradionally used by the industrial chemistry and commonly refers to "the contacting of a solid and a liquid phase, and absorption of the latter by the former"[28]. Impregnation is typically used when low loadings are preferable, but it is also sensitive to sintering and impurities.

There are two main impregnation methods, incipient wetness and wet impregnation, and both have the same main requirement - uniformly distribution of the precursor of the catalytically active site in fewest possibles operation to achieve dispersion. In general impregnation is conducted by first dissolving the precursor in a liquid, followed by mixing the liquid and solvent for the precursor to migrate in the pores of the support. Last, the solvent is often eliminated by evaporation due to thermal drying [28].

Incipient Wetness

Incipient wetness, or dry/pore volume impregnation, denotes the method where the same amount of solute as the total pore volume of the support The impregnation is achieved due to capillary forces drawing the solution into the pores, where air is present and will dissolutes as the liquid penetrates the pores. Problems may arises when the pore radius is small and thus the capillary pressure is much larger than the pressure of the entrapped air and keeping it entrapped. If the mechanical strength of the support can not withstand these forces it may collapse. This can be avoided by performing impregnation under vacuum or adding a surfactant to the solution.

Wet Impregnation

Wet impregnation denotes the method were amount of liquid added to the support is limited by the solubility of the metal precursor rather than the pore volume of the support. For powders, wet impregnation can be performed by adding a given amount of excess solution to the support and slowly evaporating the solvent under regular stirring. This method is preferred for poorly soluble compounds.

2.5   Synthesis method of N-CNFs - chemical vapor deposition and growth mechanism

N-CNFs can be grown by many different methods, but the N-CNFs described in this thesis were grown by the chemical vapor depistion (CVD) method. By applying a gaseous carbon containing source at elevated temperature over a transition metal catalyst (e.g.Fe, Co or Ni), the carbon will decompose and produce CNFs as it passes over the metal catalyst. This is illustrated by reaction 2.7, where CO is the carbon source and C denotes the carbon in the different graphene sheets [20].

$$2\,CO = C + CO_2 \tag{2.7}$$

Adding additionally a nitrogen containing gas will produce N-CNFs. The low temperature (below 800 °C), high yield and pure N-CNFs makes the process cheap and its main advantages. However, the N-CNFs are more structurally defective than fibers produced by other methods [29].

There are two main growth mechanisms for the CVD method that have been proposed over the years; tip growth model and base growth model. In both cases, the chosen reaction conditions, the belonging parameters (e.g. dimensions and shape of the metal particles, temperature and the hydrocarbons and gases) and the support interactions influence the growth [30].

The tip growth model describes the case where the top carbon diffuses through the catalytic particle. As the carbon source decomposes on the exposed surface of the metal catalyst it forms a carbon species. From here the carbon dissolves in the particle and diffuses through it until it precipitates at the downside of the particle in the form of graphene filaments, positioning the catalytic particle always on the top of the growing nanofiber. The tip growth model has been observed in cases where the substrate-catalyst interactions were weak and is illustrated in Figure 2.8 [29].

As opposed to the tip growth model, the catalytic particle remains on the growth substrate with the base growth model. Here, the carbon dissolves in the particle and diffuses through it until it precipitates on the top of the metal particle in the form of graphene filaments. This growth model has been observed in cases where the substrate-catalyst interactions were strong [29].

The intensive research on a broad range of alternative catalyst for the ORR reaction has made it somewhat difficult to appoint controlling parameters. Many different materials and techniques varying in both properties (i.e. porosity, surface area, surface functionalities) and parameters (temperature, pressure, time) have been tested, leading to the fact that all aspects regarding the correlation of the carbon, transition metal and nitrogen in terms of growth and activity yet have
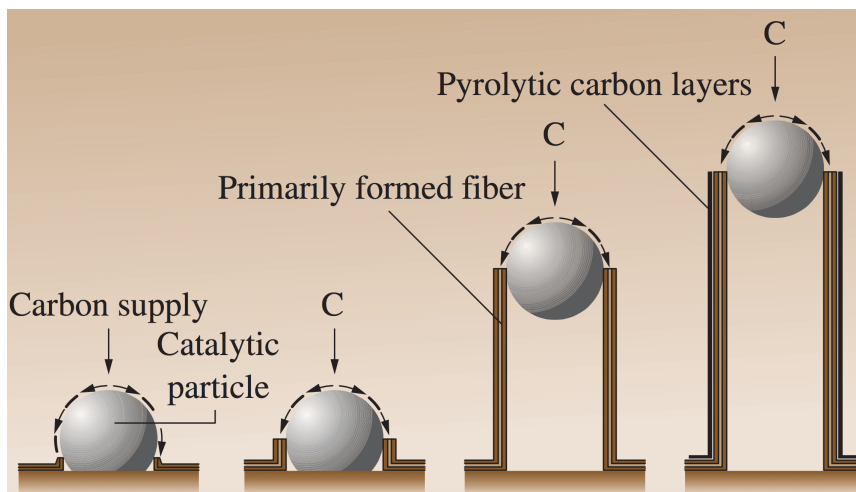
Figure 2.8: Suggested growth model of the tip-model [18].

not been fully understood. Hence this section and the next section will give an overview of the recent research related to N-CNFs used for ORR in PEMFCs [17].

The role of the support

In order to obtain a significant growth of N-CNFs on Fe particles, the particles are dispersed over a support.

A support for a electrocatalyst needs to satisfy some general needs: it should have a high surface area, sufficient electrical conductivity, maintain a high dispersion, high percentage of mesorpores and high stability in acid [15]. A high surface area is beneficial as the activity of a catalyst usually increases as the reaction surface are of the catalyst increases. In order for the electrons to flow through the support, the supports needs a certain electrical conductivity to act as a path. Moreover, the mesopores will provide accessible surface area to both the catalyst and the monomeric units of the membrane. This in turn, will benefit the diffusion of chemical species and the dissipation of reaction heat and thereby increase the poison resistance [15, 31].

A support may also interact with the active phase through either a electronic or geometric effect. The support may have the ability to influence the activity and reaction characteristics through chemical bonds between the support and the active phase. Furthermore, the support can also modify the shape of the active phase, influencing the number of active sites and thus the activity [15]. A catalyst support can modify the orientation of supported metal particles, and thus affect-

ing both the overall activity of the catalyst and its selectivity. This is especially applicable here, as the adsorption and dissociation of carbon-containing gas and thus the resulting N-CNF structures are highly sensitive to the metal crystal facets [30].

As mentioned before, the research conducted on N-CNFs is extensive, but few articles focus on the in-depth knowledge of different controlling parameters. Many different supports have been used to manufacture N-CNFs, but it seems that no research groups have been focusing on the effect of using different supports, e.g. expanded graphite and vulcan carbon. However, there is limited research done on CNFs which will be presented here. As N-CNFs and CNFs are very similar, it is believed that much of the theory also will be applicable for N-CNFs.

For CNFs it has been proven that both the support and the metal particles or nanoparticles (NP) have important feature concerning the growth of CNFs. The influence of the metal particles/NP will be discussed in the next section, so only the affect of the support will be discussed here. Using only metal particles as the initial catalyst for CNF growth has been reported to be less effective than metal particles/NPs on support. Unsupported metal particles will agglomerate during the elevated temperature, resulting in fewer growing sites. Supported metal particles on the other hand, will both have a more uniform size distribution and more homogeneous metal particles compared to the unsupported. This results in more exposed faced for the metal particles, and thus a higher CNF yield. Since this also affects the reactivity, the structural characteristics of CNFs (e.g. the alignment and crystallinity) may also be changed [30, 32]. The phenomena can be illustrated by the fact that platelet-type or fishbone-type CNFs are formed depending on the support. By using Fe deposited on supports with flat interfaces (e.g. graphite, silica) platelet-types are formed, while supports without flat interface (e.g. γ-Al$_2$O$_3$) form fishbone-type CNFs. However, the structure also is highly dependent on the carbon source used [32, 33].

In this thesis both vulcan carbon and expanded graphite have been used as supports. Vulcan carbon posses a high surface area and is low in cost and high in availability, whereas expanded graphite has a lower surface area than vulcan carbon, but excellent conductivity and a basal plane structure. These characteristics have made both supports suitable for metal-free catalyst used for fuel cells [14, 34, 35].

Effect of iron on the growth mechanism of CNFs

The effect or iron on the growth mechanism of N-CNFs has not been researched as extensive as for CNTs. However, there is still a debate whether Fe has any effect on the growth of CNTs or not. There are many claims that the size of the NP affects the diameter of the CNT, and they have been strengthen with the detection of CNTs and belonging NPs with equal diameter produced by CVD [36, 37].

However, NPs tend to agglomerate at higher temperatures and might thereby loose their catalytic efficiency, producing CNTs with different diameter than the original NPs [38]. This is supported by research indicating that the melting point decreases with decreasing diameter of the FeNP and thus increasing the tendency towards agglomeration. This means that smaller NPs would agglomerate first, resulting in thicker CNTs than the original NP diameter [39].

On the other hand, studies have also observed a lack of correlation between FeNPs and CNT diameter, indicating that the initial FeNPs are not responsible for the final CNT growth.. Among others, Moodley et al. [38] have proposed that metal particles can reshape during the growth of CNFs, affecting the graphene nucleation and fiber growth. The reshaping of the FeNP is thought to occur during the dissociative adsorption of the carbon source and the following carbon diffusion (as described in Section 2.5), initiated by the adsorption of surface carbon atoms [30].

Effect of the carbon source and reaction temperature

There is no doubt that the carbon source influences many factors, among other the shape of the metal particle and the shape and growth mechanism of the formed CNF/CNT [30, 40]. Both the metal particle and the growth mechanism has been reported to change by using different carbon sources.

The ratio of catalyst to carbon source has also been proven to be proportional to the fiber diameter and aspect ratio [40]. As the Fe concentration increases, the diameter decreases. In addition the stability and structural perfection decrease, raising the reactivity of the CNT's. However, there is an optimal ratio between the growth catalyst and the precursor. With either a too low or high concentration of the precursor the metal particles of the growth catalyst will deactivate.
Regarding the reaction temperature, there is an understanding that an increase in the reaction temperature will produce CNFs with smaller diameter and higher graphititc order, but this is also influenced by the carbon source concentration. The latter has been debated as reports have shown all kind of relations [30, 40].

2.6 Effects on activity

Both nitrogen and Fe have been attribute to influence the activity towards the ORR the most. Many aspects are still not fully understood, but below are some of the recent research highlighted to give an insight in the different theories.

Effect of nitrogen-doping on the activity

Nitrogen has an atomic size equal to the carbon atom and five valence electrons for bonding [13]. It is widely accepted that nitrogen-doping alters the properties of carbon structures by altering their electronic properties, and thus has an positively

influence on the activity [17]. Experiments have shown better electrocatalytic activity, long-term operation stability, and tolerance to crossover and poison effect with N-CNFs compared with the commercially available platinum-based electrodes for the ORR [14]. Many of these improvements are attributed to the nitrogen valence electrons. These have the ability to improve the electron-donation and electron density, and thus the ORR activity. They also create a net positive charge on the adjunct carbon atoms which is suggested to change the oxygen molecule adsorption model. In nitrogen free species, the O_2 molecule adsorbs end-on (Pauling model), whereas a side-on adsorption (Yeager model) is observed in nitrogen containing species. The side-on adsorption is also believed to weaken the $O-O$ bonding and thereby facilitating the ORR-process [11, 13].

The incorporation of nitrogen also effects the carbon structure. The graphene sheets are getting distorted by containing more dislocations and disruptions in the graphene stacking (turbostratic disorder) is an resulting effect [17].

There are four main forms of nitrogen that are present in a N-CNF structure: pyridinic-N, pyrrolic-N, quaternary-N, and pyridine-N-oxide. All groups are shown in Figure 2.9.

| Pyridinic-N | Pyrrolic-N | Quaternary-N | Pyridine-N-oxide |
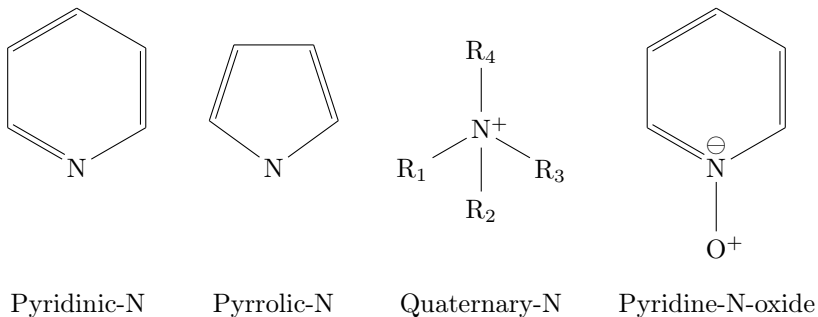
Figure 2.9: The four most common nitrogen groups in nitrogen-doped carbon nanofibers.

Although research argue which exact nitrogen groups act as catalytic centers, there is a strong believe that both pyridinic-N and quaternarty-N are the main contributors to the ORR activity. For quaternary-N, it it has been proven both experimentally and theoretically that it contributes as a catalytic center. Through computer analysis Ikeda et al. [41] have proven that the adjacent carbon atoms next to the quaternary-N are active for ORR, and that quaternary-N decreases the energy barrier more efficiently than pyridine-N. Other researches build their argument on the fact that pyridinic-N possesses one lone pair of electrons along the plane of the carbon matrix, and hence is the catalytic active center [42]. Never-

theless, it is also believed that pyridinic-N is unsuitable as the catalytic center, as sluggish ORR activity have been reported for some catalysts containing pyridinic-N [43]. In terms of electrolytes, quaternary-N is more stable in acidic media than pyridinic-N mainly due to the lower tendency to form protonation reactions. Interestingly, the work of Liu et al. [13] on nitrogen-doped carbon xerogels with metal dopants showed no direct correlation between gross nitrogen contents and catalytic activity. This indicates that the amount of nitrogen alone might not be the key responsible for the catalytic activity and that some by now unknown interactions might be key to the catalytic activity.

Effect of iron on the activity

In the addition to the debate discussed regarding the effect of nitrogen, there is also a debate as of the role the transition metal plays and especially in the relationship with nitrogen. It is accepted that Fe is the best promoter for the ORR reaction in terms of activity, and several studies have confirmed this [13, 44]. The fact that Fe has been observed to form metal/nitrogen complexes by coordinating with nitrogen, may be be a key feature as other metals only tend to form metal oxides. However, it is debated whether this contributes significant to the catalytical activity.

$MeN_xC_y^+$ is a structure that is believed to contribute to the ORR activity, and it's existence has been proven through extended x-ray absorption fine structure (EXAFS) and ToF-SIMS by showing structures like MeN_4/C and MeN_2/C [13, 45]. On the other hand, researches also believe that the transition metal only facilitates the incorporation of nitrogen atoms into the carbon-matrix and thereby form the active site. This is done by providing the an geometry location with a high degree of edge exposure for the nitrogen into the carbon species seen in Figure 2.9. However, even this is debated and can be illustrated by the differing research of Biddinger and Ozkan, and Mal. Biddinger and Ozkan [46] showed that edge plane exposures did not enhance the ORR activity. Mal [47] on the other hand, attributes the improved electro catalytic activity for the ORR in the carbon nanofibers to the presence of edge plane effects and nitrogen functional groups. Nevertheless, iron is still a key compound in the produce growth catalyst for N-CNF synthesis.

CHAPTER 3

CHARACTERIZATION

3.1 Scanning transmission electron microscope

The scanning transmission electron microscope (S(T)EM) is a combination of a scanning electron microscope (SEM) and transmission electron microscope (TEM). This means that it both possesses the property of a SEM in the sense of detecting the scattered electrons and providing information about the surface, and of a TEM in the sense of being able to detect transmitted electrons and hence providing information regarding the internal composition. By combining those two features the S(T)EM can be used to collect images down to 0.4 nm and provides the possibility to collect information regarding the elemental and internal composition, electronic structure and size of the sample [48].

As illustrated in Figure 3.1 a thin sample is bombarded with electrons from a focused beam and detectors around collect different signals simultaneously. Before the beam hits the sample, it is focused and concentrated through an objective lens. The scan coils are used to scan the electron beam across the sample and it is this feature that combines the two technologies, SEM and TEM [48].

Detectors

There are four different detectors installed in a S(T)EM and each give their own interpretation of the image. The detectors are:

- Bright field (BF)
- Dark field (DF)
- Secondary electron (SE)
- Back scatter electron (BSE)
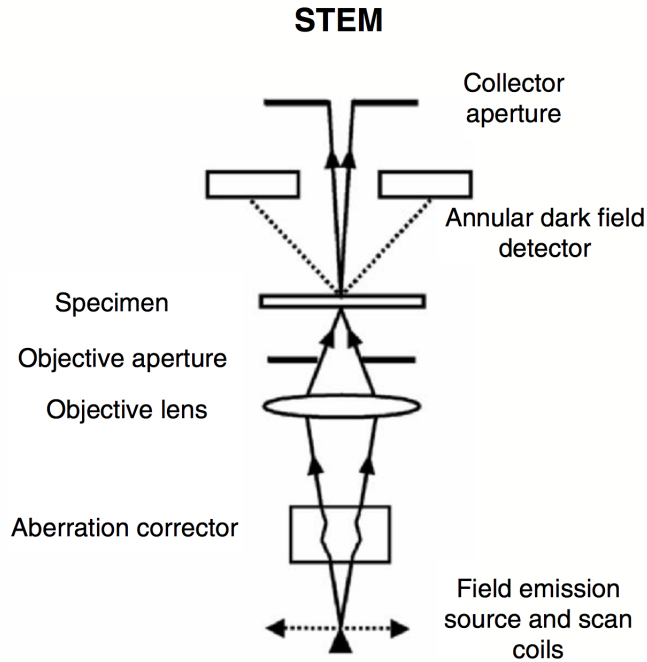
STEM

Figure 3.1: Schematic presentation of the main components of a S(T)EM [48]. The sample is bombared with electrons which have been focused and concentrated through an objective lens. Several detectors around collect the signal from sample.

The bright field detector includes the transmitted beam and thus shows holes as bright spots. This means that heavy compounds appear as dark spots and light compounds as bright spots. On the other hand, the dark field detector excludes the transmitted beam and includes the possibility to see the internal structure of a specimen [48]. The secondary electron (SE) detector is used to determine the morphological features of the surface of the sample, whereas the back scatter electron detector (BSE) determines the elemental contrast. In contrast to the BSE detector the SE detector only detects electrons which have penetrated the surface with an certain depth, whereas the BSE detects electrons from a much greater depth [49].

Energy dispersive x-ray spectroscopy

Energy dispersive x-ray spectroscopy (EDX) is a built in detector which measures the elemental identity of the elements present in the sample. By generating a voltage pulse that is proportional to the x-ray energy generated by the specimen through the beam, the resulting x-ray counts are converted to a spectra or quantitative compositional profiles, where each element has its own characteristic peak pattern. As light elements have a low x-ray yield due to a high adsorption in the specimen, a common problem of too low x-ray counts per second (cps) and resulting noise [50, 51, 52].

Acceleration Voltage

There are several options for acceleration voltages in a S(T)EM, ranging from low (1.5 kV) to high (30 kV). The higher the acceleration voltage, the poorer is the resolution but the higher is the beam-specimen interaction. The significance of the effect is also governed by the atomic number of the specimens. With a low atomic number specimen the scattering will be more prominent at high acceleration voltage as it is with a high atomic number specimen.

As the surface area of the samples examined in this project are not of primary interest, the best results are obtained with both a high acceleration voltage and emission current, together with the bright field detector.

3.2 Thermogravimetric analysis

Thermogravimetric analysis (TGA) is used to follow microscopic weight changes by measuring the sample as a controlled gas flow and temperature ramp is initiated [53]. There are many variations and both the temperature and the gas and its flow can be varied. It is possible to employ TGA in order to establish procedures for regenerating the catalyst, but it can also be used to establish e.g. oxidation temperatures. The instrument can be coupled to a gas chromatography (GC) column with a mass spectrum (MS) in order to map the composition of the probe and thereby determine the oxidized species.

3.3 X-ray diffraction

The crystallinity can be measured by powder X-ray diffraction (XRD) with assumptions that the catalyst is crystalline and hence able to diffract x-rays. As the angles of diffraction differ from the various planes within the crystal, every compound has its own unique diffraction pattern. The diffraction pattern is displayed as peaks, and the larger the crystal of a component is, the sharper the peaks of the crystal planes will be. Thus is it is possible to determine both which elements are present and in what amount, making this technique both a quantitative and
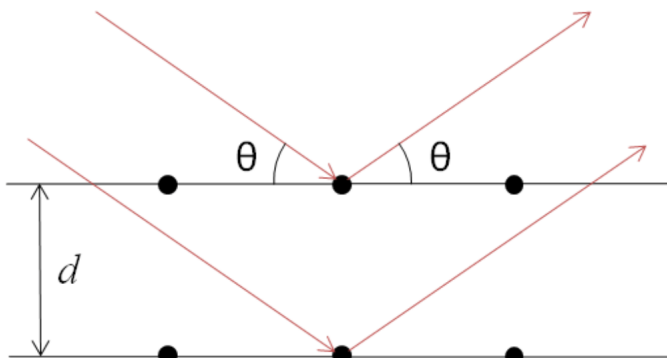
Figure 3.2: Schematic presentation of elastic scattering of incoming rays on de-
picting atoms (black dots) in an ordered lattice, where θ denotes the
diffraction angle and d is the distance between two adjacent lattice
planes [54]

qualitative technique. The described phenomena can be seen by employing the
Scherrer equation (3.1).

$$L = \frac{k\lambda}{B \cos \theta} \tag{3.1}$$

L is the size of the crystallites, k is a constant that is usually close to 0.9, λ is the
X-ray wavelength, B is the width at half-peak height of an XRD line, and θ is the
diffraction angle [53].

Figure 3.2 illustrates elastic scattering of incoming rays in an ordered lattice. In
order for the reflected beam to be registered by the detector, the incoming and re-
flected beam need to be in constructive interference, which is governed by Bragg's
law, Equation (3.2). Bragg's law denotes that the incident angle and reflected angle
need to be equal in order to result in constructive interference [53, 54].

$$n\lambda = 2d_{hkl} \sin \theta_{hkl} \tag{3.2}$$

Here, n is an integer, λ is x-ray wavelength, d_{hkl} is the distance between two
adjacent lattice planes and θ_{hkl} is the diffraction angle.

3.4 X-ray photoelectron spectroscopy

X-ray photoelectron spectroscopy (XPS) is a method to quantitatively analyze both the chemical composition and the different chemical states of an element in the surface region of the sample. Surface atoms are identified through their specific electronic binding energies by using an incoming photon that is adsorbed at the surface and emits a photoelectron, as illustrated in Figure 3.3. The initial binding energy of the photoelectron relative to the Fermi level of the sample E_b can be described by Equation (3.3) [55].

$$E_b = hv - E_{kin} - e\phi_{spec} \tag{3.3}$$

Here hv is the energy of the incoming photon, E_{kin} is the kinetic energy of the photoelectron and $e\phi_{spec}$ is the work function of the spectrometer. From Figure 3.3 it can bee seen that the ionized electron level and the binding energy E_b of a photoelectron are related. This implies that the information containing the emitting element and the ionized orbital can be extracted from E_b, and thereby also possible to determine the different nitrogen-containing functional groups on carbon nanofibers. In finer energy resolution it also possible to extract information regarding the oxidation state of the atom and different nitrogen groups [56].

XPS spectra are quantified in terms of peak intensities and peak positions, where the former measures the amount of material at the surface and the latter indicates the elemental and chemical position. An illustratioin of a XPS spectra is given in Figure 3.4. In order to quantify the spectra, it is assumed that the number of
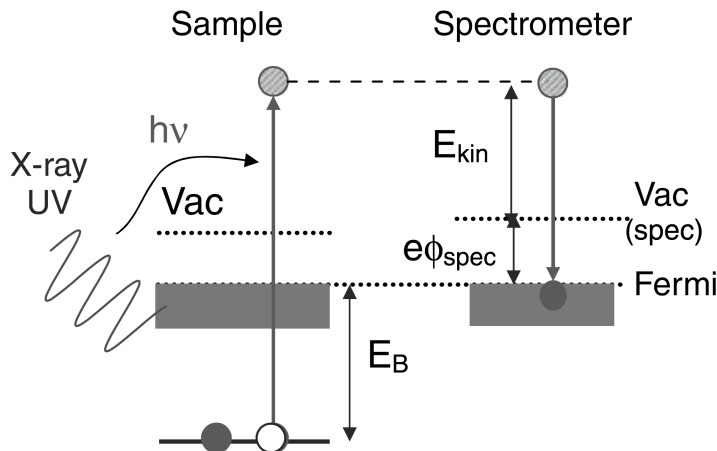

Figure 3.3: Schematic presentation of the energy in level in photoemission and analysis of photoelectrons in a solid [56].
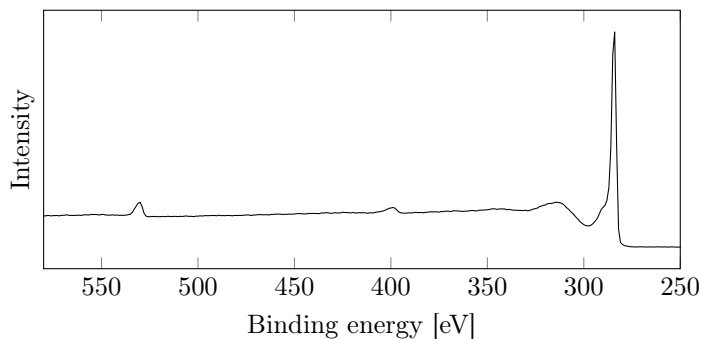
Figure 3.4: Illustration of a recorded XPS spectra.

electrons recorded are proportional to the number of atoms in a given state. It is normal to compare the peaks in terms of percentage atomic concentration, $at\%$ instead of comparing the peak areas for the following two reasons:

- The instrumentation is not able to record all electrons and this is reflected by a XPS spectrum as it records the number of detected electrons leaving the sample surface.

- The operating mode determines to some extent the kinetic energy of the electrons, which again determines the efficiency with which emitted electrons are recorded.

Percentage atomic concentration denotes the intensities of the spectrum as a percentage and is found from the peak areas. Hence, it can be taken as the ratio of the intensity to the total intensity of electrons in the measurement. If the experimental conditions changes, the changes in peak intensities will be in an absolute sense and hence remain constant in relative terms [57].

3.5 BET

BET is short for Brunauer, Emmett and Teller, and is a method that determines how many molecules are needed to form a complete monolayer. 8The occupied volume can hence be transferred to the total area of the catalyst by the means of the BET isotherm (3.4) [58].

$$\frac{P}{V_a\left(P_0 - P\right)} = \frac{1}{\chi V_0} + \frac{(\chi - 1)}{\chi V_0}\frac{P}{P_0} \equiv \eta + \alpha\frac{P}{P_0} \tag{3.4}$$

Here, $\chi = {k_2}/{k_1}$ is the ratio of desportion rate constants for the second and first layer, P_0 is the equilibrium pressure of the condensed gas at the experimental temperature, V_0 is the volume adsorbed at monolayer coverage and V is the volume

adsorbed at P. The graph yields a straight line when plotting $P/[V_a(P_0 - P)]$ against P/P_0 with the slope $\alpha = {(\chi - 1)}/{\chi V_0}$ crossing the y-axis at $\eta = 1/{\chi V_0}$. By using the assumption of ideal gas and the ideal gas law (3.5), the volume adsorbed at monolayer can be converted into the number of molecues adsorbed, N_0.

$$N_0 = {PV_0}/{RT} \tag{3.5}$$

In addition, the method can also determine the types of pores and their size distribution by the means of the Kelvin equation and capillary pore condensation. [58].

As with all methods, BET has its limitations but can be said to be valid under the following assumptions [58]:

- Equal rate of adsorption and desoprtion in any layer.

- Molecules adsorbed are beeing used as adsorption sites for the next layer of molecules.

- Ignoring adsorbate-adsorbate interations.

- Adsorption-desorption conditions are assumed to be the same for all layers but the first.

- The adsorption energy equals the condensation enery for molecules in the 2nd and higher layers.

- The thickness of the multilayer grows to infinite at saturation pressure ($P = P_0$).

CHAPTER 4

EXPERIMENTAL

The main idea of this thesis was to produce a homogeneous growth catalyst for the synthesis of nitrogen-doped carbon nanofibers (N-CNFs). This was done by producing iron nanoparticles (FeNPs) with a narrow size distribution, depositing them on support and growing N-CNFs on the obtained growth catalyst. The catalyst was then characterized by S(T)EM, TPO, XPS and XRD, and at last tested in a conventional three-electrode system.

4.1 Synthesis of iron nanoparticles

The iron nanoparticles (FeNPs) were original synthesized by a method described in [59].

A solution of $50 \, \mathrm{ml}$ octadecene and $0.75 \, \mathrm{ml}$ olyelamine was heated to $120 \, \mathrm{°C}$ with a heating ramp of $10 \, \mathrm{°C \, min^{-1}}$ under an Ar-atmosphere and magnetic stirring. After degassing the solution for $30 \, \mathrm{min}$, the temperature of the solution was raised by $10 \, \mathrm{°C \, min^{-1}}$ up to $200 \, \mathrm{°C}$. $12.98 \, \mathrm{mmol}$ of iron pentacarbonyl ($\mathrm{Fe(CO)_5}$, Sigma Aldrich) was injected to the hot solution and the reaction mixture was for $2 \, \mathrm{h}$. A black solution indicated the formation of nuclei. After cooling the reaction mixture, the black product was attached to the magnetic stirrer and collected via toluene. The final product, 200Fe, was stored in toluene.

During the thesis some alternatives were tried in other to obtain larger FeNP particles. In the first alteration, all reagents were mixed at room temperature, and the temperature was raised by $3 \, \mathrm{°C \, min^{-1}}$ up to $200 \, \mathrm{°C}$. The reaction mixture was refluxed for $40 \, \mathrm{min}$ and the final cooled sample, FeRT, was collected via and stored in hexane. In the second alteration, the mixture of octadecene and olyelamine was first heated up to $120 \, \mathrm{°C}$ with an heating ramp of $10 \, \mathrm{°C \, min^{-1}}$ and
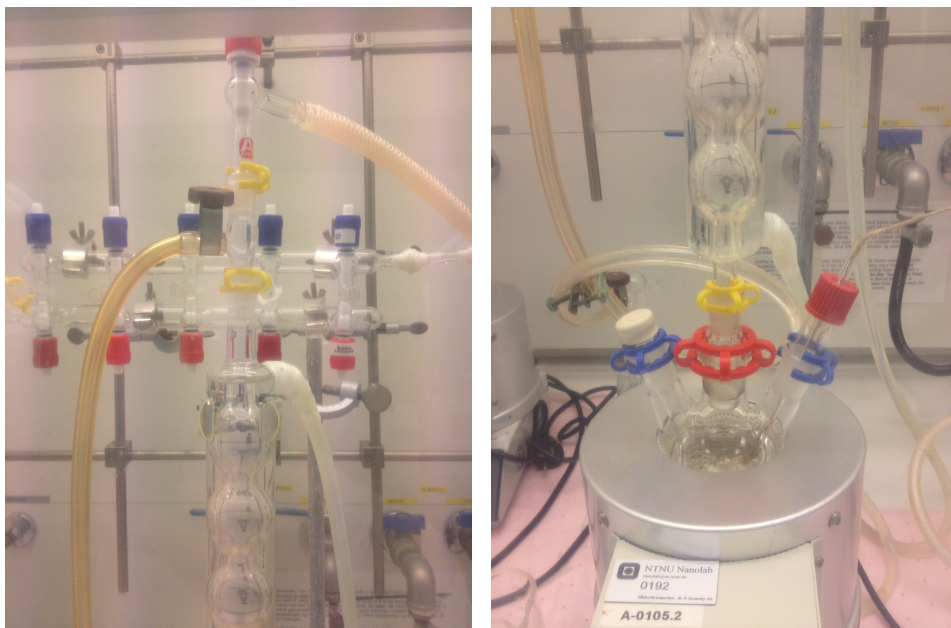
(a) The upper part of the
FeNP-synthesis set-up.

(b) The lower part of the
FeNP-synthesis set-up.

Figure 4.1: Set-up for the synthesis of iron nanoparticles (FeNPs). The thermo-
couple is not shown.

refluxed for 30 min. $Fe(CO)_5$ was then injected and the temperature was raised to
$260\,°C$ with an heating ramp of $10\,°C\,min^{-1}$. The reaction mixture was refluxed for
40 min and the final cooled sample, Fe260C, was collected via and stored in hexane.

The set-up of the FeNP synthesis is shown in Figure 4.1 and consist of the fol-
lowing main equipment:

- Round-bottom flask
- Thermocouple
- Reflux column
- Magnetic stirrer

4.2 Impregnation of iron particles on support

Both FeNPs from the sample 200Fe and iron nitrate were impregnated on expanded graphite and vulcan carbon by incipient wetness and wet impregnation respectively with an aim of a 20 wt% loading of Fe. The produced samples were named 200ExG and 200Vu for the FeNP impregnated samples, and ExGM and VuM for the iron nitrate impregnated samples. Table 4.1 summarizes the impregnated samples and their impregnation method.

Table 4.1: Impregnated samples with their iron source and impregnation method.

Sample name	Iron source	Impregnation method
200ExG	200Fe	Incipient wetness
ExGM	Iron nitrate	Incipient wetness
200Vu	200Fe	Wet impregnation
VuM	Iron nitrate	Wet impregnation

Impregnation with iron nanoparticles

Expanded graphite was prepared by heating oxidized graphite in a microwave-oven at 700 W for 60 s. 15 ml of FeNP with a concentration of $0.024\,\mathrm{g\,cm^{-3}}$ dissolved in toluene were then added to 15 g of exfoliated graphite. The growth catalyst was dried for several days in a closed hood before it was dried for 3 h in a oven at 90 °C. To remove solvents from the FeNP synthesis, the sample was washed several times by water, ethanol and aceton in a Büchner trakt. Finally, the product was dried for another 3 h in an oven at 90 °C.

For the vulcan sample the growth catalyst was prepared by wet impregnation with the same ratio as for the expanded graphite, but with corrected concentration: 19 ml FeNP with a concentration of $0.0185\,\mathrm{g\,cm^{-3}}$ and 0.375 g carbon vulcan. The growth catalyst was sonicated for 5 h and dried over night before. To remove solvents from the FeNP synthesis, the sample was washed several times by water, ethanol and aceton in a Büchner trakt. Finally, the product was dried for 3 h in an oven at 90 °C.

It was difficult to calculate the loading in advance due to loss of iron in the synthesis in form of other iron products. Thus, the noted weight was based on trial and error and measurements based on XRF and TGA.

Impregnation with iron nitrate

The expanded graphite was prepared by the same method as with the impregnation with FeNPs – oxidized graphite was heated in a microwave-oven at 700 W for 60 s. The growth catalyst was then prepared by incipient wetness impregnation: 2 g of exfoliated graphite was mixed with 3.214 g $Fe(NO_3)_3$x9H_2O dissolved in 35 ml ethanol, and dried at room temperature for at least a day before being used.

The same method with the same ratio was conducted with vulcan carbon, but resulting in a wet impregnation instead of incipient wetness. Once again, the growth catalyst was dried at room temperature for at least a day before being used.

4.3   Synthesizing nitrogen-doped carbon nanofibers

Nitrogen-doped carbon nanofibers (N-CNFs) were synthesized using a CVD-method (as described in Section 2.5) with the prepared samples listed in Table 4.1 and a FeNP sample without support (200Fe). The general method is described below, and the different reaction conditions and sample names are given in Table 4.2.

The samples were loaded in a tubular quartz reactor and reduced in an H_2/Ar flow (40 ml min^{-1} and 160 ml min^{-1}) by increasing the temperature of the furnace up to either 650 °C or 750 °C with an heating ramp of 3 or 15 °C min^{-1}. Subsequently, the N-CNFs were grown at the temperature using a synthesis gas mixture of CO/NH_3/H_2 (60 ml min^{-1}, 6.5 ml min^{-1} and 20 ml min^{-1}). After 24 h the reactor was cooled down to room temperature under an Ar flow. The set-up is illustrated in Figure 4.2.

Table 4.2: Different reaction conditions used in the N-CNF synthesis

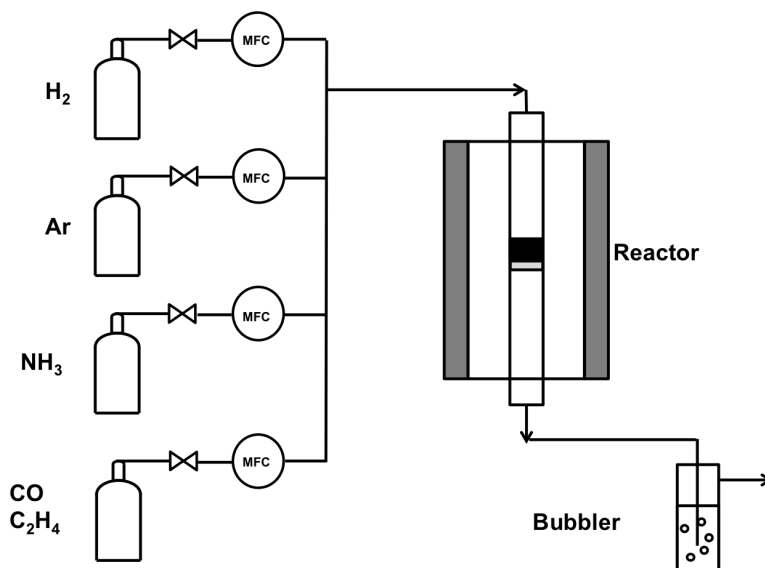| Sample name	Amount loaded [g]	Reaction temperature [°C]	Heating ramp [°C min^{-1}]
200Fe24h	0.21	650	15
200ExG24h	0.05	750	15
ExGM24h	0.5	750	3
200Vu24h	0.11	750	15
VuM24h	0.11	750	15

Figure 4.2: Illustration of the reaction set-up for the synthesis of nitrogen-doped carbon nanofibers.

Checking for agglomeration

In order to chekc if the FeNP agglomerate during the reduction of the N-CNF synthesis, the samples 200ExG, ExGM and 200Vu where first reduced using the same conditions as in their respective N-CNF synthesis (Section 4.3), and then passivated with a small flow of air ($10\,\%$ O_2 in N_2) for 15 min at room temperature.

4.4   Electrochemical measurements

The electrode used was a rotating ring disk electrode consisting of a glassy carbon disk and a Pt-ring. The electrode was prepared by first weighing out $3\,mg$ of the catalyst. $500\,\mu l$ of H_2O, $200\,\mu l$ of isopropyl alcohol, $200\,\mu l$ of ethanol and $100\,\mu l$ of 0.5wt% nafion were measured out and mixed with the catalyst, before they was sonicated for 30 min. $16\,\mu l$ of the dispersion was then placed on the glassy carbon electrode and dried for 30 min in N_2-saturated atmosphere. After the catalyst layer had dried, a protective layer of 50/50 H_2O/ethanol and 0.5wt% Nafion was added by placing $10\,\mu l$ of each on the electrode and allowing it to dry overnight. Last, $10\,\mu l$ of a 50/50 H_2O/ethanol solution was added onto the electrode before the experiment start to simplify the wetting process of the electrode with the electrolyte.

The electrochemical measurements were conducted with a conventional three-electrode system, with a reversible hydrogen electrode (RHE) as reference electrode, plat-
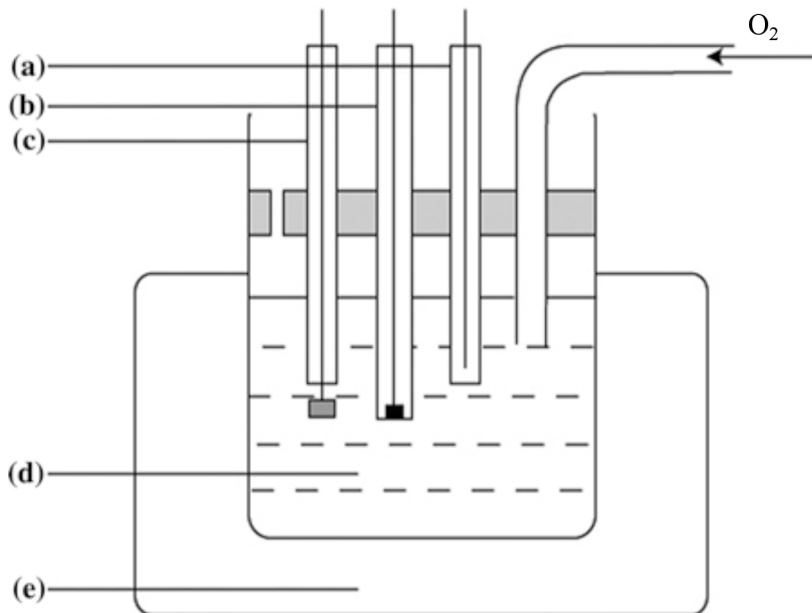
Figure 4.3: Illustration of a three-electrode system with (a) the reference electrode, (b) the working electrode, (c) the counter electrode, (d) the electrolyte, (e) a constant temperature bath. (e) was not used during the experiments conducted in this report [60].

inum foil as counter electrode and a $0.5\,M$ H_2SO_4 as the electrolyte. Figure 4.3 illustrates the set-up. By using linear sweep voltammetry (LSV), the experiments were performed at room temperature in an O_2-saturated atmosphere. The linear sweep voltammograms were recorded at a scan rate of $5.0\,\mathrm{mV\,s^{-1}}$ from $1.10\,V$ to $0.01\,V$ while the electrode was rotated at $1600\,\mathrm{rpm}$. The onset potential (EORR) for the oxygen reduction was measured by comparing the cathodic scan obtained in an Ar-saturated atmosphere with the same electrolyte. In order to determine the amount of H_2O_2 produced on the working electrode, a constant potential was applied to the Pt-ring during the LSV.

Removing iron from 200Fe24h

For the sample 200Fe24h, the iron was removed before the electrochemical measurement in order to avoid noise from Fe corrosion in acid during the measurements. $10\,\mathrm{ml}$ HCl was added to the sample, and the sample was heated in a silicon oil bad at $80\,°C$ for $2\,h$. The purified sample was then collect by centrifuging the acid

mixture.

4.5 Characterization

Several different characterization methods were conducted and the apparatus is described below. A description of the theory behind the different methods is given in Chapter 3.

Scanning transmission electron microscope

The analysis was performed using a Hitachi S-5500 S(T)EM. A few particles of the samples were mixed with ethanol and sonicated for about 1 min. A drop of the dispersion was then placed on a hole carbon grid sample holder. For most pictures, an acceleration voltage of 30 kV and an emission current of either 20 µA were used.

Temperature programmed oxidation

The temperature programmed oxidation was performed in a Netzsch STA 449C Jupiter which conducted the thermogravimetric analysis and differential scanning calorimetry. Attached to the instrument was a Netzsch Aërlos QMS 403C which performed the mass spectrometry of the outlet gas flow.

All samples were oxidated by heating the sample up to $900\,°C$ with a heating ramp of $10\,°C\,min^{-1}$ in a flow of $80\,ml\,min^{-1}$ of air.

X-ray diffraction

The x-ray diffraction (XRD) was performed on a D8 DaVinci with a Lynxeye-detector and a Cu-target ($1.54\,Å$). As the yields of both the synthesis of the FeNPs and the synthesis of N-CNFs were low, the samples were spread out on a small sample carrier. This technique is not optimal and some noise can be expected in the spectrum. The samples were analyzed in a 30 min program from 15° and 75° with varying slits.

X-ray photoelectron spectroscopy

The x-ray photoelectron spectroscopy (XPS) was performed on a Kratos Axis Ultra DLD spectrometer with monochromatic Al Kα radiation ($hv = 1486.58\,eV$). The survey spectra were collected using fixed analyzer pass energies of 160 eV.

CHAPTER 5

RESULTS

This Chapter provides both the synthesis and the characterization results obtained for the synthesized iron nanoparticles (FeNPs) and the nitrogen-doped carbon nanofibers (N-CNFs) grown on the FeNPs. All measurements of the diameter and the particle count in Sections 5.1, 5.3 and 5.7 are done by the program Image J if nothing else is noted.

5.1 Synthesis of iron nanoparticles

The sample name, the belonging synthesis temperature, and the average diameter of the synthesized FeNP are summarized in Table 5.1. As the FeNPs were collected in solution, no yield or concentration (as the volume varied) were calculated.

Table 5.1: The average diameter of the iron nanoparticles varied with reaction conditions.

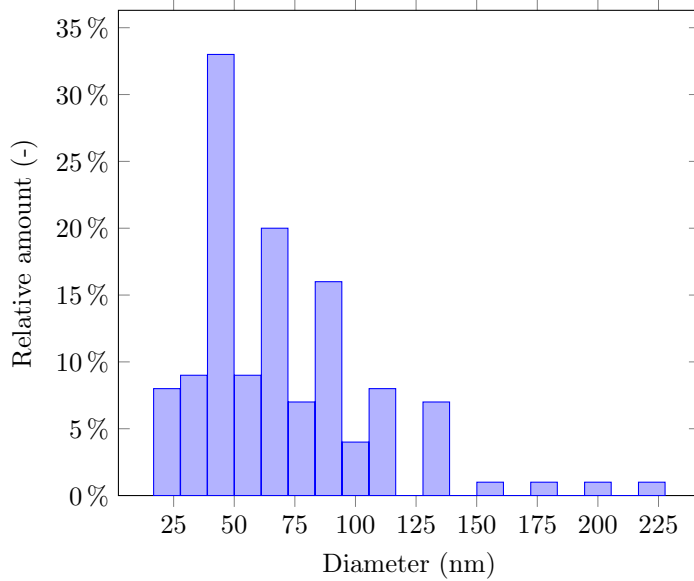| Sample name	Synthesis temperature (°C)	Heating ramp during synthesis ($°C\,min^{-1}$)	Average diameter (nm)
260Fe	120 to 260	10	5.4±0.5
200Fe	200		9.7±0.5
RTFe	25 to 200	3	70±10

Figure 5.1: RTFe: Particle size distribution of RTFe based on Figure 5.2a with an average diameter of 70±10 nm based on a count of 125 particles. The measurement was conducted by hand.

RTFe

Figure 5.1 show the particle size distribution of the FeNPs synthesis from room temperature based on Figure 5.2a. The average diameter is 70±10 nm with a count of 125 particles, and the measurements were conducted by hand. Figure 5.2b illustrates a close up of Figure 5.2a.
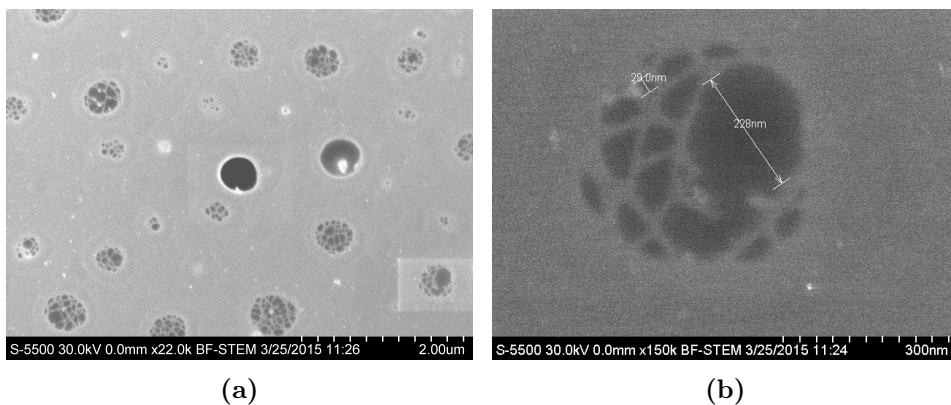
(a)

(b)

Figure 5.2: RTFe: FeNPs deposited on expanded graphite. Figure 5.2a is used for the size distribution in Figure 5.1.

260Fe

Figure 5.3 illustrates the FeNP synthesized between $120\,°C$ and $260\,°C$ and the belonging size distribution. The average diameter is $5.4\pm0.5\,nm$ based on a count of 1008 particles. A close-up of the FeNPs is illustrated in Figure E.1.
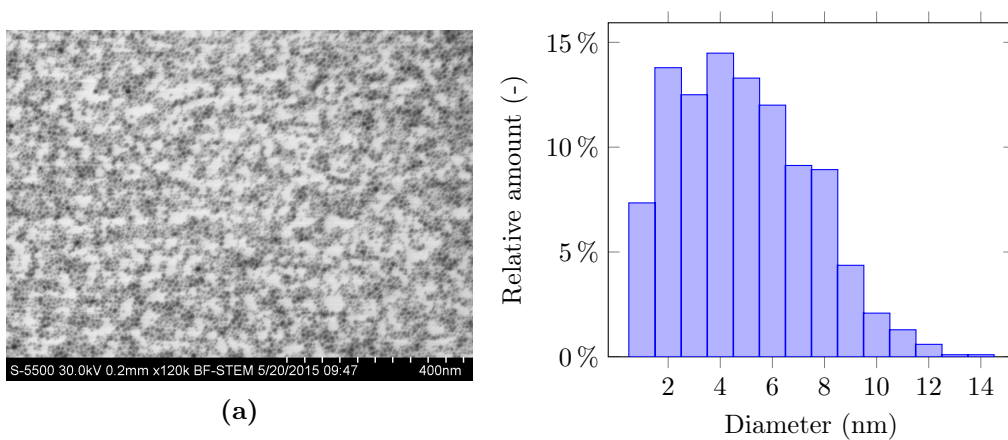

(a)

Figure 5.3: 260Fe: Particle size distribution based on the left S(T)EM image. The average diameter is $5.38\pm0.5\,nm$ based on a count of 1008 particles.

200Fe

Figure 5.4 illustrate a S(T)EM images of the synthesised FeNPs with the belonging size distribution. The average diameter is 9.7±0.5 nm based on a count of 383 particles.
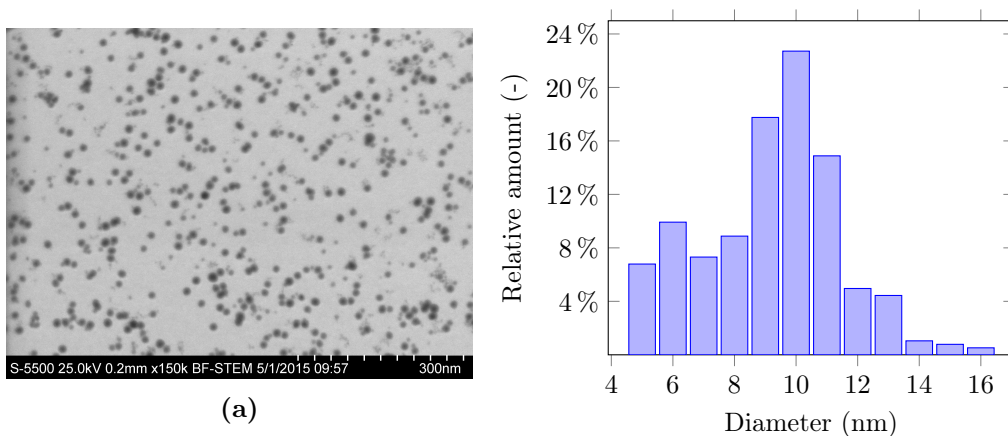

(a)

Figure 5.4: 200Fe: Particle size distribution based on the left S(T)EM image. The average diameter is 9.7±0.5 nm based on a count of 383 particles.

5.2 Calculation of the iron loading after impregnation

The samples 200ExG, ExGM, 200Vu and VuM were examined by TPO in order to calculate the Fe loading. All Fe loadings were calculated as described in Appendix A based on the information given in Table A.1. Figure 5.5 illustrates the TPO graph for all samples and detailed graphs for each sample can be found in Figures B.1 to B.4.

The initial weight loss of about 8 % for 200ExG is presumably due to loss of low molecular species such as adsorbed moisture and residual solvents, whereas the weight gain for 200Vu is presumably due to adsorption of moisture. The Fe loadings were calculated to be 16.4 % for 200ExG (with taken into account the initial weight loss), 18.4 % for ExGM, 17.3 % for 200Vu and 17.4 % for 200Vu. Table 5.3 summarizes the results together with the N-CNFs results.
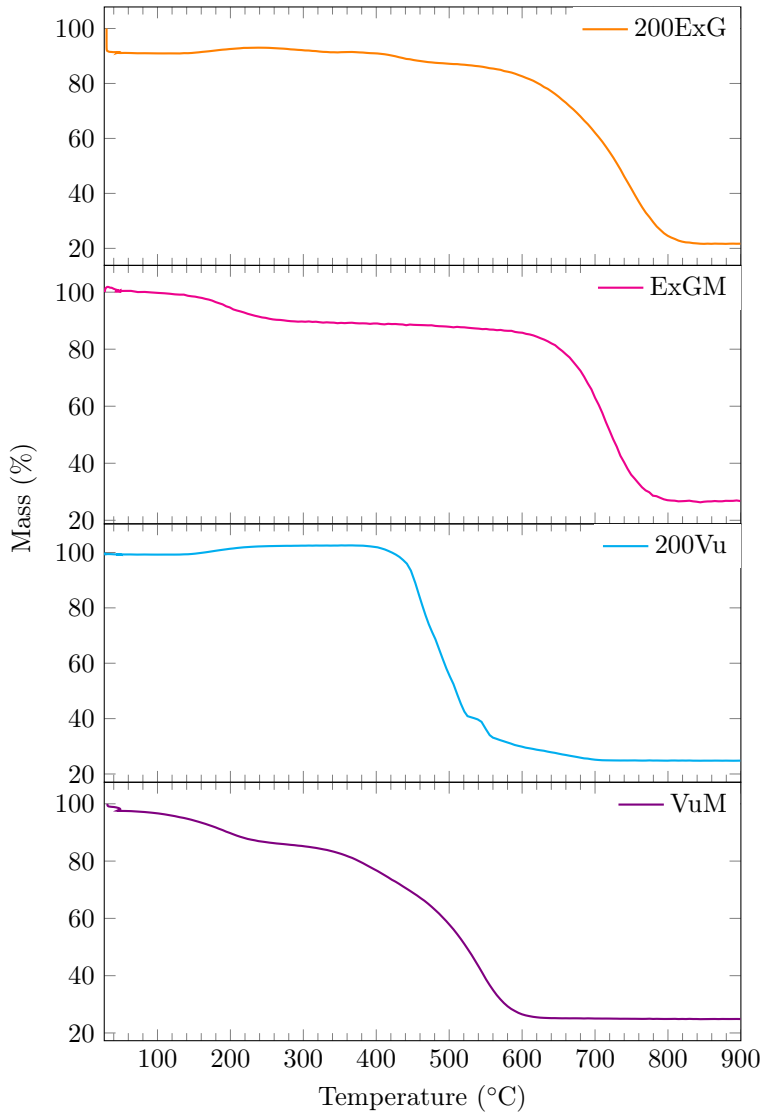
Figure 5.5: The support of the different impregnated samples is burnt of with increasing temperature, resulting in a decrease of the mass percentage for 200ExG ———, ExGM ———, 200Vu ——— and VuM ———.

5.3 Checking for agglomeration

Figure 5.6 presents the XRD plot for 200ExG and 200Vu reduced at 750 °C, and ExGM reduced at 650 °C (200ExGRed, 200VuRed and ExGMRed). All new particles sizes are summarized in Table 5.2.

A new average particle size was calculated for 200Vu to be 25 nm from the Fe top at about 45° in Figure 5.6 with the Scherrer equation (Equation (3.1)) in the analysis program Diffrac Eva. A close up of the Fe top with the lines used for the calculation is illustrated in Figure 5.7. Carbon vulcan is amorphous, and hence no C is detected as it is with expanded graphite.

As the Fe peak is too disturbed by the other graphite peaks for both 200ExGRed and ExGM, the new average particle size was calculated based on S(T)EM images. Figure 5.8 illustrates agglomerate FeNPs on a expanded graphite flake with the belonging size distribution. The average diameter is 69.5±0.5 nm based on a count of 100 particles. Figure 5.9 illustrates agglomarated FeNPs without support for 200ExGRed, and the new average diameter is 39.5±0.5 nm based on a count of 94 particles. The belonging size distribution for Figure 5.9 is given in Appendix D, Figures D.2 and D.3. For ExGMRed, a new average particle size was determined from Figure 5.10 to be 14.5±0.5 nm based on a count of 133 particles.

Both the reduction and the XRD scans were conducted at 650 °C for the two samples 200ExG and 200Vu. As the results were not significant different, the graphs are displayed in Appendix C, Figure C.1.

Table 5.2: Sample name, reduction temperature and average diameter of the agglomerated FeNPs.

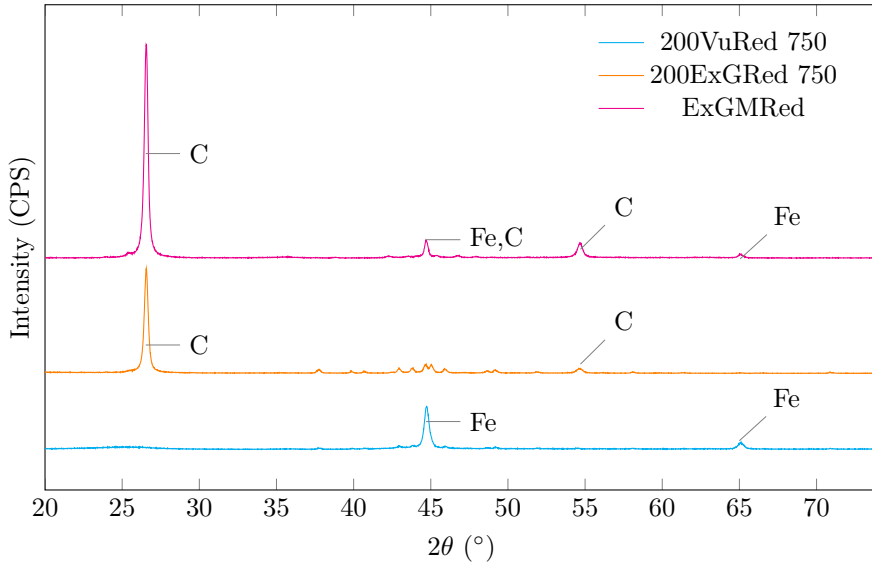| Sample name	Reduction temperature (°C)	Average diameter (nm)
ExGMRed	650	14.5±0.5
200VuRed	750	25
200ExGRed	750	69.5±0.5 and 39.5±0.5

Figure 5.6: XRD scan of the reduced samples of ExGM at 650 °C, 200ExG at 750 °C ―― and 200Vu at 750 °C ――. C represents carbon in the form of graphite, whereas Fe represents metallic iron. The peaks in the range 40° to 50° for 200ExGRed are mostly graphite, but also contain a combined Fe and C peak at about 44.5°.
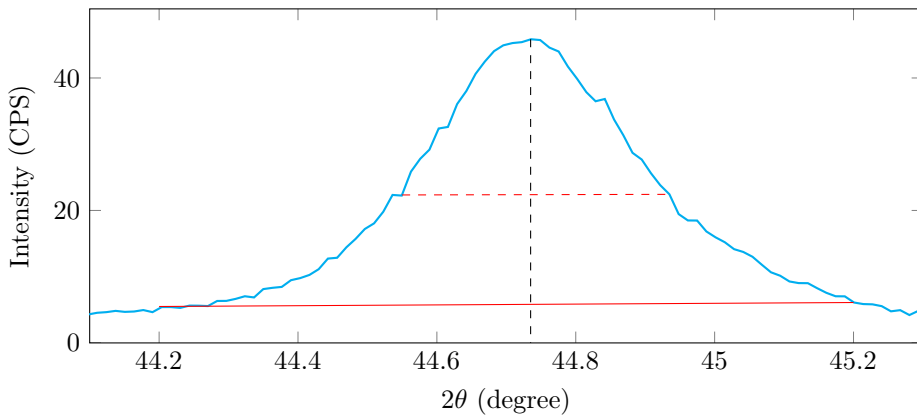

Figure 5.7: XRD 200VuRed: Close up of the Fe top used for calculating the average particle size. ―― marks the bottom line, - - - marks the full width at half maximum (FWHD) and - - - the maximum.
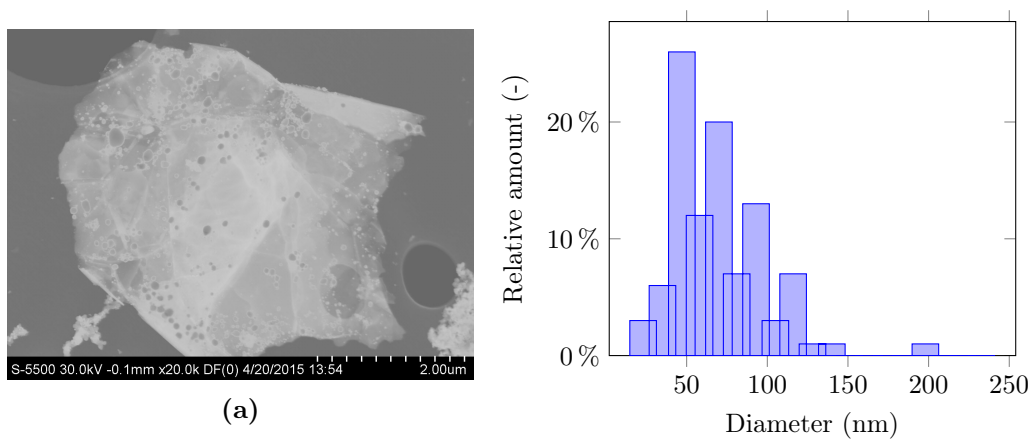
(a)

Figure 5.8: 200ExGRed: Particle size distribution of Figure 5.8a. The average diameter is 69.5±0.5 nm based on a count of 100 particles.
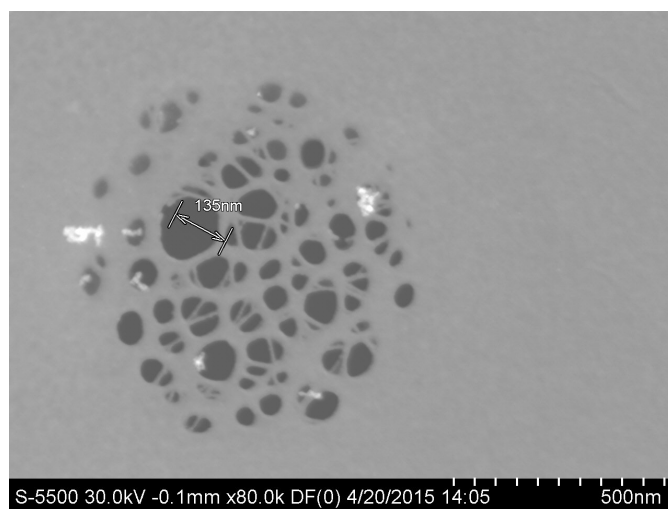

Figure 5.9: 200ExGRed: The average diameter is 39.5±0.5 nm based on a count of 94 particles.
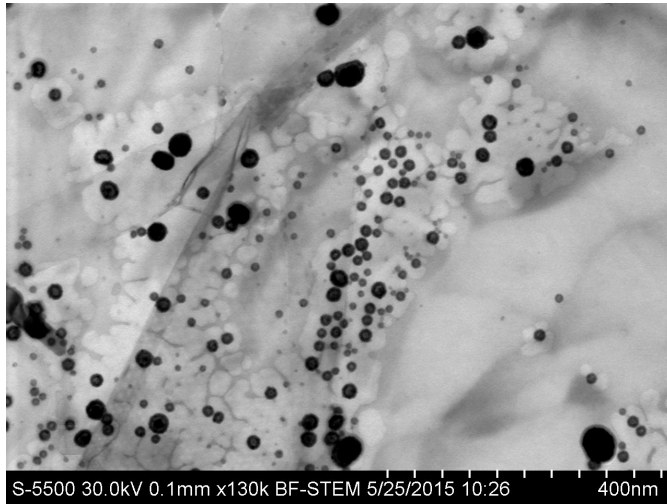
Figure 5.10: S(T)EM ExGMRed: Images used for determining the particle size distribution given in Figure 5.11.
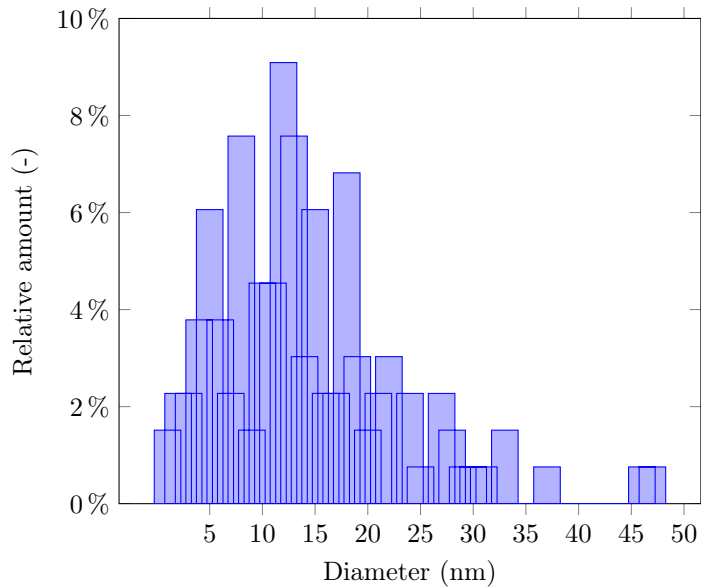

Figure 5.11: ExGMRed: Particle size distribution based on Figure 5.10. The average diameter is 14.5±0.5 nm based on a count of 133 particles. The belonging size distribution is found in Appendix D, Figures D.2 and D.3.

5.4   Synthesis of nitrogen-doped carbon nanofibers

The weight after the N-CNFs synthesis, the yield and the iron loading are presented for all samples in Table 5.3 and increases with an increaing iron loading. The yield was calculated by Equation (5.1).

$$Yield = \frac{m_{N-CNF}}{m_{Fe}} \tag{5.1}$$

Table 5.3: Weigth after synthesis, mass of the grown N-CNFs, yield and Fe loading for the synthesized samples.

Sample name	Weight after (g)	Mass of N-CNFs grown (g)	Yield (g/g$_{cat}$)	Fe Loading (wt%)
200Fe24h	0.25	0.04	0.21	
200ExG24h	0.08	0.03	4.07	16.4
200Vu24h	0.22	0.11	5.60	17.3
VuM24h	0.25	0.14	7.25	17.4
ExGM24h	1.26	0.76	8.26	18.4

5.5   X-ray photoelectron spectroscopy

The relative percentage atomic concentration (at%) values for N, O and Fe obtained from the XPS scan are given in Table 5.4. Figure 5.12 illustrates a close-up of the N 1 s peak, which consist of two main peaks. These are appointed to represent quaternary-N at 401 eV and pyridinic-N at 398.5 eV.

Table 5.4: XPS: The relative percentage atomic concentration (at%) of nitrogen (N), oxygen (O) and iron (Fe).

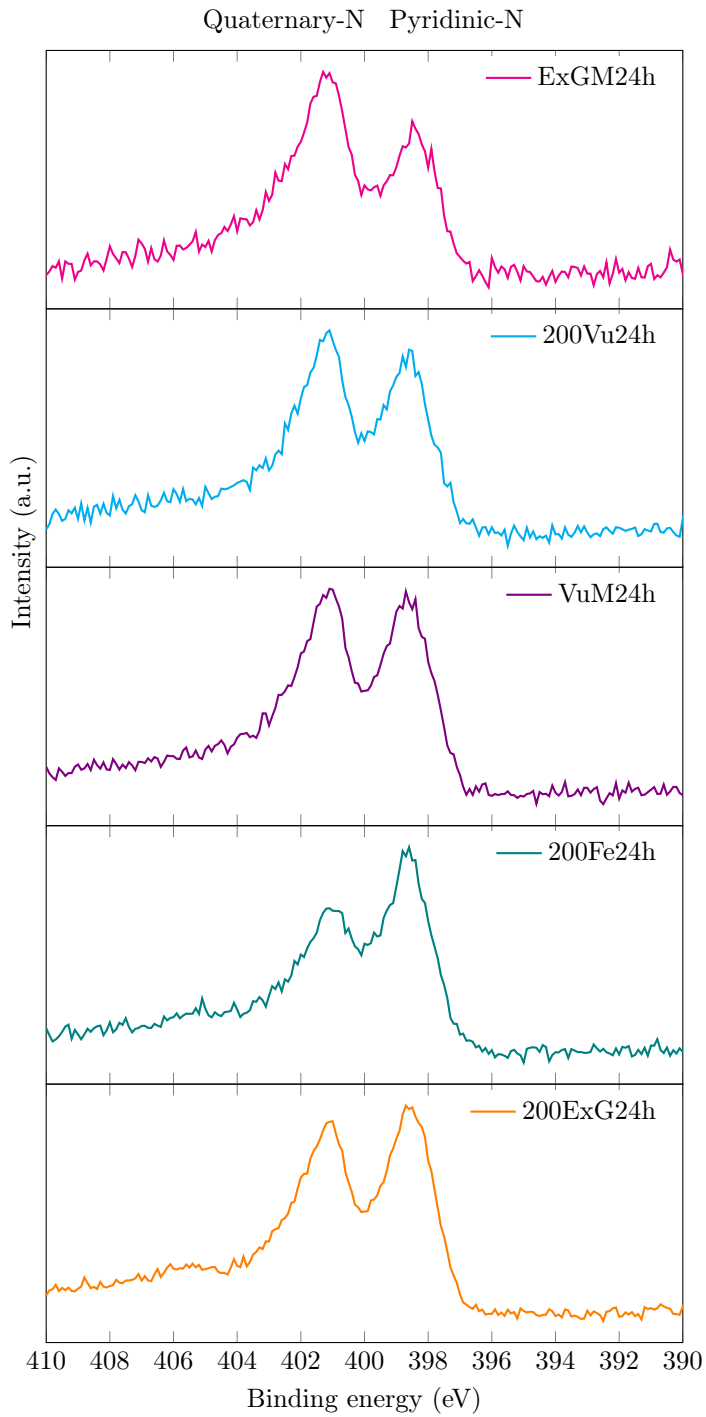| Sample name	N [at%]	O [at%]	Fe [at%]
ExGM24h	1.4	0.6	0.1
200Vu24h	2.4	1.0	0.1
VuM24h	2.8	1.4	0.1
200Fe24h	2.8	2.2	0.2
200ExG24h	3.5	2.0	0.2

Figure 5.12: XPS: N 1 s spectra with an increasing N content for ExGM24h ——, 200Vu24h ——, VuM24h ——, 200Fe24h ——, and 200ExG24h ——. The two peaks represent quaternary-N and pyridinic-N.

5.6   Thermogravimetric analysis

Figure 5.13 compares the mass changes for the synthesized samples, and Figure 5.14 compares the same samples but based on their belonging derivative of the mass. The derivative was calculated by the TGA data processing software Proteus 200Fe24h was not analyzed as not enough sample was left to conduct the analysis. Table 5.5 summarizes the maximum temperature from Figure 5.14. As many of the samples have quite a broad top, the listed temperatures in Table 5.5 corresponds to the maximum of the derivative. Detailed graphs for each sample, including the DSC and MS measurements can be found in Figures B.5 to B.12 in Appendix B.

Table 5.5: TPO: The N-CNFs are burnt of at lower temperatures on vulcan carbon compared to expanded graphite, which is illustrated by the temperature of the maximum derivative of the first peak from Figure 5.14.

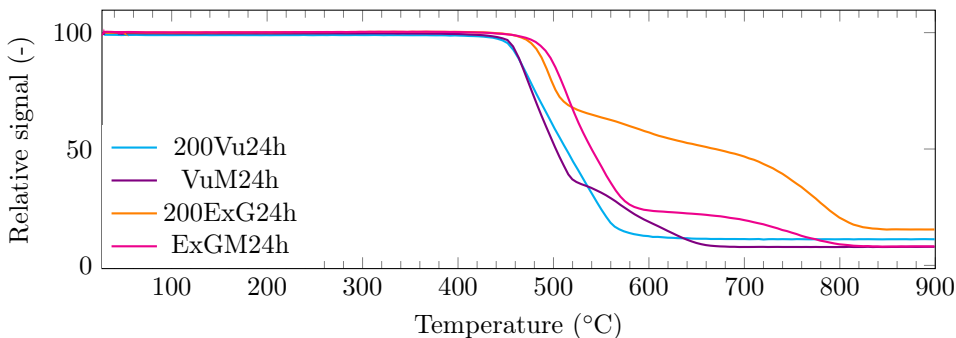| Sample name	Maximum temperature (°C)
VuM24h	464
200Vu24h	478
200ExG24h	493
ExGM24h	507

Figure 5.13: TPO: The mass of the samples is burnt of with increasing temperature in an oxidizing environment. This is illustrated by the mass changes for 200Vu24h ——, VuM24h ——, 200ExG24h —— and ExGM24h —— as a function of temperature.
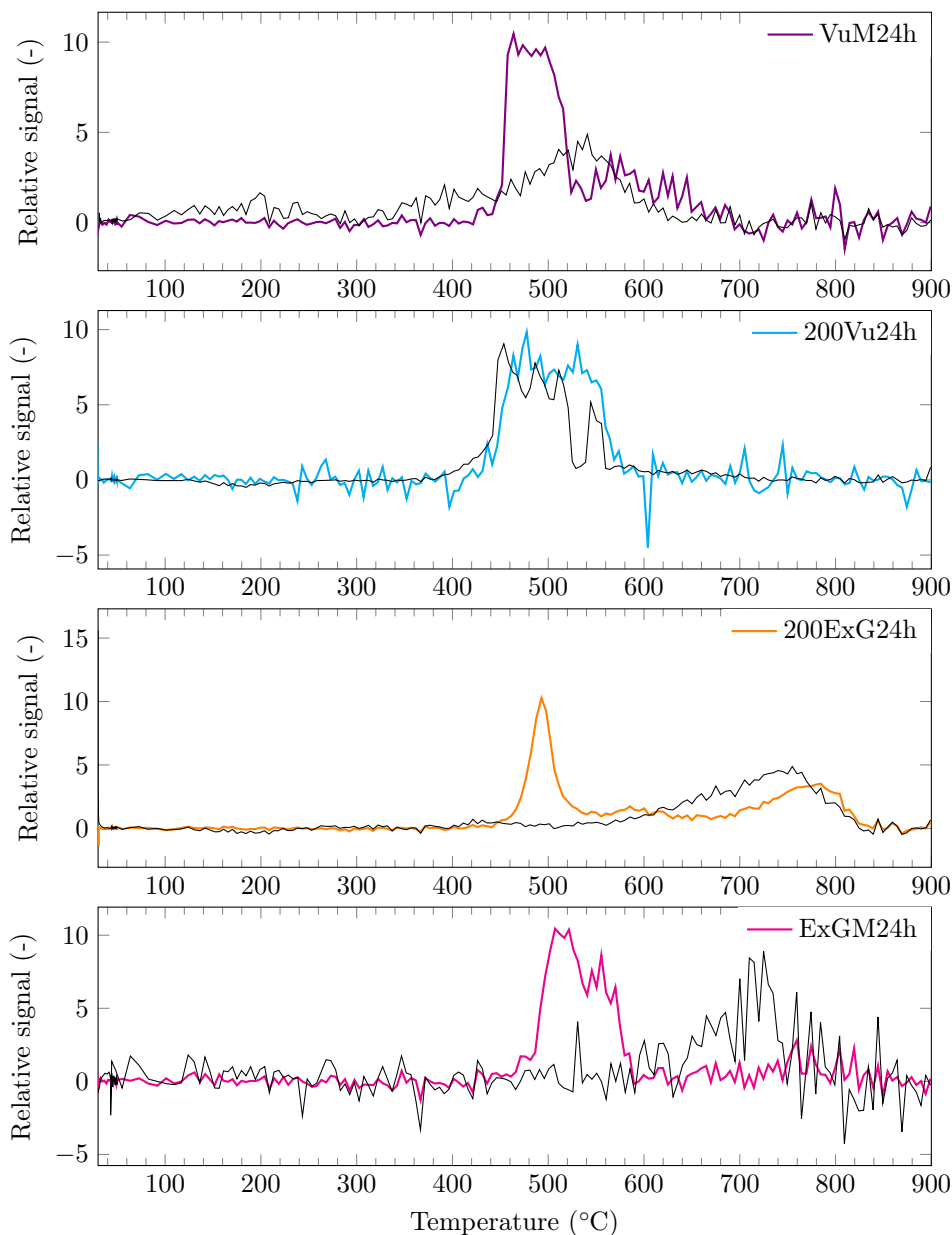
Figure 5.14: TPO: Nitrogen-doped carbon nanofibers are burnt of at lower temperatures with vulcan carbon as support (———,———) compared to expanded graphite (———,———). This is illustrated by the comparison of derivatives of the mass changes from Figure 5.13 as a function of temperature. The black curve in each plot illustrates the derivative of the sample before the N-CNF synthesis.

5.7   Scanning transmission electron microscope

The images from the scanning transmission electron microscope (S(T)EM) for the
N-CNFs grown are illustrated in Figure 5.15 to Figure 5.27. EDX images are illus-
trated in Figures 5.28 to 5.30. Only some few representative images are illustrated
for each sample, and for more images the reader is referred to Appendix E.

200Fe24h

Figure 5.15a illustrates the different structures that were found in 200Fe24h: ag-
glomerated FeNPs, small N-CNFs with clear bamboo structure, large N-CNFs with
fishbone structure and intermediate N-CNFs with tendency towards bamboo struc-
ture. The FeNPs average diameter is about 86 nm compared to 12.9 nm before the
synthesis, based on counts from Figure E.5. Figure 5.15b presents a close up of
small N-CNFs with clear bamboo structure. The two visible FeNPs on top of the
fibers have a diameter of 56.5 nm and 35.4 nm with a belonging fiber diameter of
50 nm and 41.8 nm (from top and down). Figure 5.16a illustrates a N-CNF with a
distorted bamboo structure in the front and a perfect bamboo structure in the back,
whereas Figure 5.16b illustrates a thickened N-CNF with bidirectional growth and
a total length of about 2.7 µm.

(a)   (b)
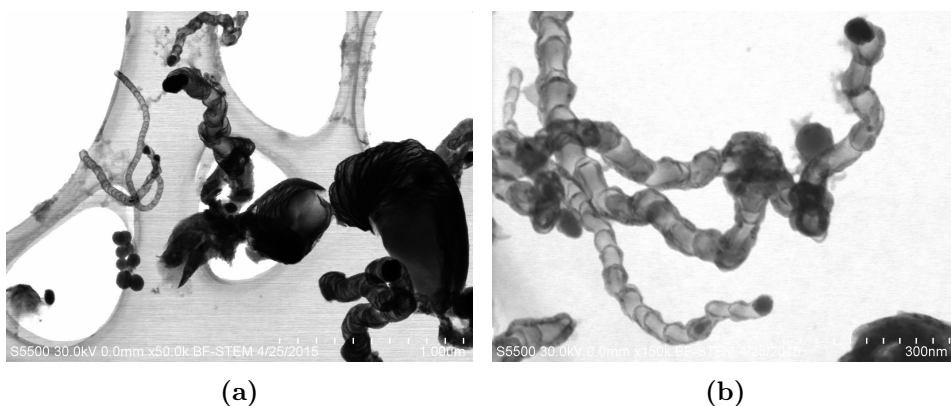
Figure 5.15: S(T)EM 200Fe24h: (a) Characterizing structures for the sample:
free-standing FeNPs, bamboo, defect bamboo and thickened N-
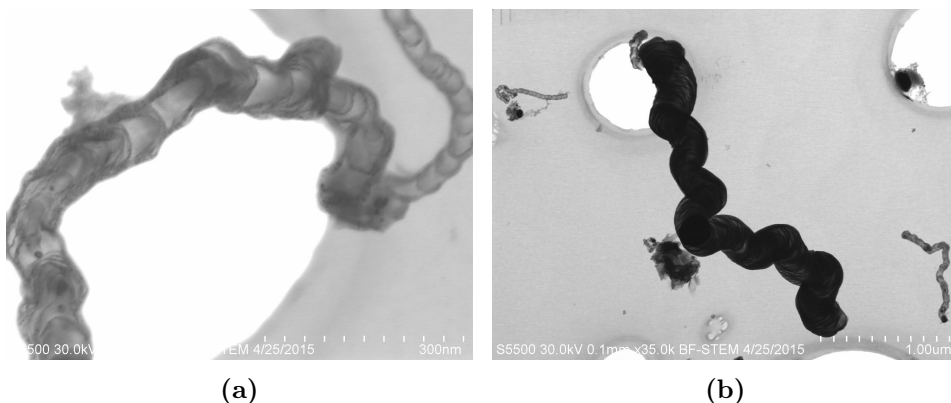CNFs (b) Regularly stacked bamboo structure.

(a)   (b)

Figure 5.16: S(T)EM 200Fe24h: (a) Close-up of an unregular bamboo structure
with some visible FeNPs within (b) a long thickened N-CNF grown
with bidirectional growth from one FeNP. The length of the fiber
is estimated to be about 2.7 μm, and the diameter of the FeNP is
237 nm.

200ExG24h

Figures 5.17 to 5.19 illustrate the different structures found in 200ExG24h in both
SE-mode and BF-mode. Small N-CNFs with clear bamboo structure, intermediate
N-CNFs with fishbone structure and thickened N-CNFs.

Figure 5.17 presents clustered N-CNFs on support with clearly visible FeNPs both
on top and within the N-CNFs. The diameter of the N-CNFs range from about
80 nm to 130 nm. The length of the N-CNF in Figure 5.18a is measured to be
around 7.47 μm by the S(T)EM software, and the diameter of the N-CNFs in Fig-
ure 5.18b range from 135 nm to 165 nm for the fishbone N-CNFs and 40 nm to 50 nm
for the bamboo N-CNFs. Figure 5.19a illustrates two N-CNFs, where the largest
N-CNF has tendency towards bamboo structure with clearly visible compartments,
and the smaller has a hybrid structure between bamboo and either MWCNT or
ribbon. Figure 5.19b illustrates a large N-CNF with a diameter of about 330 nm
and what appears to be unreacted FeNPs (on the right side of the N-CNF).

The images displayed in Figures 5.18 and 5.19 are given in Figures E.6 to E.9
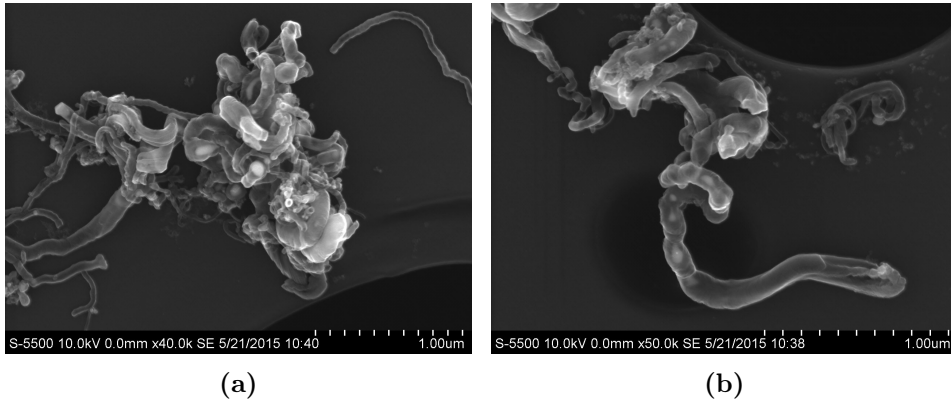in full scale in order to enhance the readability of the belonging scale.

S-5500 10.0kV 0.0mm x40.0k SE 5/21/2015 10:40   1.00um

S-5500 10.0kV 0.0mm x50.0k SE 5/21/2015 10:38   1.00um

(a)   **(b)**

Figure 5.17: S(T)EM 200ExG24h: SE images of clustered N-CNFs with clear visible FeNPs both on top and within the N-CNFs.

S5500 30.0kV 0.1mm x9.00k BF-STEM 4/25/2015   5.00um

S5500 30.0KV 0.1mm x90.0k BF-STEM 4/25/2015   500nm

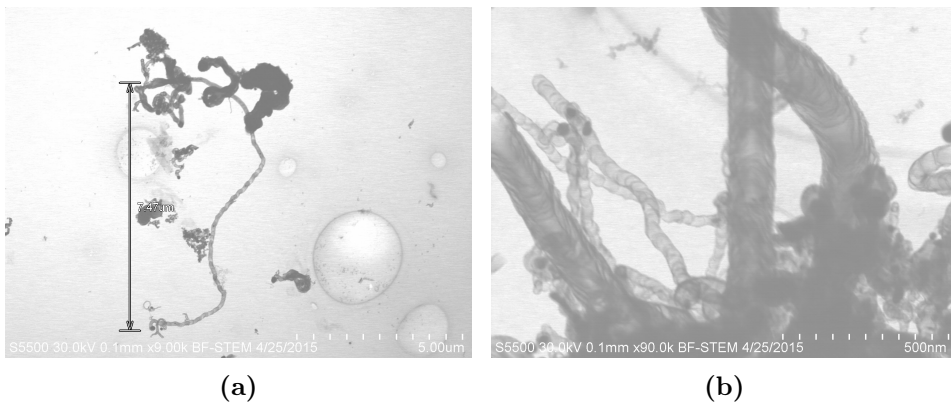**(a)**   **(b)**

Figure 5.18: S(T)EM 200ExG24h: (a) A 7.47 µm long N-CNF with bamboo strucuture and some larger thickened N-CNFs in the upper part (b) N-CNFs with FeNPs on top and bamboo (in the back) and fishbone structure (in the front).
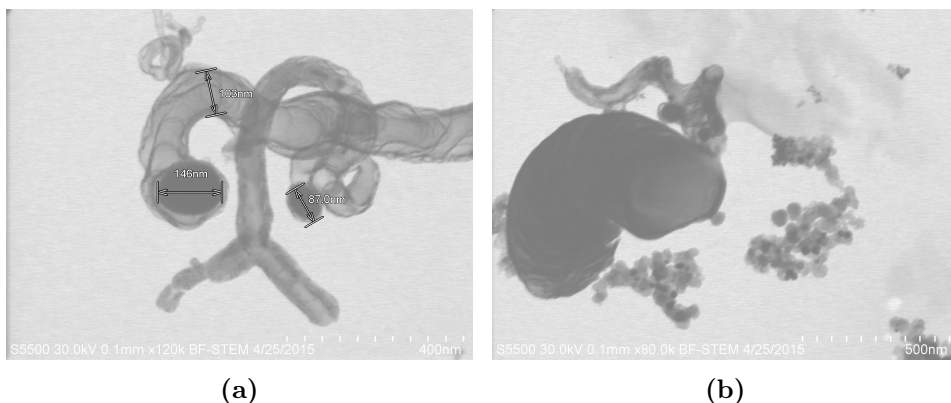
(a)   (b)

Figure 5.19: S(T)EM 200ExG24h: (a) A closeup of Figure 5.18a. Two N-CNFs with indicated FeNP diameter and fiber diameter. The largest N-CNF has tendency towards bamboo structure with clearly visible compartments, and the smaller has a hybrid structure between bamboo and either MWCNT or ribbon. (b) A large thickened N-CNFs, smaller N-CNFs and FeNPs deposited on support.

ExGM24h

The S(T)EM images for ExGM24h are illustrated in Figures 5.20 and 5.21. The most abundant structure is multi-walled carbon nanotube (MWCNT), which is clearly illustrated in Figure 5.20. Figure 5.20 is a close-up of Figure E.13 and illustrates both MWCNTs and iron particle on a graphite flake. Most of the iron particle are encapsulated by a graphite layer, which is seen as a light gray ring around the particle. The iron particles trapped inside the N-CNTs are often either stretched or have a droplet structure, compared to the round structure of the free-standing iron particles. The diameter of the N-CNFs range from 30 nm to 80 nm and 20 nm to 80 nm for the iron particles, making them resembling the FeNPs.

Another characteristic feature are N-CNFs with distorted structures, which is illustrated by Figure 5.21. Figure 5.21a shows a N-CNF which changes structure from a MWCNT to a bamboo structure. There are also three entrapped iron particles which are clearly visible. An EDX scan of the area is shown in Figure E.21b. Figure 5.21b illustrates a distorted structure which has an iron particle at top and other entrapped within the structure. The structure starts with a slightly defected bamboo structure and changes to what seems to be a hybrid between MWCNT and fishbone structure, or a thickened fiber with a core MWCNT structure.
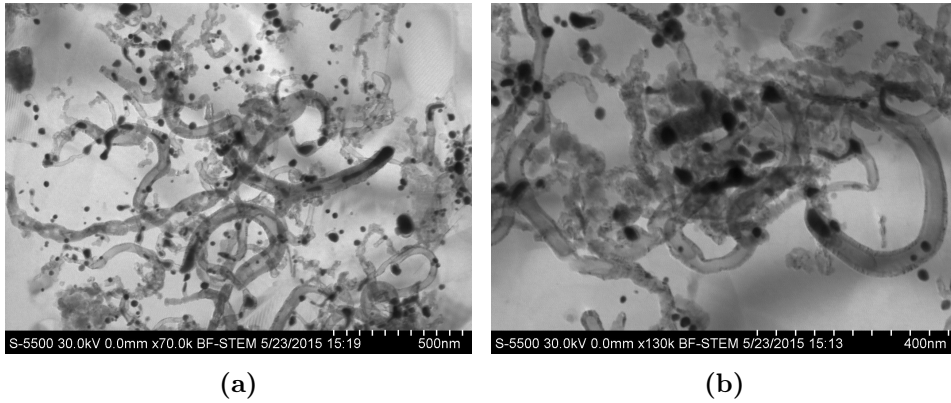
S-5500 30.0kV 0.0mm x70.0k BF-STEM 5/23/2015 15:19   500nm

(a)

S-5500 30.0kV 0.0mm x130k BF-STEM 5/23/2015 15:13   400nm

(b)

Figure 5.20: S(T)EM ExGM24h: Smaller fibers with mostly MWCNT structure and iron particles entrapped. Some fibers also show tendency towards bamboo structure. The dark dots are unreacted iron particles. Both images are a closeup of Figure E.13.
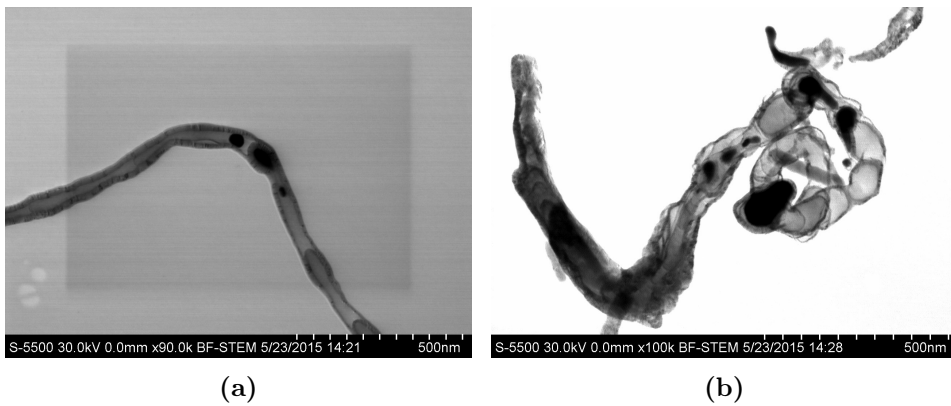

S-5500 30.0kV 0.0mm x90.0k BF-STEM 5/23/2015 14:21   500nm

(a)

S-5500 30.0kV 0.0mm x100k BF-STEM 5/23/2015 14:28   500nm

(b)

Figure 5.21: S(T)EM ExGM24h: (a) A N-CNF with entrapped iron particles and a clear shift from MWCNT to bamboo structure (b) A distorted structure that resembles bamboo and MWCNT with entrapped iron particles. The end of the N-CNF also show tendency towards a thickened fiber.
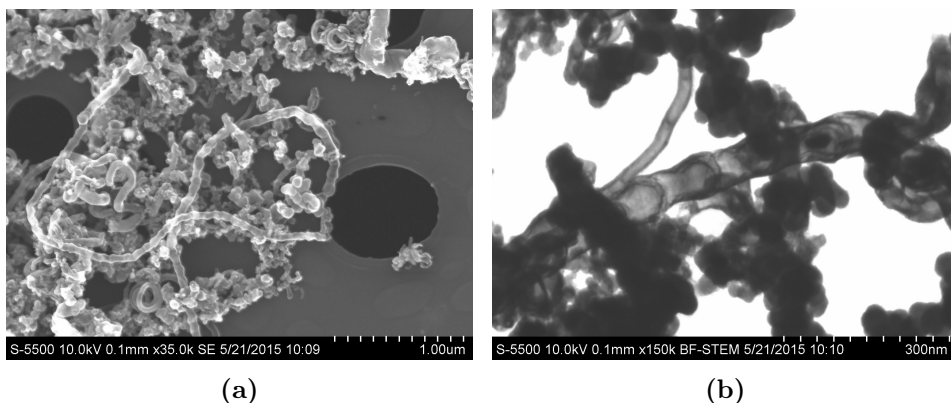
(a)   **(b)**

Figure 5.22: S(T)EM 200Vu24h: (a) SE image of a cluster of N-CNFs attached to the support. A long fiber with clearly visible bamboo structure is visible on top. (b) BF image of two fibers in between the support with different structure. The fiber in front has a clear bamboo structure, whereas it is difficult to determine the structure of the fiber in the back.

200Vu24h

200Vu24h consist primarily of smaller N-CNFs with different structures and some larger N-CNF as illustrated by Figures 5.22 to 5.24. The structure of the smaller N-CNFs are mostly either bamboo (Figure 5.24a), fishbone, or a mixture of both (Figure 5.23b).

Most of the N-CNFs are found in clusters together with the support as illustrated by Figures 5.22a and 5.24a. The N-CNFs displayed in Figure 5.22a have a diameter ranging from 50 nm to 90 nm. Figure 5.22b illustrates a close up of a N-CNF with bamboo structure and entrapped FeNP entangled between the support. Figure 5.23 presents two small N-CNFs. The N-CNF in Figure 5.23a has a diameter of about 60 nm and a clear bamboo structure with entrapped FeNPs, whereas the N-CNF in Figure 5.23b has a diameter of about 30 nm and a change in the structure from bamboo on the top to fishbone. Figure 5.24b illustrates some of the larger N-CNFs, where one of the fibers has clearly FeNPs entrapped within (seen as bright spots). Another fiber has an interesting braid structure and it is unclear whether it is one or two fibers interlaced.
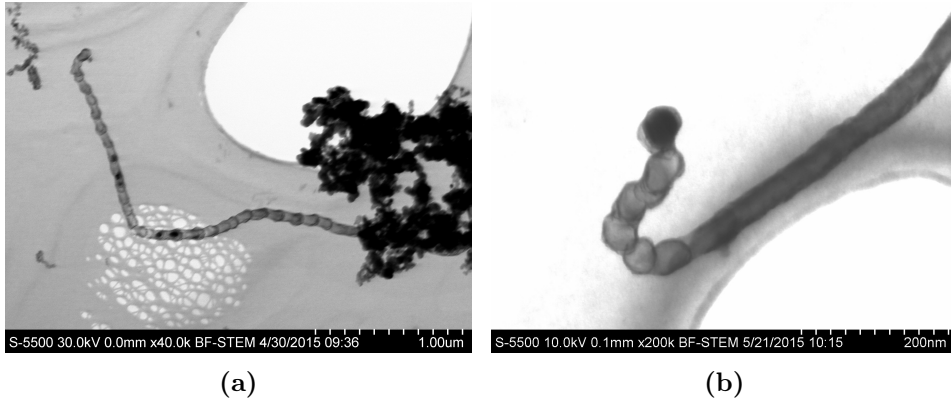
Figure 5.23: S(T)EM 200Vu24h: (a) a 2.5 µm long fiber with bamboo structure and entrapped FeNPs with a diameter of about 35 nm, (b) a N-CNF with a FeNP with a diameter of 48 nm on top and bamboo structure in the first part and fishbone structure in the rest.
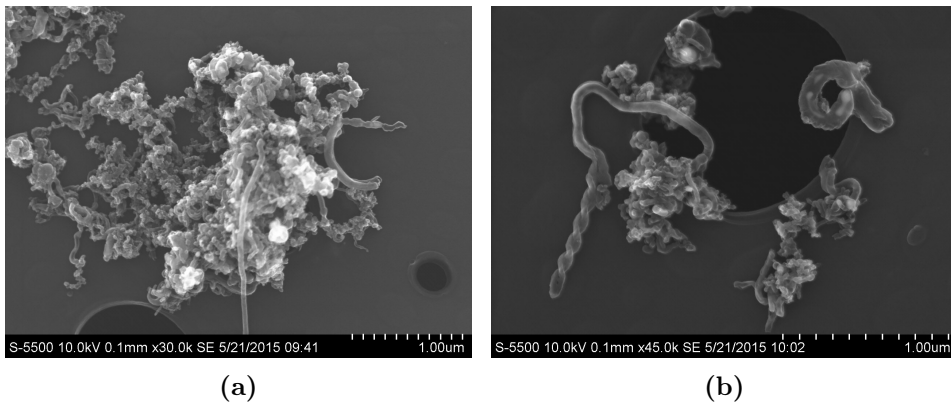

Figure 5.24: S(T)EM 200Vu24h: (a) a cluster of N-CNFs attached to the support, (b) Larger N-CNFs with different structures, including a braid strucutre.
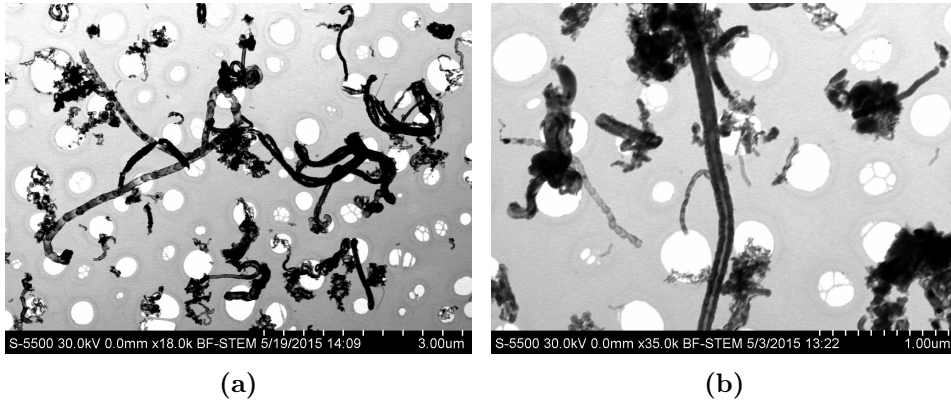
(a) (b)

Figure 5.25: S(T)EM VuM24h: (a) An overview of different N-CNFs found in the sample: bamboo, thickened N-CNFs, and MWCNTs (b) A close up of a MWCNT. Fibers with bamboo structure are also visible.

VuM24h

The sample VuM24h is characterized by long N-CNFs as illustrated by Figure 5.25. The N-CNFs display bamboo structure (Figure 5.25a), fishbone structure, MWC-NTs (Figure 5.25b) and changes between them (Figure 5.26) as seen with the other samples.

The N-CNFs in Figure 5.25a have a diameter range of 100 nm to 140 nm for the larger N-CNFs, and 40 nm to 80 nm for the smaller N-CNFs. Many of the larger N-CNFs have a distorted structure and most of the N-CNF are not attached to the support. Figure 5.25b illustrates a N-CNF with a MWCNT structure, which shows tendency towards thickening as the walls are quite thick. The N-CNF is surrounded by smaller bamboo structured N-CNFs with iron particles on top. Figure 5.26 displays two different images of the same N-CNF, which has changed structure during growth from fishbone (Figure 5.26a) to bamboo (Section 5.7). Furthermore, two interesting structures were also observed: octopus (Figure 5.27a) and a braid structure (Figure 5.27b).

(a)

(b)

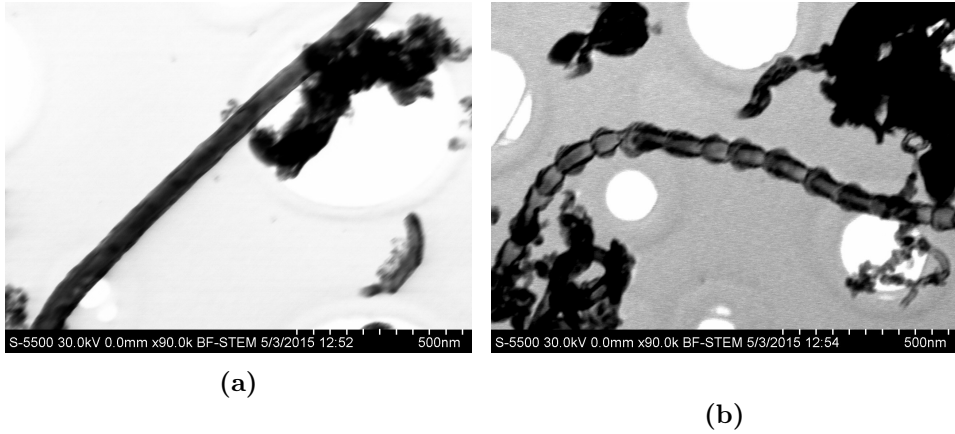**Figure 5.26:** S(T)EM VuM24h: the same N-CNF but with different structure (a) fishbone structure (b) bamboo structure.

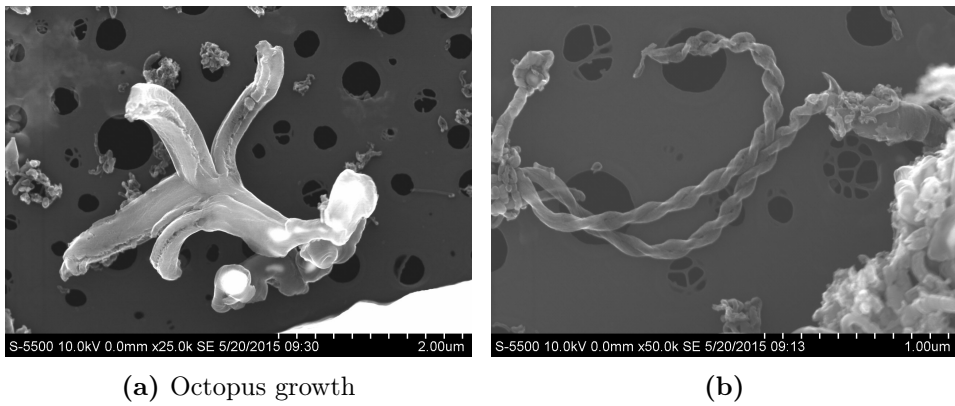**(a)** Octopus growth   **(b)**

Figure 5.27: S(T)EM VuM24h: (a) Octopus growth, (b) braid structure.

EDX

The following images are taken from the two samples VuM24h and 200ExG24h, but are believed to be representative for ExGM24h and 200Vu24h too. Figure 5.28 illustrates two N-CNFs where the tip has a droplet-shaped FeNP on top. Figure 5.29a show a cluster of N-CNFs for VuM24h, and Figure 5.29b illustrates the cross section of a fiber with fishbone structure. In Figure 5.30 the N-CNF show tendency towards bamboo structure and has clearly iron particles trapped within, which is also confirmed by the EDX scan.
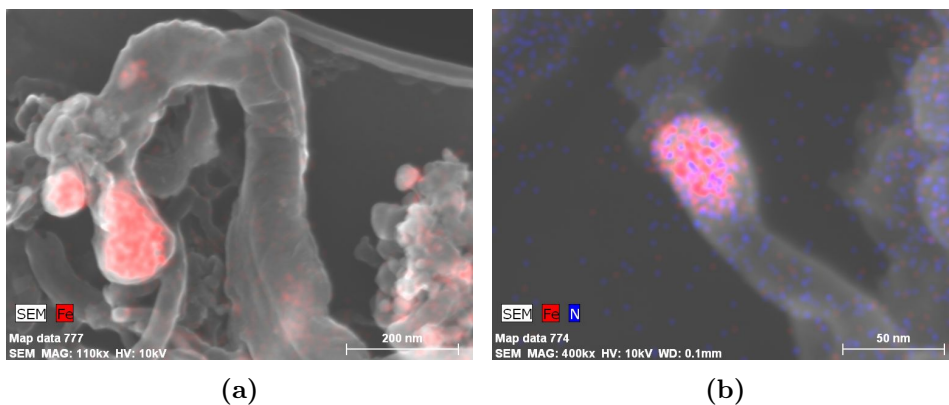

(a)

(b)

Figure 5.28: EDX: (a) 200ExG24h: N-CNF with a droplet shaped FeNP on the tip (b) VuM24h: N-CNF with a droplet shaped FeNP on the tip.
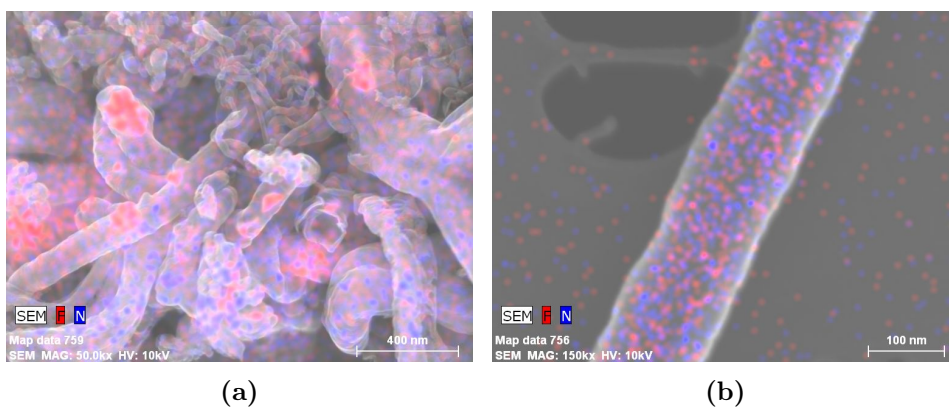

(a)

(b)

Figure 5.29: EDX: (a) VuM24h: cluster of N-CNFs on support with detected nitrogen and iron on the tip of the fibers (b) 200Vu24h: fiber with detected nitrogen and atomic iron.
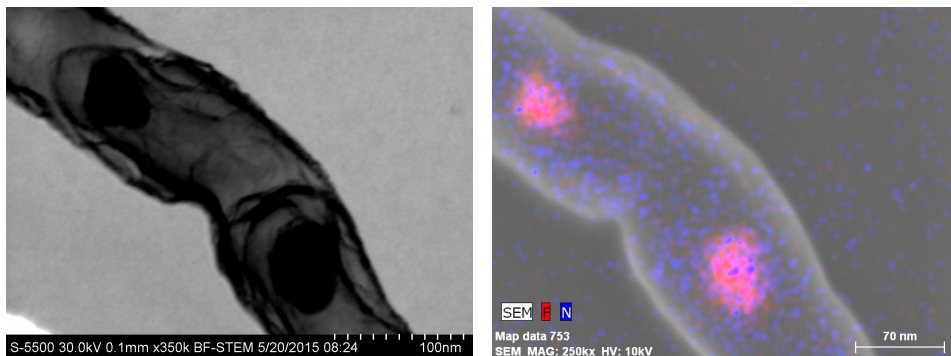
Figure 5.30: EDX VuM24h: Iron particles trapped within a fiber with bamboo structure.

5.8   BET

The surface area and the cumulative volume of the pores between $17\,\text{Å}$ and $3000\,\text{Å}$ was calculated by the BET desorption isotherm and are displayed in Table 5.6. Again, 200Fe24h was not measured due to lack of sample.

Table 5.6: The total surface area and the cumulative surface area of the pores between $17\,\text{Å}$ and $3000\,\text{Å}$ at desorption for the synthesized samples.

Sample name	Surface area [m²/g]	Average volume of the pores [cm²/g]
200Vu24h	180.44	0.446
VuM24h	153.23	0.348
ExGM24h	157.29	0.165
200ExG24h	64.72	0.267

5.9   Electrochemical measurements

Figure 5.31 illustrates the linear sweep voltammogram for the corrected current (the disk current subtracted from the background current) for all samples. Table 5.7 presents the value for the onset potential for the different samples. Detailed scans can be found in Appendix F, including a closeup of the onset potential area.

The onset potential is quite similar for all samples (ranging from $0.92\,\text{V}$ to $0.88\,\text{V}$). 200Vu24h is the most active sample followed by VuM24h, and 200Fe24h the least active. From Figure 5.31 it is difficult to say whether there is any difference in activity between 200ExG24h and ExGM24h, as they lay close enough that the difference could be due to experimental factors.

Table 5.7: The onset potenial varies with the support and iron source used.

Sample name	Onset potential (V)
200Vu24h	0.92
VuM24h	0.92
200Fe24h	0.90
200ExG24h	0.90
ExGM24h	0.88
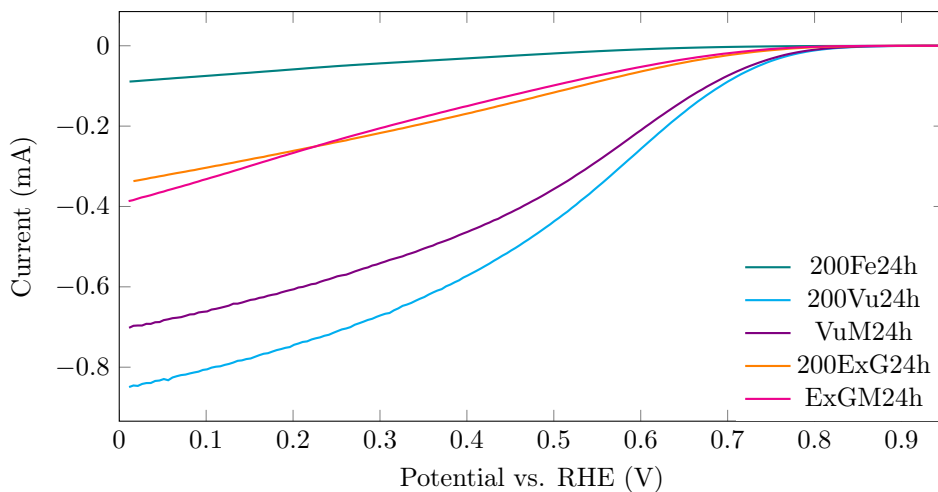
Figure 5.31: The Linear sweep voltammogram, where the produced current and activity for the oxygen reduction reaction differed with the use of different supports and iron source. Both activity and the onset potential was highest for the vulcan sample with iron nanoparticles (——) followed by vulcan with iron particles (——), the two expanded graphite samples (——,——), and last the sample with iron nanoparticles without support (——). The measurements were performed at a scan rate of $5\,\mathrm{mV/s}$ and a rotation rate of $1600\,\mathrm{rpm}$ in a O_2 saturated electrolyte.
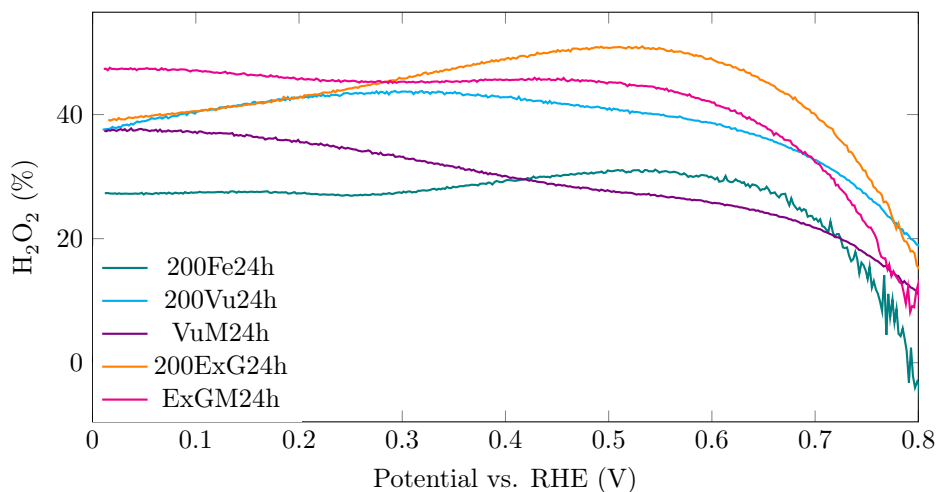
Figure 5.32: Produced H_2O_2 during the linear sweep measurement varies with the support and iron source of the sample and the voltage. 200Fe24h ——, 200Vu24h ——, VuM24h ——, 200ExG24h ——, ExGM24h ——.

To calculate the amount of H_2O_2 produced during the ORR reaction, Equation (5.2) was used.

$$H_2O_2\,(\%) = 200 \times \frac{I_r/N}{I_r/N + |I_d|} \tag{5.2}$$

In equation Equation (5.2) I_r and I_d are the ring and disk currents respectively, and N is the collection efficiency of the ring electrode, which is 20 %. Figure 5.32 illustrates the produced H_2O_2 for all samples.

Fuel cells operate at lower overpotentials (between 0.5 V and 0.7 V), resulting in the lowest H_2O_2 production for VuM24h and highest for 200ExGM24h.

CHAPTER 6

DISCUSSION

6.1 Synthesising iron nanoparticles

The aim of the iron nanoparticle synthesis was to produce homogeneous FeNPs with a uniform size distribution. By varying the synthesis temperature and heating ramp, the intention was to produce larger homogeneous FeNPs. Results from the specialization project conducted the fall of 2014 and ongoing research suggested that the FeNPs should be in the range of about 50 nm in order to grow N-CNFs which would produce acceptable activities. However, the FeNPs tested in the project were not deposited on any support, and the ongoing research uses iron nitrate instead of FeNPs as the iron source. Thus the suggestion might have given some misleading guidance [44, 61]. All produced FeNPs are spherical, and as they were not dried before use, they do not have a distinguished oxide layer, as illustrated in Figure 2.7. The FeNPs are still core-shell particles, but the shell is difficult to detect as it is thin.

The FeNPs synthesized from 200Fe were the largest FeNPs (9.7 ± 0.5 nm) with the most uniform size distribution produced. They were thus chosen as the base for the growth catalyst for the synthesis of N-CNFs. The different diameter and degree of homogeneity of the FeNPs is caused by the different reaction conditions. RTFe yielded the largest FeNPS, but also the least homogeneous (Figures 5.1 and 5.2). During their synthesis, the FeNPs had a long nucleation and growth process as the reaction mixture was slowly heated up to the synthesis temperature ($3\,^\circ\text{C}\,\text{min}^{-1}$ up to $200\,^\circ\text{C}$). Consequently the FeNPs had time to agglomerate, resulting in larger FeNPs and less homogeneous particles [27].

260Fe yielded smaller FeNPs than 200Fe, which is attributed to the higher synthesis temperature and heating ramp. Although the iron precursor was added at a lower temperature ($120\,^\circ\text{C}$ vs. $200\,^\circ\text{C}$), the heating ramp up to the synthesis

temperature of 260 °C for 260Fe was high ($10\,°C\,min^{-1}$). Hence, the FeNPs had a shorter nucleation and growth time compared to 200Fe, resulting in smaller FeNPs.

The program Image J was used to analyze the size distribution. This is not optimal, as the used images needed to be greatly modified. Smaller particles were omitted from the analysis and nearby particles were merged together, resulting in an inaccurate size distribution. However, the margin of error is not considered to be significant, and the presented size distributions are believed to be sufficiently accurate.

6.2 Impregnation

To distinguish between the samples impregnated with FeNPs and iron nitrate, the terms FeNPs is solely going to be used for the samples 200ExG and 200Vu, whereas the iron in the samples ExGM and VuM will be denoted as iron particles.

During the FeNP synthesis, different iron compounds were formed as byproducts, making it difficult to calculate the iron loading on the support based on synthesis data. Consequently the loading had to be adjusted by trial and error using TPO in order to produce samples with a loading of about 20 wt%. As an example, a loading of 58.95 wt% was calculated for 200ExG based on the synthesis data, but the TPO measurements revealed an actual loading of 16.4 wt%. Despite the trial and error method, all samples had almost identical iron loadings, making them comparable.

As it was impossible to disperse all FeNPs by sonification, residual FeNPs were left behind in the beaker for both 200ExG and 200Vu. This may cause irregular loadings and difficulties to replicate the samples for future experiments.

6.3 Checking for agglomeration

Based on the calculation with the Scherrer equation from Figure 5.6 and the particle size distribution from Figure 5.8, the diameter has increased by about 15 nm for 200Vu and 30 nm to 50 nm for 200ExG. Comparing the particle size for all samples (Table 5.2), ExGM yields the smallest iron particles. Although ExGM was reduced at a lower temperature combined with a lower heating rate, it is reasonable to assume that ExGM also has the smallest iron particles prior to synthesis start. As the same iron particles and FeNPs are impregnated on vulcan carbon, the same trend, with the iron particles being smaller than the FeNPs, is also thought to be valid for VuM and 200Vu.

Additionally, the XRD scans for both 200ExGRed and 200VuRed indicate that the FeNPs have become more crystalline during the reduction. This is clearly visi-

ble when comparing the scan with a scan for pure FeNPs, as shown in Appendix C
Figure C.2. The scan was performed for the specialization project conducted in
the fall using the same FeNPs, but in a dried state. Comparing the peaks at about
45° for 200ExGRed and ExGMRed and the lacking peak at about 65° for 200Ex-
GRed, there is a clear indication that the iron particles are more crystalline than
the FeNPs. It is reasonable to assume that the iron particles are more crystalline
than the FeNPs for the vulcan sample too, despite the lack of a XRD scan for VuM.
The more distinct Fe peaks for 200VuRed are a result of the amorphous carbon in
vulcan carbon. For expanded graphite, the crystalline carbon overshadows the Fe
signals due do its higher crystallinity. This results in lower Fe peaks in terms of
intensity, compared to Fe on vulcan carbon.

Interestingly, the homogeneous FeNPs that were deposited on expanded graphite
are no longer homogeneous in size after reduction. This is clearly illustrated by
the size distributions given in Figure 5.11, resulting in a non-homogeneous start-
ing system prior the N-CNF synthesis. Although the cooling down process of the
samples may have distorted the results, the starting system is still thought to be
non-homogeneous.

The program used for calculating the crystal size for 200Vu only calculates the
average diameter. It is not clear whether all FeNPs have become crystalline and to
which extend, making it difficult to estimate the minimum and maximum diame-
ter for 200Vu. More, the program does not adjust for the instrument broadening
and the calculated crystal size can only be seen as a rough estimate for the FeNP
particle size.

ExGMRed was not passivated under a O_2flow after the reduction, and this may
explain the color gradients in the particles. The gradient is believed to be a result
of a formed oxide layer.

6.4   N-CNF synthesis

Previous results with iron nitrate have concluded with an optimal synthesizing tem-
perature of $650\,°C$ combined with a heating rate of $3\,°C\,min^{-1}$ in order to achieve
both a sufficient yield and activity [44]. However, a temperature of $750\,°C$ com-
bined with a higher heating ramp ($15\,°C\,min^{-1}$) was chosen with the expectation of
an increase in the yield and a decrease in the potential agglomeration of the FeNPs.
These assumptions were based on preliminary results with FeNPs without support
[61]. As mentioned in above, agglomeration was not avoided, but it is thought that
the FeNPs would have agglomerated more severe with a lower heating ramp.

The yield was lowest for 200Fe24h and highest for ExGM24h, as seen from Ta-
ble 5.3. However, 200Fe24h was produced at $650\,°C$ and ExGM24h had a lower

heating ramp, making them not directly comparable with the other samples. The lower heating rate of ExGM24h may have affected the agglomeration of the iron particles and thus the growth process. Nevertheless, a size distribution for ExGM should be conducted in order to confirm the hypothesis. From the samples produced at the same conditions, VuM24h had the highest yield followed by 200Vu24h and 200ExG24h. Interestingly, both samples impregnated with iron nitrate had almost the same yield, despite the different heating ramp.

The two samples impregnated with FeNPs differed more with respect to yield. One possible explanation might be the lower Fe loading of 200ExG24h compared to 200Vu24h, but the difference in support is thought to have a larger impact. This is supported by the calculated diameters of the reduced samples, which indicate a stronger support-interaction for vulcan compared to expanded graphite, as the average FeNPs was smaller.

As described in Section 2.2, carbon nanofibers is a collective term for many different structures, including carbon nanotubes. Thus N-CNF will be used as a collective term rather than a description of a certain structure in the following sections.

6.5   X-ray photoelectron spectroscopy

The results from the XPS (Table 5.4) strongly indicates the incorporation of nitrogen and oxygen to the grown N-CNFs. Figure 5.12 proves the incorporation of two nitrogen structures (quaternary-N and pyridinic-N) which are believed to be essential for activity.

200Fe24h has among the highest nitrogen and oxygen content despite having the lowest yield of N-CNFs, and will be discussed in Section 6.7. This indicates that the grown N-CNF will have a structure associated with hydrogen and heteroatoms, e.g. bamboo or fishbone. Both vulcan carbon samples, 200Vu24h and VuM24h, show almost identical nitrogen-peaks and report the same amount of both nitrogen and oxygen, despite having very different yields ($5.60\,\mathrm{g/g_{cat}}$ and $7.25\,\mathrm{g/g_{cat}}$). This indicates a similar structure for the grown N-CNFs, and will again be discussed in Section 6.7.

The results for the two expanded graphite samples are quite different: 200ExG24h has the highest nitrogen content compared to the others, but also the lowest quaternary-N peak and yield of the samples with support, whereas ExGM24h has the highest yield of N-CNFs, but by far the lowest nitrogen content and pyridinic-N peak. The grown N-CNFs are thus thought to have different structures, but this will be discussed further in Section 6.7.

When measuring the signals for XPS, the photon only enters a certain depth of the

surface area of the sample, hence only revealing the surface composition. Thus, the iron reported in Table 5.4 is surface iron. For all samples except ExGM24h, the iron is denoted to be iron oxide, while metallic for ExGM24h. As the amount of iron detected on the surface is almost the same for all samples, despite the different yields, this suggest that most of the iron is encapsulated by carbon. The encapsulation can either take place during the synthesis or the cooling down.

6.6 Temperature programmed oxidation

From Figures 5.13 and 5.14 it is clearly visible that all samples have different burning curves. In general, the first shoulder represents the burning of the N-CNFs, whereas the second shoulder represents the burning of the support. This is also confirmed by the MS measurements found in Appendix B, as there are clear NO and NO_2 tops for all samples corresponding to the first shoulder. There are also often a NO_2 top corresponding to the second shoulder, but this is believed to be mainly CO_2, as CO_2 and NO_2 are close in molecular weight.

200ExG24h has the lowest yield which is confirmed by a high first shoulder. For 200Vu24h only one shoulder is observed, but this is probably due to the simultaneous burning of the support (Figure 5.14). By comparing the derivative curves before growth (black curves) for 200Vu and VuM, a difference in the burning temperature of the support is noted. This difference is attributed to the catalyzing property of iron in connection with the burning carbon. Additionally, there are also clear indications that FeNPs and iron nitrate particles have different effects on the burning properties of vulcan carbon when comparing the two curves with TPO curves from the literature [62, 63]. This indicates that the iron particles and FeNPs have different characteristics, which may be due to difference in crystallinity or size as indicated by the XRD scans, or also the nitrogen and oxygen content. A similar difference is seen for 200ExG and ExGM, but not as pronounced. It is not clear why the samples ExGM24h, 200Vu24h and VuM24h have significant more noise in the plots than 200ExG24h.

6.7 Scanning transmission electron microscope

With the use of uniformed FeNPs as the base of the growth catalyst for the N-CNF synthesis, uniform N-CNFs with a narrow size distribution were also expected. However, this is clearly not the case as seen from the S(T)EM images, and there are many possible reasons which will be discussed below. The first reason might be the non-uniform system after reduction which the S(T)EN images after reduction revealed. Generating FeNPs that remain homogeneous after reduction might result in more uniform N-CNFs. However, this is thought to be difficult to achieve, as the FeNPs need to be prevented from agglomerating during impregnation and reduction.

In general, smaller N-CNFs were observed for the vulcan samples compared to the expanded graphite samples, confirming the suggestion of a stronger support-interaction for vulcan. This is partly supported by the measured particle sizes after reduction (Table 5.2), as they present a smaller particle size for FeNPs deposited on vulcan carbon compared to expanded graphite. However, the size of the iron particles deposited on expanded graphite are smaller than those for the FeNPs on vulcan carbon. As no measurements after reduction were conducted for the iron particles on vulcan carbon, it is difficult to compare the samples. Nevertheless, it is presumed that the iron particles will agglomerate more than the FeNPs during the first synthesis time. In addition, previous results have shown that the major growth of N-CNFs first starts after a longer period of time [44, 61], indicating that the particle sizes probably are not as presented in Section 5.3.

For all samples, FeNPs or iron particles were observed on the top of the grown N-CNF confirming the top growth model. As discussed in Section 2.5 it is unclear which effects the Fe and the support have regarding the diameter of the N-CNFs. Still, a general conclusion in this thesis is: That the larger the iron particle or FeNP is, the larger is the belonging fiber.

Even though smaller iron particles and FeNPs are observed without deposited on any carbon (free-standing) after the synthesis (Figures 5.17a, 5.19b and 5.20), no larger particles (above 100 nm) were observed free-standing. The larger particles are just observed attached on the top of a fiber structure. From Figure 5.8 some larger particles were detected, but not as large as the particles observed in e.g. 200ExG24h, Figures 5.17a and 5.18b. It is therefore concluded that the major agglomeration, in order to produce FeNPs in the range of µm, must take place after the reduction, and possibly before or during the growth. Combined with the fact that they are not observed free-standing it is presumed that the iron particles and FeNPs either agglomerate in collaboration with the growing N-CNF, or that the carbon deposition may determine the size of the particles. The latter has been proposed by Nolan et al. [20] and confirmed by Moodley et al. [38]. Another cause, might also be the fact that smaller particles deactivate more easily and possibly through the formation of iron nitrate with NH_3.

In general, the CNF yield (and thus also the N-CNF yield) is dependent on the initial coking rate and deactivation rate. The coking rate is governed by the surface area which in turn is governed by the particle size of Fe. Nevertheless, there is a balance between an adequate surface area and a too large surface area [64]. An adequate surface area will have a high diffusion flux area and thus a shorter diffusion length, resulting in a high coking rate and yield of N-CNFs. However, a too large surface area will have a large saturation concentration of N-CNFs which lowers the driving forces of carbon diffusion through the particle. This leads to

a low coking rate and an increase in the surface coverage of carbon, resulting in encapsulation of carbon and thus deactivation of the particle. The free-standing iron particles and FeNPs observed in most samples are presumed to have been deactivated by this route, but it is difficult to say whether it is because of their initial size, or if other factors such as changes in the Fe surface orientation have had effects. Still, this theory suggests that there might be an optimal particle size for N-CNF growth. This optimal size is probably governed by changes in the thermodynamic properties of the N-CNFs as a function of the crystal size of the Fe. Despite this theory, ExGM24h with the highest yield and lowest nitrogen content did not exhibit the highest activity (Figure 5.31). The presumptions that both the support, the nitrogen content and possibly the iron source contribute towards the activity are strengthen.

The most abundant structures for all samples are either bamboo and fishbone or MWCNTs. The bamboo structure is known to be produced for samples with a high nitrogen content, whereas MWCNTs are produced with a low nitrogen content [19]. This is confirmed by ExGM24h, which mostly contains MWCNTs and has the lowest nitrogen content. The other samples have a higher nitrogen content and thus a higher degree of bamboo structure.

All samples contain N-CNFs which suddenly have changed structure during the growth (Figures 5.20 and 5.23b). Changes in the growth conditions or a deactivation mechanism are though to be the causing effects. Many of the fibers also have one or several FeNPs or iron particles entrapped at the point where the structure changes. Presumably, the entrapped particle(s) causes a change in the growth condition and thus results in a change of the structure. Another explanation would be bidirectional growth, which is exhibited by both the fishbone and the platelet structure, as described in Section 2.2. If the iron particles or FeNPs expose different index planes on either site, this could result in different structures on either side as in Figure 5.21a. However, N-CNFs with entrapped FeNPs or iron particles and without a change in structure (Figure 5.21a) have also been observed. The fact that the particles either had a droplet shape or were outstretched (Figure 5.20) suggest that the particles were split up and are fragmented over time, rather than alternating the growth conditions by being stuck within the N-CNF. A third explanation could be the changing condition (e.g. partial pressures or yield) caused by gradient in the reaction during synthesis. This might cause the FeNPs or iron particles to change crystal structure and thus resulting in alternations of the N-CNF structure.

In the following subsections, each sample will be discussed separately and with emphasis on the structure of the N-CNFs.

200Fe24h

200Fe24h produced in average the largest N-CNFs, which mainly displayed two structures: bamboo and fishbone. Many of the observed N-CNFs show defects as a result of a lacking support interaction. Despite this, N-CNFs with non-defect structures were also observed (Figures 5.15b and 5.16a). This is in slight disagreement with Yu et al. [32] who have reported that Fe in a powder form and Fe deposited on Al_2O_3 yield different CNF structures caused by the support-interactions.

Evidently the growth catalysts with support had a much higher yield than 200Fe24h without support. This can be explained by the fact that the FeNPs are more exposed towards sintering as they lack a support-interactions which would contribute towards keeping them separated. As FeNPs dispersed on a support often expose high index planes and are smaller and more open compared to FeNPs in powder form, they tend also to form different and smaller structures than pure FeNPs [32]. Interestingly, the structures and to some extent the diameters of the N-CNFs are quite similar to the other FeNP samples with support, indicating that the FeNPs expose the same index planes both in powder and dispersed on a support. This may be due to the protective olylamine layer formed around the FeNPs during their synthesis, as it protects the magnetic FeNPs from agglomerating as discussed in Section 2.3.

Figure 5.15a displays two thickened N-CNFs and Figure 5.16b illustrates a thickened fiber with bidirectional growth. Although it is difficult to determine the structure of these fibers, the high nitrogen content of the sample indicates that the core structure could be either fishbone or bamboo rather than MWCNT. This also coincides with the possibility of bidirectional growth with the fishbone structure.

200ExG24h

Like the observation made for Fe20024h, the N-CNFs range from thin to thick (80 nm to 330 nm), and vary in size for 200ExG24h. Characteristic are long fibers with mainly bamboo or fishbone structure. According to the S(T)EM images (Figures 5.17 and 5.18), the N-CNFs mostly occur on their own without being attached to the support. However this may be misleading as they most likely have been separated from the support during the short sonication for preparing the sample.

Figure 5.19a illustrates two N-CNFs: one N-CNF with a clear bamboo structure and another twinned around the first N-CNF with partly bamboo and partly MWCNT structure. The size of the FeNP for the first N-CNF is measured to be slightly bigger than the diameter of the N-CNFs. This is probably due to carbon encapsulation forming layers around the FeNPs during the cooling down, making the diameter of the FeNP to appear bigger. As with 200Fe24h, it is difficult to determine the structure of the thickened N-CNF illustrated in Figure 5.19b. Once again, it is

reasonable to assume that the core structure could be bamboo or fishbone rather than MWCNT due to the high nitrogen content of the sample.

ExGM24h

The most observed structure for ExGM24h resembles MWCNT (Figures 5.20 and E.15b), but some N-CNFs also display bamboo structure (Figure 5.21b). Characteristic for this sample are the many N-CNFs with defects within their structure and the sudden change of structure. Furthermore, there are more iron within the fibers than observed in other samples and these iron particles are often larger or longer (Figures 5.20 and E.16). From Figure E.14 (an overview of Figure 5.20) it can be observed that the larger N-CNFs tend to grow on the edge of the support, whereas the smaller fibers tend to grow in the middle. This may be a result of a weaker support interaction at the edges compared to the middle, and the iron particles will thus easier agglomerate resulting in larger particles and N-CNFs. However, due to the sonication of the sample in the preparation process it is difficult to conclude with whether the bigger N-CNFs tend to be attached to the support or not.

Compared to 200ExG24h, the major difference is the structure of the N-CNFs, and it would be obvious to attribute this difference to the iron source. However, the lower heating ramp of ExGM24h during the reduction ($3\,^{\circ}\mathrm{C\,min}^{-1}$ vs. $15\,^{\circ}\mathrm{C\,min}^{-1}$) may have affected the characteristics of the iron particles, leading them to expose different index planes and thus producing predominant MWCNTs. As seen by Table 5.4, ExGM24h has both a lower nitrogen and oxygen content compared to the other samples. This is linked to the abundant observation of MWCNTs as they require no other element to stabilize the structure compared to the other structures [19]. The tendency towards defected bamboo- and fishbone structures is most likely due to the same cause. Both structures require a certain amount of hydrogen or other heteroatoms for stabilization, and the detect amount from the XPS is presumably not sufficient enough.

The shape of the iron particles entrapped in the N-CNFs for ExGM24h compared to others, are unique. As discussed in Section 2.2, the ribbon structure resembles the MWCNT in a S(T)EM image, making it difficult to distinguish between the two structures. The ribbon structure is characterized by having molten particles entrapped within the fibers. Comparing the iron particle in Figure 5.20 with the entrapped iron in the fibers grown by Martin-Gullon et al.[19] and Kim et al. [22], suggest that these iron particles are molten as well. This suggest that the N-CNFs in Figure 5.20 are composed of both ribbon and MWCNTs.

200Vu24h

Compared with 200ExG24h, smaller N-CNFs attached to the supports were observed for 200Vu24h (Figures 5.23a and 5.24a). Once more, this supports the claim

of stronger support-interactions between vulcan carbon and the FeNPs compared to expanded graphite. The main structures of the sample are primarily bamboo and fishbone (Figure 5.22b), which is in accordance with the indicated structures according to the nitrogen content. In addition, a more exotic structure like the braid structure in Figure 5.24b was discovered. Although this is not the norm, it shows the diversity of the fiber structures that can be grown.

VuM24h

For VuM24h, primarily long fibers with either bamboo (Figure 5.25a), fishbone (Figure 5.26a) or MWCNT (Figure 5.25b) structure were observed. Exotic structures like octopus and a braid structure (Figure 5.27) were also found, but again these structures are more a curiosity rather than the norm.

Compared to 200Vu24h, the fibers are slightly bigger in diameter, but also longer and less attached to the support. This suggest that the iron source may affect the support-interactions, and that it is are stronger for FeNPs compared to iron particles. This is also supported by the XRD scan, as they indicated a difference in crystallinity between iron particles and FeNPs. Also, the XRD results (Table 5.2) indicate a smaller iron particle size for the iron particles compared to the FeNPs on expanded graphite. It is logical to assume that the same trend is valid for vulcan carbon, which indicates that smaller particles yield longer fibers on vulcan carbon.

The S(T)EM images have not revealed that an apparent difference in crystallinity has affected the structure of the N-CNFs. However, this may be misleading as not all features of the structure are visible and detectable through a arbitrary selected area of a S(T)EM grid.

EDX

The EDX scans confirm that the black particles within the N-CNFs are either entrapped iron particles or FeNPs (Figures 5.28 and 5.30). Figure 5.28 also reveals a droplet shape of the particle, which is a shape associated with the top growth model.

One of the biggest problem with the EDX measurements was to get sufficient counts per second (cps). Normally the cps should be in the range of about 1600, but only values between 300 and 600 were achieved. This affects the intensity of the registered elements as noise signals from the surrounding objects are registered as well. Figure 5.29b illustrates a fishbone fiber that contains both iron and nitrogen according to the EDX scan. The iron is believed to be present within the fiber as atomic iron, as the signals are too strong to be noise from the surroundings. This could be a contributing effect towards enhanced ORR activity, but it should be detected for other samples too before concluding with something.

6.8   BET

The BET results (Table 5.6) indicates, 200Vu has both the highest surface area and cumulative volume of pores, followed by VuM, ExGM and 200ExG in terms of surface area of pores. Both the total surface area and the cumulative volume of pores include the surface area of the support and the synthesized fibers.

Compared to VuM24h, 200Vu24h has a significant lower yield ($5.60 \, \text{g/g}_\text{cat}$ and $7.25 \, \text{g/g}_\text{cat}$), which indicates that 200Vu24h possesses a much higher fiber surface area than VuM. The higher surface area for ExGM24h compared to 200ExG24h is attributed to the significant higher yield.

6.9   Electrochemical measurements

The highest activity was measured for 200Vu24h followed by VuM24h. Both samples consist of mostly bamboo structures attached to the support, but the fibers of 200Vu24h are in general smaller both in diameter and length. The shape of the two scans are quite equal. However, 200Vu24h has a steeper gradient between $0.75 \, \text{V}$ and $0.4 \, \text{V}$, which is a desirable feature.

In the terms of the difference in activity, this is mainly attributed to the structure of the N-CNFs. Despite the difficulties to observe differences between the samples through the S(T)EM images, the other characterization results indicate a difference. The surface area and cumulative volume of the pores is higher, despite the low yield for 200Vu24h. This indicates that 200Vu24h possesses more active sites compared to VuM24h. Although it is still unclear which role the surface area of N-CNFs play with respect to activity, these results indicate a beneficial effect of a high surface area and an importance of structure. Considering the iron source, the XRD scans from expanded graphite indicated a difference for the particles both in regards of crystallinity and a size prior to the synthesis. Combined with the activity measurements, this indicate that particles in the range of $25 \, \text{nm}$ with low crystallinity yield more desirable N-CNFs.

The scans of 200ExG24h and ExGM24h resemble each other in shape, and according to Figure 5.31 a difference can be seen in activity. However, this difference is not sufficient in order to determine whether they are distinguishable in activity or not, as it could be due to experimental factors. From the significant higher yield and higher surface area, ExGM24h should display a higher activity. From the characterization results, the nitrogen and oxygen content, the structure of the N-CNFs, and the yield differ too. Nevertheless, the nitrogen content is too low in order to display a high activity. Thus the activity is equal to 200ExG24h which has a significant lower yield and surface area. As the structure of the N-CNFs is linked to the nitrogen content, it is concluded that MWCNTs do not display high

activity towards the ORR.

The lack of support and the predominant presence of larger N-CNFs explains the significant lower activity of 200Fe24h compared to all other samples. Interestingly, 200Fe24h has both the highest oxygen content and the second highest nitrogen content of all samples, which would suggest a higher activity for the sample. This suggests that the non-catalytic graphite layers on the outside of the thickened N-CNFs are not as active as the potential core structure with most of the incorporated nitrogen.

The amount of H_2O_2 produced varies with the potential as seen by Figure 5.32. Ideally, the H_2O_2 should be compared at high potential where the reaction kinetics govern the activity. However, there are difficulties with measuring the produced H_2O_2, resulting in measurements from only $0.8\,V$. At low overpotentials, the activity is both governed by kinetics and diffusion, and gradually becoming diffusion controlled at higher overpotentials. In general, all samples have a high H_2O_2 production. Interestingly, both vulcan samples have similar nitrogen content, iron loading N-CNF structure and activity, but significant different H_2O_2 production. This indicates that the samples are not as similar as the observation suggest. Thus the difference in yield reflects a different composition for the N-CNF structures, which in turns affect the H_2O_2 production.

6.10   Further work

There are many parameters that are yet to be understood regarding the synthesis of N-CNFs, both with and without the use of FeNPs, and there are thus many more aspects that can be researched.

The gas flows used in the N-CNF synthesis were optimized for the growth of N-CNFs with iron nitrate, and it has been reported that strong bonding between nitrogen and iron may block the growth of N-CNFs. Thus, a study with different flow rates of NH_3 could be conducted in order to optimize the flow for the 200Vu24h catalyst. This may increase the activity if the yield is increased. For iron nitrate, the most active catalyst was grown at $650\,°C$, which is a growth temperature that also should be tried for 200Vu.

The origin of this thesis was to produce larger FeNPs than those produced by iron nitrate. As the results show, this was presumably achieved. Although, an interesting research would be to examine the possibility to produce larger FeNPs particle, and study their effect on both the produced N-CNFs and their activity. A possibility could be to prolong the synthesis time for RTFe and thus let the FeNPs complete the ongoing agglomeration process.

CHAPTER 7

CONCLUSION

Non-uniform N-CNFs were synthesized at 750 °C from uniform and homogeneous iron nanoparticles (FeNPs) on both expanded graphite and vulcan carbon. XRD measurements revealed that the FeNPs agglomerate during the reduction, resulting in a non-uniform starting system prior to synthesis start. Compared to samples impregnated with iron nitrate, the sample with FeNP deposited on vulcan carbon (200Vu24h) exhibited both the highest activity and onset potential towards the oxygen reduction reaction (ORR). This is attributed to the relative short N-CNFs with bamboo structure and high surface area. However, the sample produced high amounts of H_2O_2, making it less attractive as a potential catalyst for a transportable fuel cell.

The determining factors regarding activity for this particular system are yet to be understood. The results indicate that the N-CNFs need to be grown on a support, and contain a certain amount of nitrogen in order to display activity towards the ORR reaction. Nevertheless, comparing the XPS results with the electrochemical measurements for the two active samples, no correlation between neither the amount of nitrogen nor amount of quaternary-N and pyridinic-N and the activity was found. This suggests that a nitrogen content above a certain level and its composition might have a smaller effect on activity than perhaps both the structure and surface area of the N-CNFs.

BIBLIOGRAPHY

[1] Michael Bron. Non-Noble Metal Fuel Cell Catalysts. chapter Electrocatalysts for Acid Proton Exchange Membrane PEM Fuel Cells – an Overview, pages 1–28. Wiley-VCH Verlag GmbH & Co. KGaA, 2014.

[2] D. Yu, E. Nagelli, F. Du, and L. Dai. Metal-free carbon nanomaterials become more active than metal catalysts and last longer. *Journal of Physical Chemistry Letters*, 1(14):2165–2173, 2010.

[3] C.a Domínguez, F.J.a Pérez-Alonso, M.b Abdel Salam, S.A.b Al-Thabaiti, A.Y.b Obaid, A.A.b Alshehri, J.L.a Gómez de la Fuente, J.L.G.a Fierro, and S.a Rojas. On the relationship between N content, textural properties and catalytic performance for the oxygen reduction reaction of N/CNT. *Applied Catalysis B: Environmental*, 162:420–429, 2015.

[4] J.-P. Tessonnier and D.S. Su. Recent progress on the growth mechanism of carbon nanotubes: A review. *ChemSusChem*, 4(7):824–847, 2011.

[5] FREECATS. R &D activities, Decembre 2014. URL http://www.freecats.eu/empty_13.html.

[6] Expert Group on Future Transport Fuels. Future Transport Fuels – Report of the European Expert Group on Future Transport Fuels. Technical report, Expert Group on Future Transport Fuels, 2011. URL http://ec.europa.eu/transport/themes/urban/cts/doc/2011-01-25-future-transport-fuels-report.pdf.

[7] European Commission. Communication from the commission to the european parliament, the council, the european economic and social committee and the committee of the regions – a roadmap for moving to a competitive low carbon economy in 2050. Technical report, European Commission, 2011. URL http://eur-lex.europa.eu/resource.html?uri=cellar:5db26ecc-ba4e-4de2-ae08-dba649109d18.0002.03/DOC_1&format=PDF.

[8] S. Litster and G. McLean. PEM fuel cell electrodes. *Journal of Power Sources*, 130(1–2):61 – 76, 2004.

[9] R.K. Shah. Introduction to Fuel Cells. In Suddhasatwa Basu, editor, *Recent Trends in Fuel Cell Science and Technology*, pages 1–9. Springer New York, 2007.

[10] Paola Costamagna and Supramaniam Srinivasan. Quantum jumps in the PEMFC science and technology from the 1960s to the year 2000: Part i. Fundamental scientific aspects. *Journal of Power Sources*, 102(1–2):242 – 252, 2001.

[11] Mei Zhang and Liming Dai. Carbon nanomaterials as metal-free catalysts in next generation fuel cells. *Nano Energy*, 1(4):514 – 517, 2012.

[12] I. Chorkendorff and J. W. Niemantsverdriet. *Heterogeneous Catalysis in Practice: Hydrogen*, pages 301–348. Wiley-VCH Verlag GmbH & Co. KGaA, 2005.

[13] S. Liu, C. Deng, L. Yao, H. Zhong, and H. Zhang. The key role of metal dopants in nitrogen-doped carbon xerogel for oxygen reduction reaction. *Journal of Power Sources*, 269:225–235, 2014.

[14] L. Qu, Y. Liu, J. B. Baek, and L. Dai. Nitrogen-doped graphene as efficient metal-free electrocatalyst for oxygen reduction in fuel cells. *ACS Nano*, 4(3): 1321–1326, 2010.

[15] Ermete Antolini. Carbon supports for low-temperature fuel cell catalysts. *Applied Catalysis B: Environmental*, 88(1–2):1 – 24, 2009.

[16] E. Antolini. Formation, microstructural characteristics and stability of carbon supported platinum catalysts for low temperature fuel cells. *Journal of Materials Science*, 38(14):2995–3005, 2003.

[17] Stephen Maldonado and Keith J. Stevenson. Influence of Nitrogen Doping on Oxygen Reduction Electrocatalysis at Carbon Nanofiber Electrodes. *The Journal of Physical Chemistry B*, 109(10):4707–4716, 2005.

[18] YoongA. Kim, Takuya Hayashi, Morinobu Endo, and MildredS. Dresselhaus. Carbon nanofibers. In Robert Vajtai, editor, *Springer Handbook of Nanomaterials*, pages 233–262. Springer Berlin Heidelberg, 2013.

[19] Ignacio Martin-Gullon, José Vera, Juan A. Conesa, José L. González, and César Merino. Differences between carbon nanofibers produced using Fe and Ni catalysts in a floating catalyst reactor. *Carbon*, 44(8):1572 – 1580, 2006.

[20] Peter E. Nolan, David C. Lynch, and Andrew Hall Cutler. Carbon Deposition and Hydrocarbon Formation on Group VIII Metal Catalysts. *The Journal of Physical Chemistry B*, 102(21):4165–4175, 1998.

[21] Peter E. Nolan, Michael J. Schabel, David C. Lynch, and Andrew Hall Cutler. Hydrogen control of carbon deposit morphology. *Carbon*, 33(1):79 – 85, 1995.

[22] Yoong-Ahm Kim, Takuya Hayashi, Satoru Naokawa, Takashi Yanagisawa, and Morinobu Endo. Comparative study of herringbone and stacked-cup carbon nanofibers. *Carbon*, 43(14):3005 – 3008, 2005.

[23] Yahachi Saito. Nanoparticles and filled nanocapsules. *Carbon*, 33(7):979 – 988, 1995.

[24] Nelly M. Rodriguez, Alan Chambers, and R. Terry K. Baker. Catalytic Engineering of Carbon Nanostructures. *Langmuir*, 11(10):3862–3866, 1995.

[25] Alessandro Chiolerio, Angelica Chiodoni, Paolo Allia, and Paola Martino. Magnetite and Other Fe-Oxide Nanoparticles. In Bharat Bhushan, Dan Luo, Scott R. Schricker, Wolfgang Sigmund, and Stefan Zauscher, editors, *Handbook of Nanomaterials Properties*, pages 213–246. Springer Berlin Heidelberg, 2014.

[26] Manuel Bañobre-López, Y. Piñeiro, M.Arturo López-Quintela, and José Rivas. Magnetic Nanoparticles for Biomedical Applications. In Bharat Bhushan, Dan Luo, Scott R. Schricker, Wolfgang Sigmund, and Stefan Zauscher, editors, *Handbook of Nanomaterials Properties*, pages 457–493. Springer Berlin Heidelberg, 2014.

[27] M. Faraji, Y. Yamini, and M. Rezaee. Magnetic nanoparticles: Synthesis, stabilization, functionalization, characterization, and applications. *Journal of the Iranian Chemical Society*, 7(1):1–37, 2010.

[28] Eric Marceau, Xavier Carrier, and Michel Che. *Impregnation and Drying*, pages 59–82. Wiley-VCH Verlag GmbH & Co. KGaA, 2009.

[29] Krzysztof Koziol, BojanObrad Boskovic, and Noorhana Yahya. Synthesis of Carbon Nanostructures by CVD Method. In *Carbon and Oxide Nanostructures*, volume 5 of *Advanced Structured Materials*, pages 23–49. Springer Berlin Heidelberg, 2011.

[30] Xuezhi Duan, Jian Ji, Gang Qian, Xinggui Zhou, and De Chen. Recent advances in synthesis of reshaped fe and ni particles at the tips of carbon nanofibers and their catalytic applications. *Catalysis Today*, 249(0):2 – 11, 2015. Carbon in Catalysis.

[31] Francisco Rodríguez-reinoso. The role of carbon materials in heterogeneous catalysis. *Carbon*, 36(3):159 – 175, 1998.

[32] Zhixin Yu, De Chen, Bård Tøtdal, and Anders Holmen. Effect of Support and Reactant on the Yield and Structure of Carbon Growth by Chemical Vapor Deposition. *The Journal of Physical Chemistry B*, 109(13):6096–6102, 2005.

[33] Xuezhi Duan, Gang Qian, Jinghong Zhou, Xinggui Zhou, De Chen, and Weikang Yuan. Flat interface mediated synthesis of platelet carbon nanofibers on fe nanoparticles. *Catalysis Today*, 186(1):48 – 53, 2012. Carbon for Catalysis: CarboCat-IV Symposium.

[34] Z. J. Lu, S. J. Bao, Y. T. Gou, C. J. Cai, C. C. Ji, M. W. Xu, J. Song, and R. Wang. Nitrogen-doped reduced-graphene oxide as an efficient metal-free electrocatalyst for oxygen reduction in fuel cells. *RSC Advances*, 3(12): 3990–3995, 2013.

[35] S. Bai, S. Chen, X. Shen, G. Zhu, and G. Wang. Nanocomposites of hematite (α-Fe$_2$O$_3$) nanospindles with crumpled reduced graphene oxide nanosheets as high-performance anode material for lithium-ion batteries. *RSC Advances*, 2 (29):10977–10984, 2012.

[36] S.B. Sinnott, R. Andrews, D. Qian, A.M. Rao, Z. Mao, E.C. Dickey, and F. Derbyshire. Model of carbon nanotube growth through chemical vapor deposition. *Chemical Physics Letters*, 315(1–2):25–30, 1999.

[37] Paul E. Anderson and Nelly M. Rodríguez. Influence of the Support on the Structural Characteristics of Carbon Nanofibers Produced from the Metal-Catalyzed Decomposition of Ethylene. *Chemistry of Materials*, 12(3):823–830, 2000.

[38] P. Moodley, J. Loos, J.W. Niemantsverdriet, and P.C. Thüne. Is there a correlation between catalyst particle size and CNT diameter? *Carbon*, 47(8): 2002 – 2013, 2009.

[39] Takashi Inoue, Itaru Gunjishima, and Atsuto Okamoto. Synthesis of diameter-controlled carbon nanotubes using centrifugally classified nanoparticle catalysts. *Carbon*, 45(11):2164 – 2170, 2007.

[40] Gregg S.B. McKee, Christian P. Deck, and Kenneth S. Vecchio. Dimensional control of multi-walled carbon nanotubes in floating-catalyst CVD synthesis. *Carbon*, 47(8):2085 – 2094, 2009.

[41] Takashi Ikeda, Mauro Boero, Sheng-Feng Huang, Kiyoyuki Terakura, Masaharu Oshima, and Jun-ichi Ozaki. Carbon alloy catalysts: Active sites for oxygen reduction reaction. *The Journal of Physical Chemistry C*, 112(38): 14706–14709, 2008.

[42] Nalini P. Subramanian, Xuguang Li, Vijayadurda Nallathambi, Swaminatha P. Kumaraguru, Hector Colon-Mercado, Gang Wu, Jong-Won Lee, and Branko N. Popov. Nitrogen-modified carbon-based catalysts for oxygen reduction reaction in polymer electrolyte membrane fuel cells. *Journal of Power Sources*, 188(1):38 – 44, 2009.

[43] Zhiqiang Luo, Sanhua Lim, Zhiqun Tian, Jingzhi Shang, Linfei Lai, Brian MacDonald, Chao Fu, Zexiang Shen, Ting Yu, and Jianyi Lin. Pyridinic N-doped graphene: synthesis, electronic structure, and electrocatalytic property. *J. Mater. Chem.*, 21:8038–8044, 2011.

[44] Marthe E. M. Buan, Navaneethan Muthuswamy, John C. Walmsley, De Chen, and Magnus Rønning. The Role of Transition Metals on the Oxygen Reduction Activity of Nitrogen-doped Carbon Nanofibers. Manuscript in preparation.

[45] Gang Wu, Christina M. Johnston, Nathan H. Mack, Kateryna Artyushkova, Magali Ferrandon, Mark Nelson, Juan S. Lezama-Pacheco, Steven D. Conradson, Karren L. More, Deborah J. Myers, and Piotr Zelenay. Synthesis-structure-performance correlation for polyaniline-Me-c non-precious metal cathode catalysts for oxygen reduction in fuel cells. *J. Mater. Chem.*, 21: 11392–11405, 2011.

[46] Elizabeth J. Biddinger and Umit S. Ozkan. Role of graphitic edge plane exposure in carbon nanostructures for oxygen reduction reaction. *The Journal of Physical Chemistry C*, 114(36):15306–15314, 2010.

[47] Structure, composition, and chemical reactivity of carbon nanotubes by selective nitrogen doping. *Carbon*, 44(8):1429 – 1437, 2006.

[48] S.J. Pennycook, A.R. Lupini, M. Varela, A. Borisevich, Y. Peng, M.P. Oxley, K. Van Benthem, and M.F. Chisholm. Scanning Transmission Electron Microscopy for Nanostructure characterization. In Weilie Zhou and ZhongLin Wang, editors, *Scanning Microscopy for Nanotechnology*, pages 152–191. Springer New York, 2007.

[49] NTNU NanoLab. NTNU NanoLab, S(T)EM Introduction Course. Lecture given at NTNU NanoLab, September 2014.

[50] N.R. Lugg, G. Kothleitner, N. Shibata, and Y. Ikuhara. On the quantitativeness of {EDS} {STEM}. *Ultramicroscopy*, 151(0):150 – 159, 2015. Special Issue: 80th Birthday of Harald Rose; {PICO} 2015 – Third Conference on Frontiers of Aberration Corrected Electron Microscopy.

[51] Oxford Instruments. Eds in the TEM explained. URL http://www.oxford-instruments.com/OxfordInstruments/media/nanoanalysis/brochures%20and%20thumbs/TEM-Explained.pdf.

[52] DavidB. Williams and C.Barry Carter. X-ray Spectrometry. In *Transmission Electron Microscopy*, pages 581–603. Springer US, 2009.

[53] Magnus Rønning. Catalyst chacterization. Lecture given at NTNU in TKP4515 Catalysis and Petrochemisty, Specialization Course, September 2014.

[54] Powder X-ray Diffraction, December 2014. URL `http://chemwiki.ucdavis.edu/Analytical_Chemistry/Instrumental_Analysis/Diffraction/Powder_X-ray_Diffraction`.

[55] J. F. Le Page, D. Avnir, E. Taglauer, M. Guisnet, G. Moretti, M. Che, F. Bozon-Verduraz, M. Anpo, E. Roduner, and H. Knözinger. *Characterization of Solid Catalysts: Sections 3.1.4 – 3.2.2*, pages 582–689. Wiley-VCH Verlag GmbH, 2008.

[56] Wolfgang Grünert. *Auger Electron, X ray and UV Photoelectron Spectroscopies*, pages 537–583. Wiley-VCH Verlag GmbH & Co. KGaA, 2012.

[57] Casa Software Ltd. Basic Quantification of XPS Spectra, December 2008. URL `http://www.casaxps.com/help_manual/manual_updates/Basics_Quantification_of_XPS_Spectra.pdf`.

[58] I. Chorkendorff and J. W. Niemantsverdriet. *Solid Catalysts*, pages 167–214. Wiley-VCH Verlag GmbH & Co. KGaA, 2005.

[59] Gurvinder Singh, Puri Anil Kumar, Christopher Lundgren, Antonius T. J. van Helvoort, Roland Mathieu, Erik Wahlström, and Wilhelm R. Glomm. Tunability in crystallinity and magnetic properties of core–shell fe nanoparticles. *Particle Particle Systems Characterization*, 2014.

[60] Genxi Li and Peng Miao. Theoretical background of electrochemical analysis. In *Electrochemical Analysis of Proteins and Cells*, SpringerBriefs in Molecular Science, pages 5–18. Springer Berlin Heidelberg, 2013.

[61] Anne Helene Barsnes. Nitrogen-doped carbon nanofibers as metal-free catalyst in the oxygen reduction reaction, 2014.

[62] Paul H. Matter, Ling Zhang, and Umit S. Ozkan. The role of nanostructure in nitrogen-containing carbon catalysts for the oxygen reduction reaction. *Journal of Catalysis*, 239(1):83 – 96, 2006.

[63] P.H. Matter, E. Wang, M. Arias, E.J. Biddinger, and U.S. Ozkan. Oxygen reduction reaction catalysts prepared from acetonitrile pyrolysis over alumina-supported metal particles. *Journal of Physical Chemistry B*, 110(37):18374–18384, 2006.

[64] De Chen, Kjersti O. Christensen, Ester Ochoa-Fernández, Zhixin Yu, Bård Tøtdal, Nieves Latorre, Antonio Monzón, and Anders Holmen. Synthesis of carbon nanofibers: effects of Ni crystal size during methane decomposition. *Journal of Catalysis*, 229(1):82 – 96, 2005.

APPENDIX A

CALCULATIONS OF FE LOADING FROM TPO MEASUREMENTS

Under follows the calculation of the weight percent loading of FeNPs on support based on the TPO measurements done in Section 3.2. All results are given in Table A.1, but only the calculation for 200Vu is given as an example below. The belonging graphs are displayed in Appendix B.

The TPO measurements startet with an intial weight m_i of 11.1 mg of iron impregnated on expanded graphite. The final TPO results showed a weight perecent of 24.78 % of iron oxide, here assumed to be Fe_2O_3, with an equivalent weight of $m_{Fe_2O_3} = 11.1\,\text{mg} \times 0.2478 = 2.751\,\text{mg}$.

The mass and weight percent of iron was then calculated by assuming that only Fe_2O_3 is present.

$$m_{Fe} = \frac{2M_{Fe}}{2M_{Fe} + 3M_O} \times m_{Fe_2O_3}$$

$$= \frac{2 \times 55.845\,\text{g mol}^{-1}}{2 \times 55.845\,\text{g mol}^{-1} + 3 \times 15.999\,\text{g mol}^{-1}} \times 2.751\,\text{mg} = 1.924\,\text{mg}$$

$$w\%_{Fe} = \frac{m_{Fe}}{m_i} \times 100\,\% = \frac{2.751\,\text{mg}}{11.1\,\text{mg}} \times 100\,\% = 17.33\,\%$$

Table A.1: Calculated Fe loadings.

Sample name	Weight [mg]	Mass minimum [%]	Weight percent Fe [wt%]
200ExG	5.1	23.5	16.4
ExG	2.5	26.3	18.4
200Vu	11.1	24.8	17.3
VuM	11.6	24.9	17.4

Appendix B

TPO

B.1 Fe loading

Figures B.1 to B.4 show the results from the analysis for 200ExG, ExGM, 200Vu and VuM respectively. Both the weight changes in % and the DSC profile are plotted as a function of temperature, but note that the DSC curve is has no belonging axis, as only the trends are of interes. The calculation of the Fe loading is found in Appendix A.
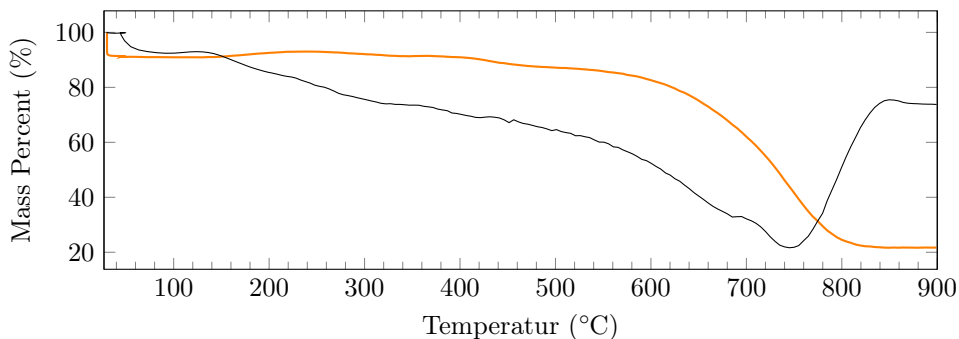
Figure B.1: TPO 200ExG: mass reduction profile —— and the corresponding DSC curve —— as a function of temperature.
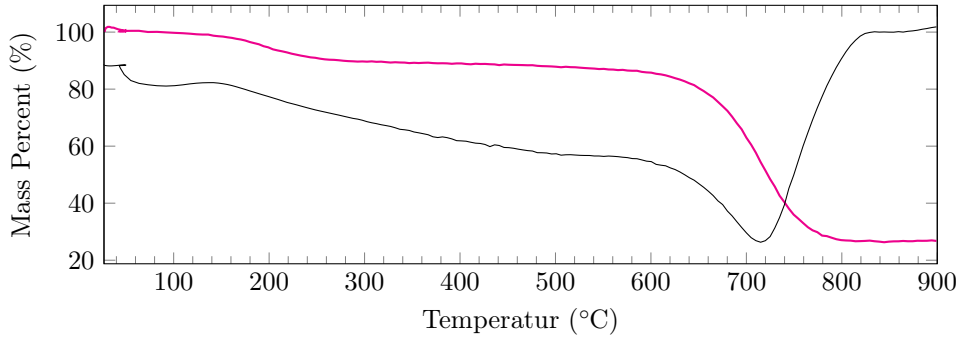
Figure B.2: TPO ExGM: mass reduction profile ▬▬ and the corresponding DSC curve ▬▬ as a function of temperature.
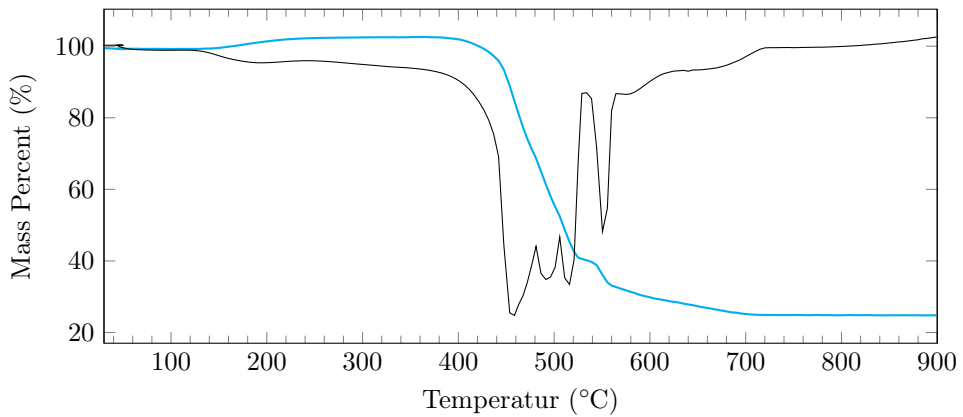
Figure B.3: 200Vu: mass reduction profile ▬▬ and the corresponding DSC ▬▬ as a function of temperature.
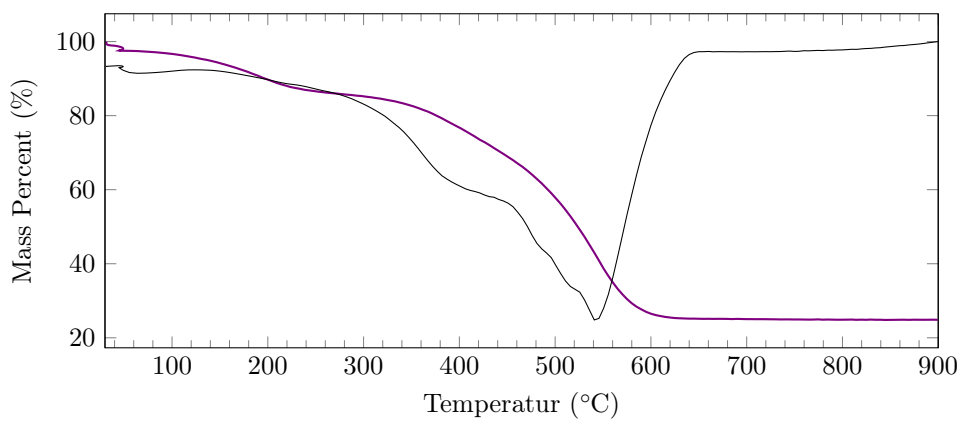
Figure B.4: VuM: mass reduction profile ―― and the corresponding DSC ――
as a function of temperature.

B.2   N-CNFs

Figures B.5, B.7, B.9 and B.11 illustrate the mass reduction profile for the samples 200ExG24h, ExGM24h, 200Vu24h and VuM24h as a function of temperature. The corresponding MS signals are illustrated in Figures B.6, B.8, B.10 and B.12 for 200ExG24h, ExGM24h, 200Vu24h and VuM24h respectively.

200ExG24h
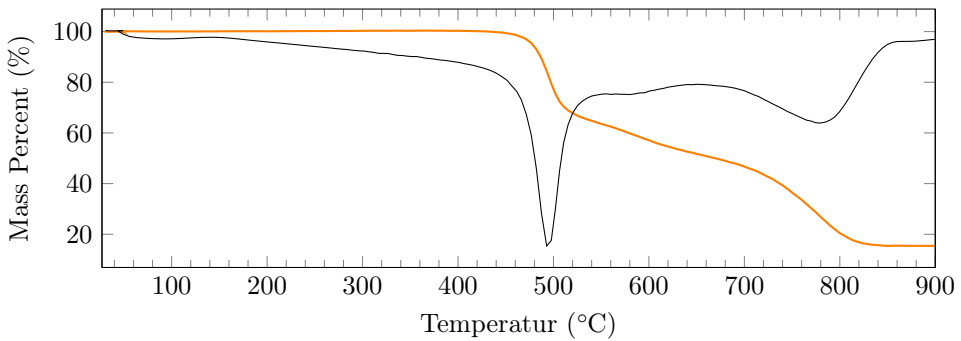
Figure B.5: 200ExG24h: mass reduction profile —— and the corresponding DSC —— as a function of temperature
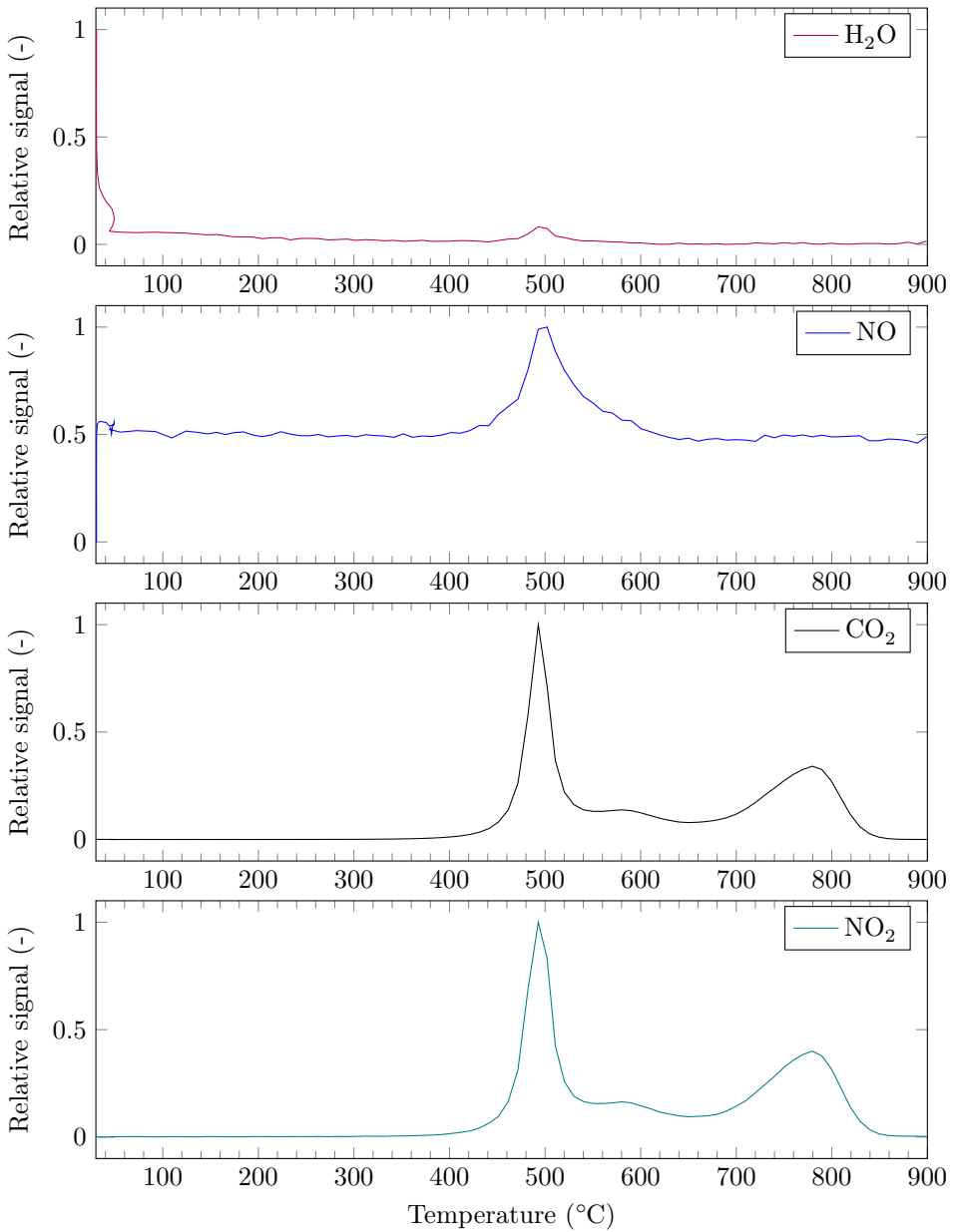
Figure B.6: TPO 200ExG24h: MS measurements from Figure B.5.

ExGM24h
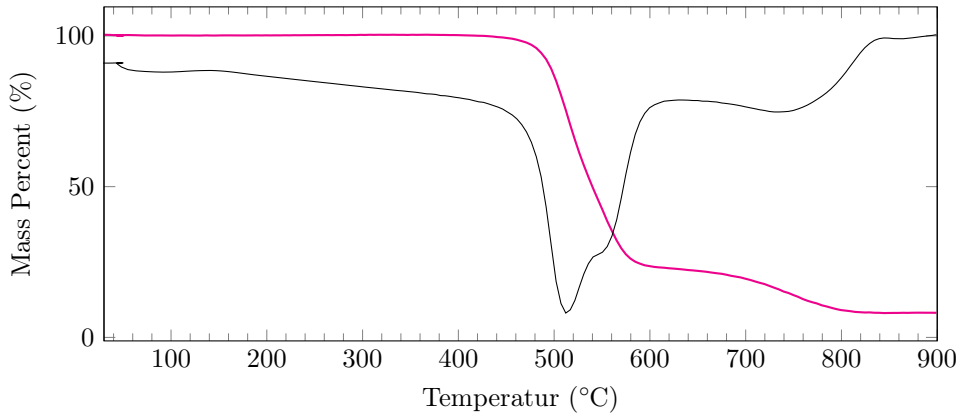
Figure B.7: ExGM24h: mass reduction profile ——— and the corresponding DSC ——— as a function of temperature.
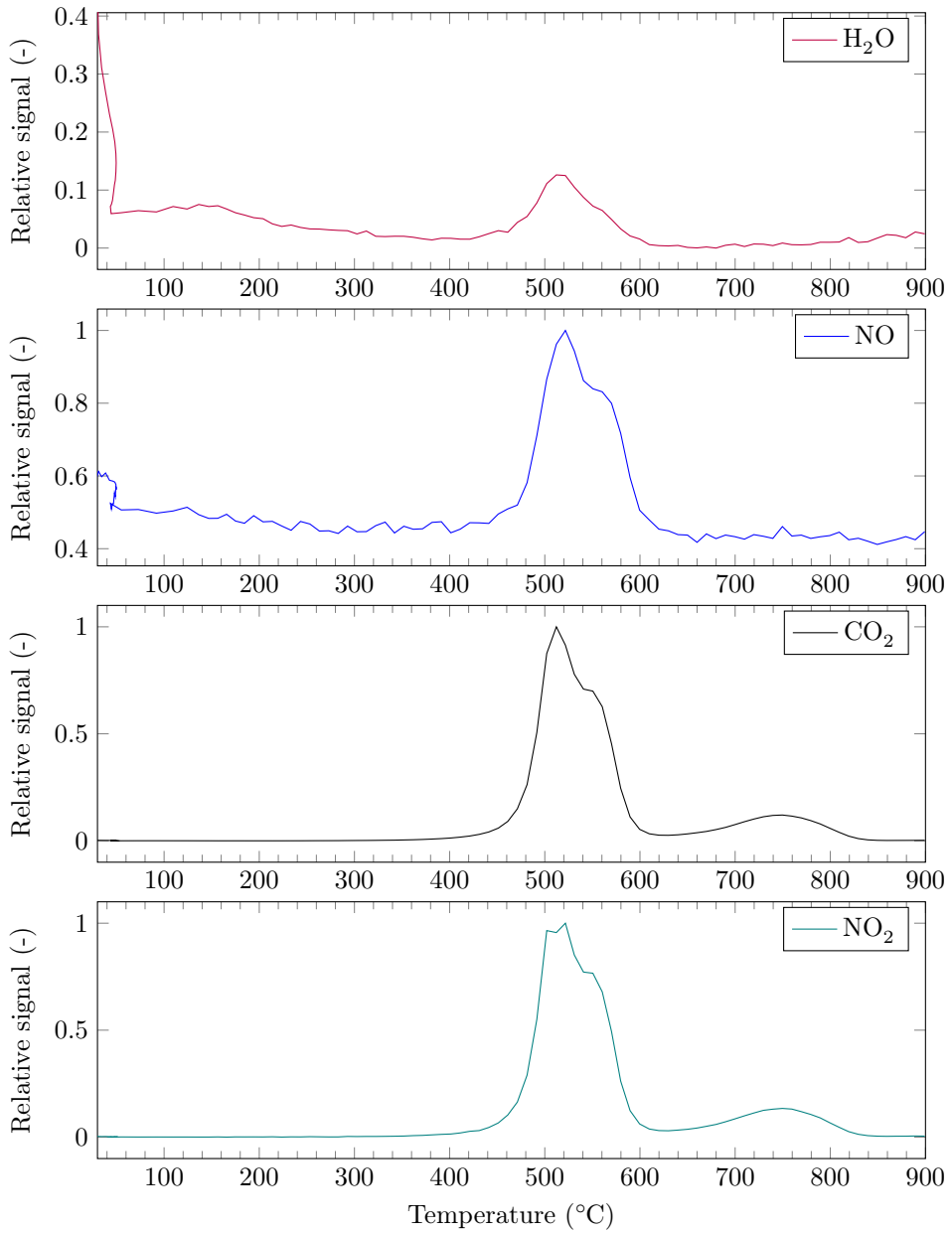
Figure B.8: TPO ExGM24h: MS measurements from Figure B.7.

B.3   200Vu24h
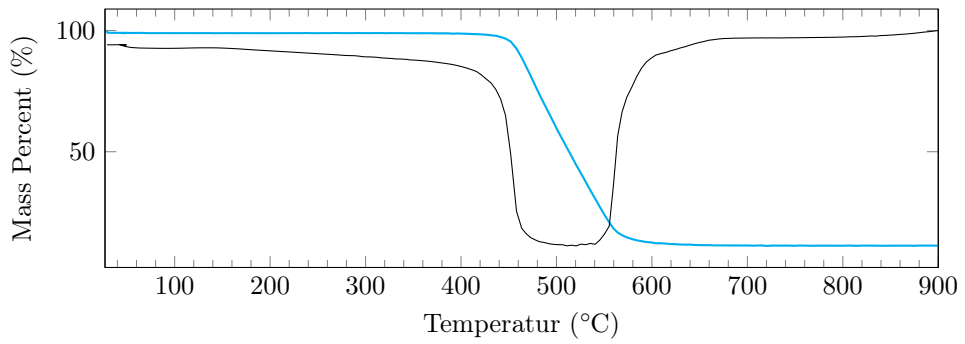
Figure B.9: 200Vu24h: mass reduction profile —— and the corresponding DSC
—— as a function of temperature
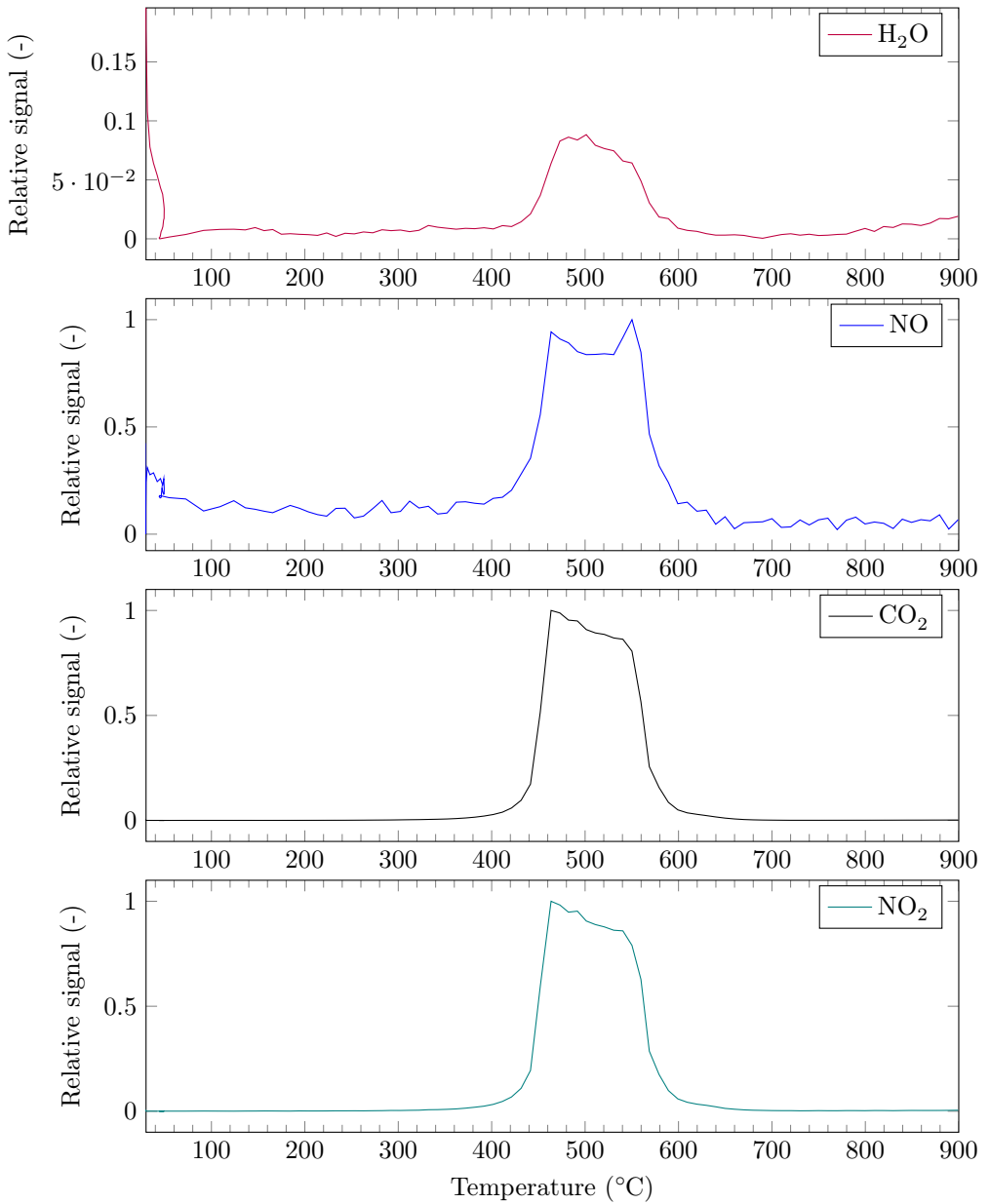
Figure B.10: TPO 200Vu24h: MS measurements from Figure B.9.

B.4   VuM24h
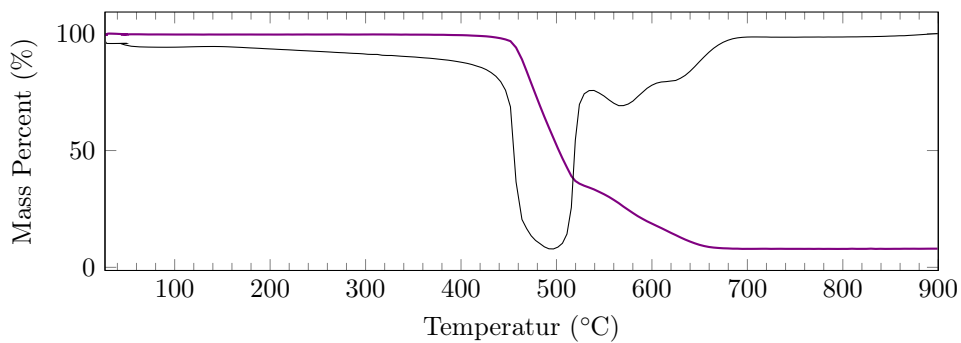
Figure B.11: VuM24h: mass reduction profile ▬▬ and the corresponding DSC
—— as a function of temperature
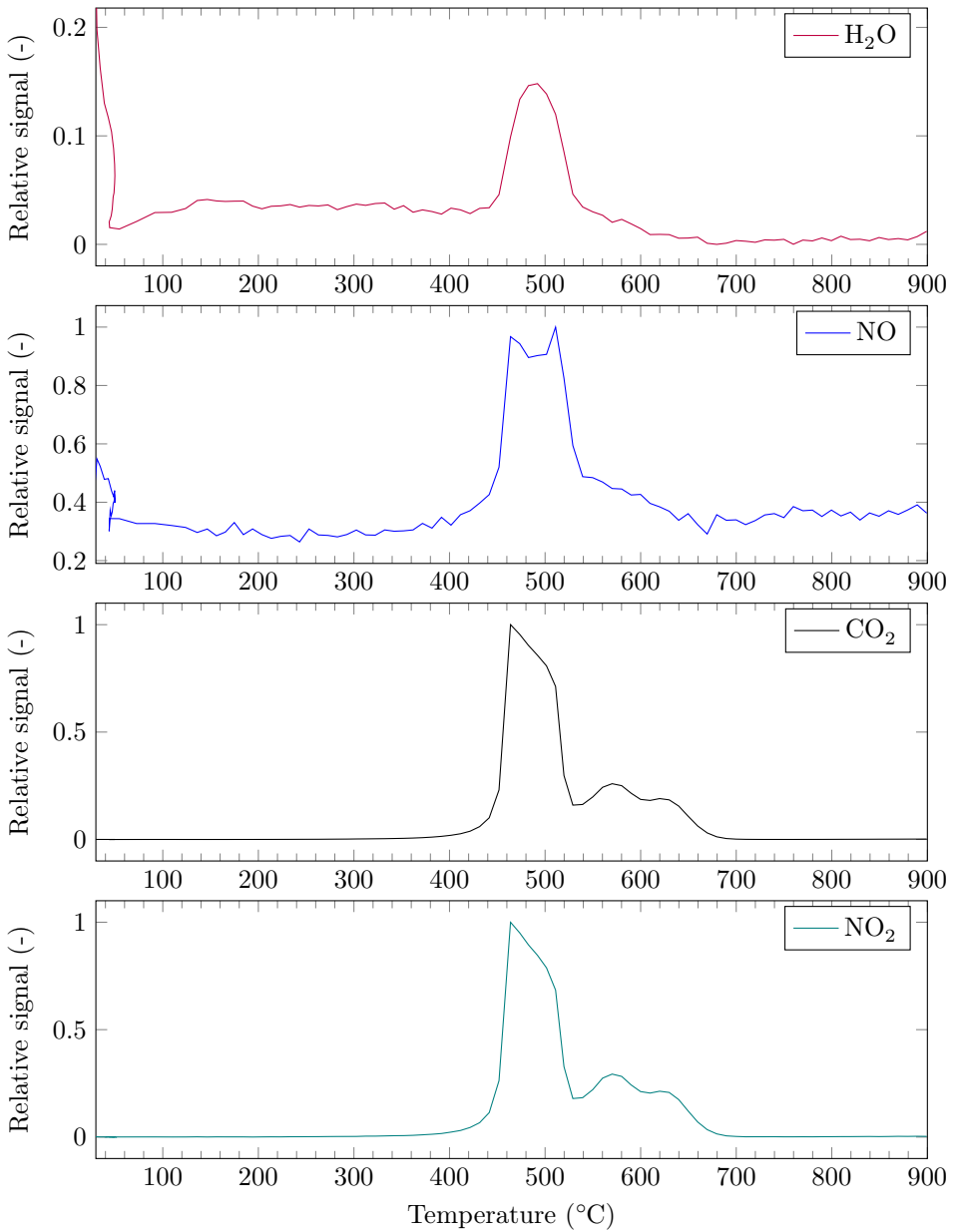
Figure B.12: TPO VuM24h: MS measurements from Figure B.11.

Appendix C

XRD

This Appendix provides XRD plots of the samples 200ExG and 200Vu reduced at 650 °C in Figure C.1 and dried FeNPs from the sample 200Fe in Figure C.2
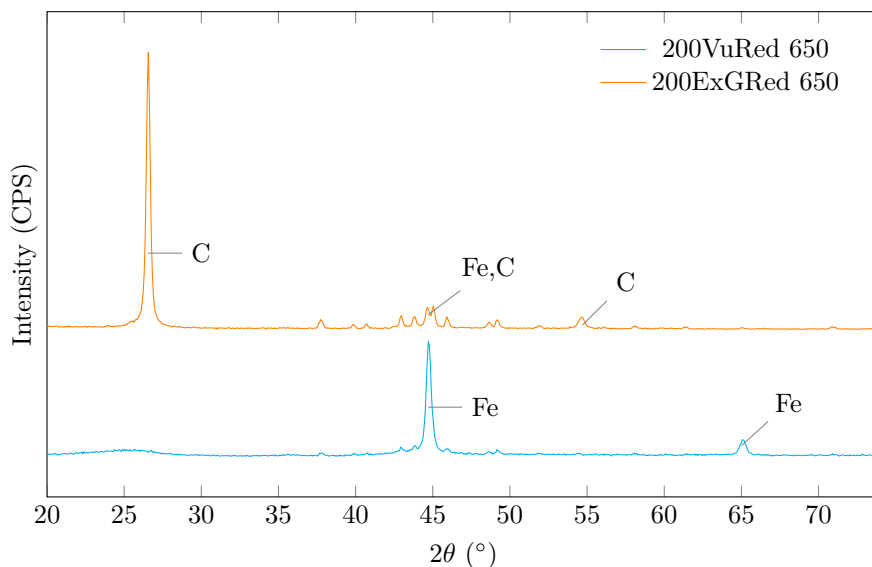
Figure C.1: XRD: 200ExG reduced at 650 °C ——— and 200Vu reduced at 650 °C ———. C represents carbon in the form of graphite, whereas Fe represents metallic iron. The peaks in the range 40° to 50° for 200ExGRed are mostly graphite, but also contain a combined Fe and C peak at about 44.5°.
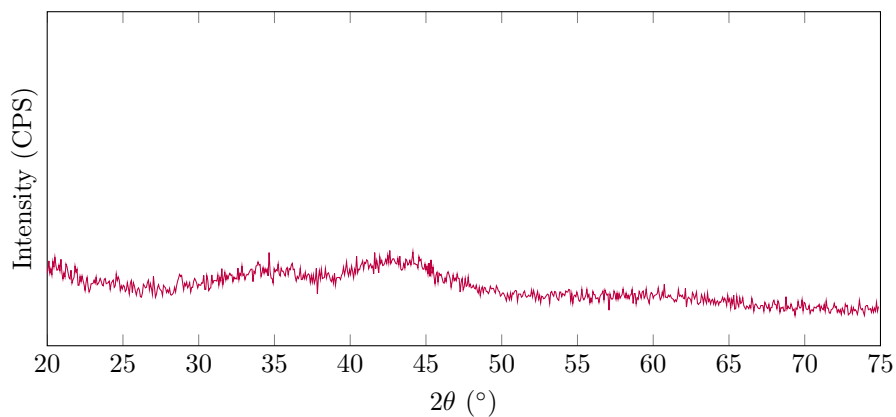
Figure C.2: XRD plot of dried FeNPs from the sample 200Fe.

Particle size distribution

This appendix illustrates the compromised particle size distribution given in Chapter 5 in full scale. The particle size distribution for 200ExGRed is split into two Figures, Figures D.2 and D.2 in order to produce readable diagrams.
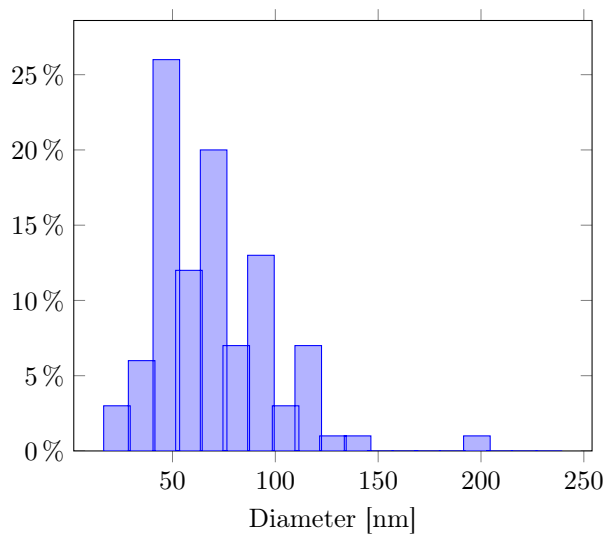
Figure D.1: 200ExGRed: Particle size distribution based on Figure 5.8a. The average diameter is 69.5±0.5 nm based on a count of 100 particles.
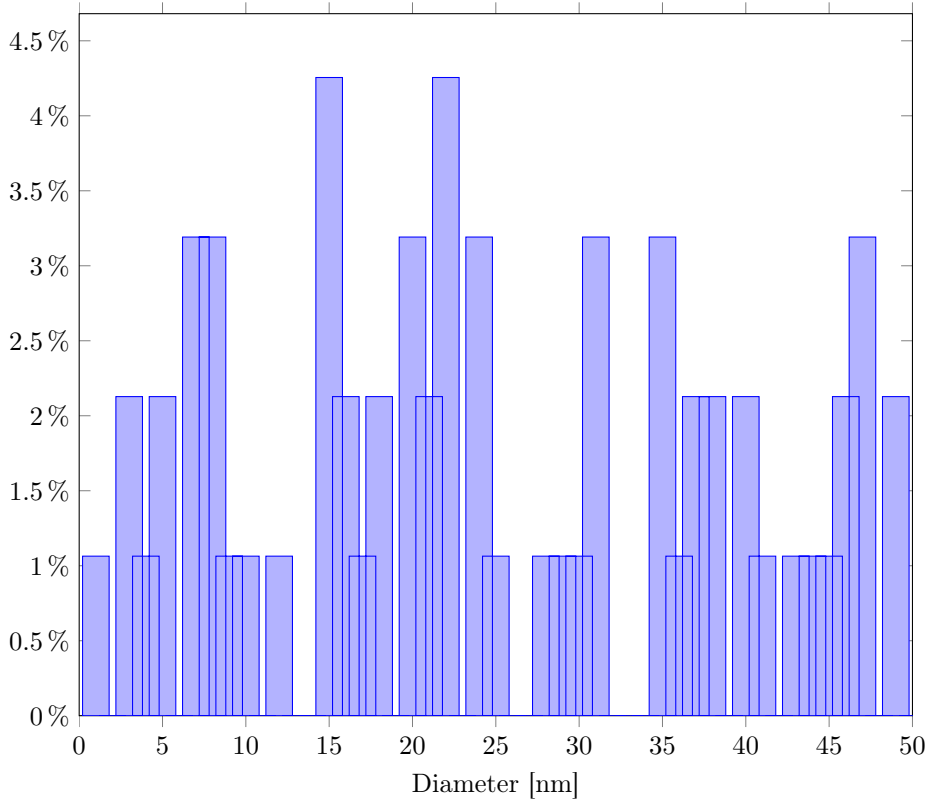
Figure D.2: 200ExGRed: Part 1 of the particle size distribution based on Figure 5.9. The average diameter is 39.5±0.5 nm based on a count of 94 particles.
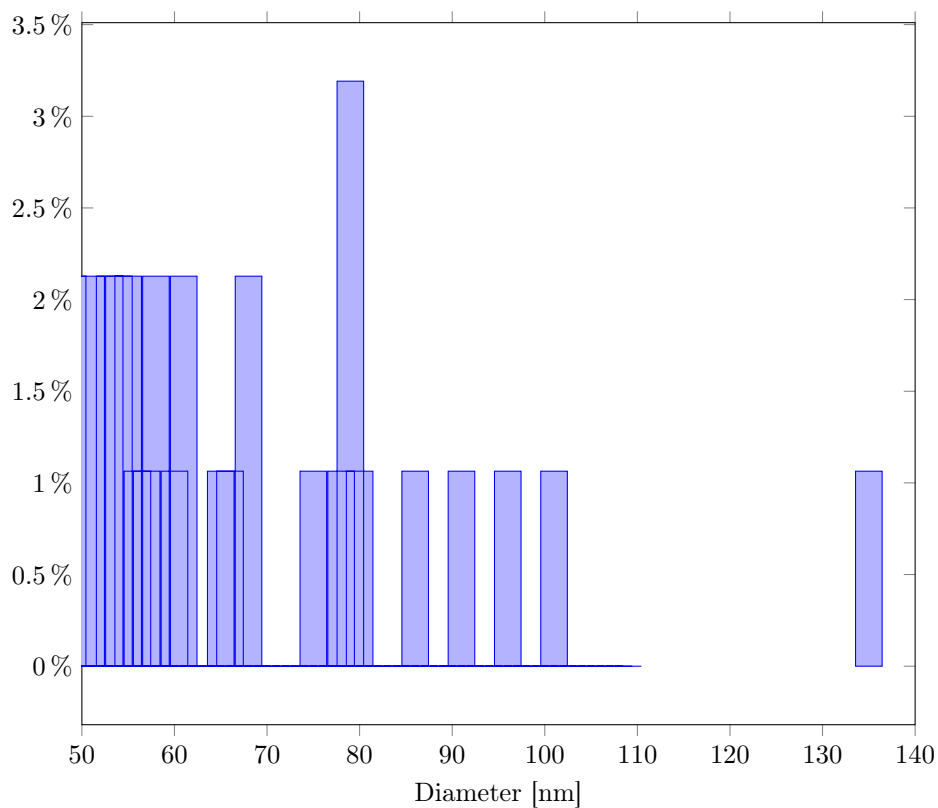
Figure D.3: 200ExGRed: Part 2 of the particle size distribution based on Figure 5.9. The average diameter is 39.5±0.5 nm based on a count of 94 particles.
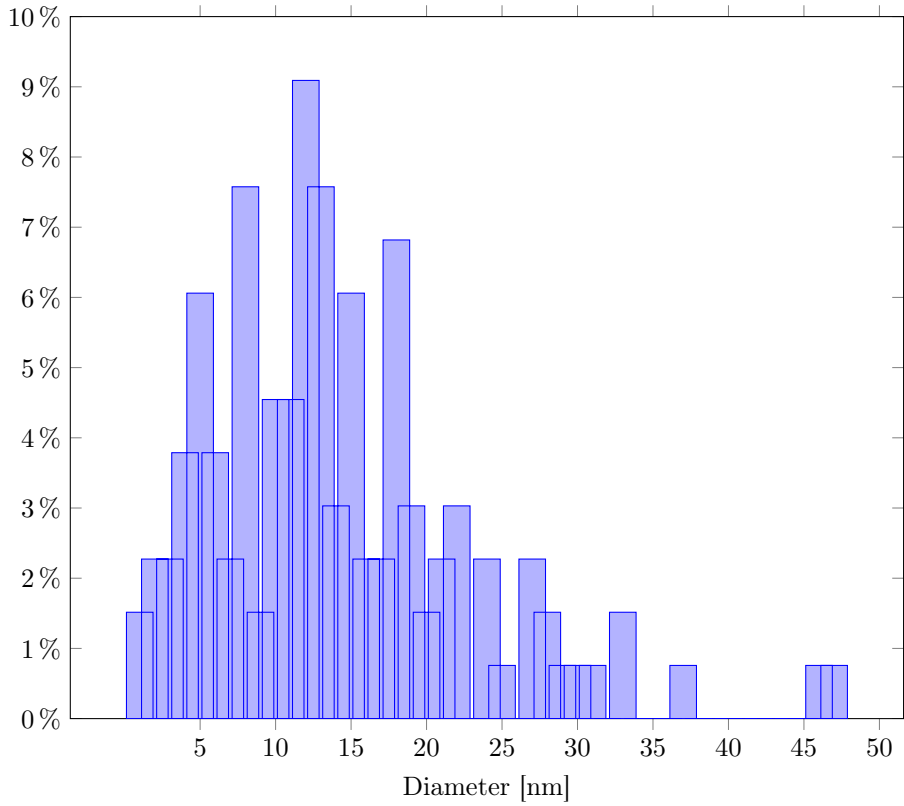
Figure D.4: ExGMRed: Particle size distribution based on Figure 5.10. The average diameter is 14.5±0.5 nm based on a count of 133 particles.

APPENDIX E

S(T)EM IMAGES

This Appendix provides additional S(T)EM pictures of some of the samples presented in the thesis.

Figure 5.3a illustrates a close up of the FeNPs produced by 260Fe. Appendix E.2 illustrates the reduced 200Vu at 750 °C.

Appendices E.3 to E.7 illustrate additional S(T)EM picture for the samples 200Fe24h, 200ExG24h, ExGM24h, 200Vu24h and VuM24h.

E.1   260Fe
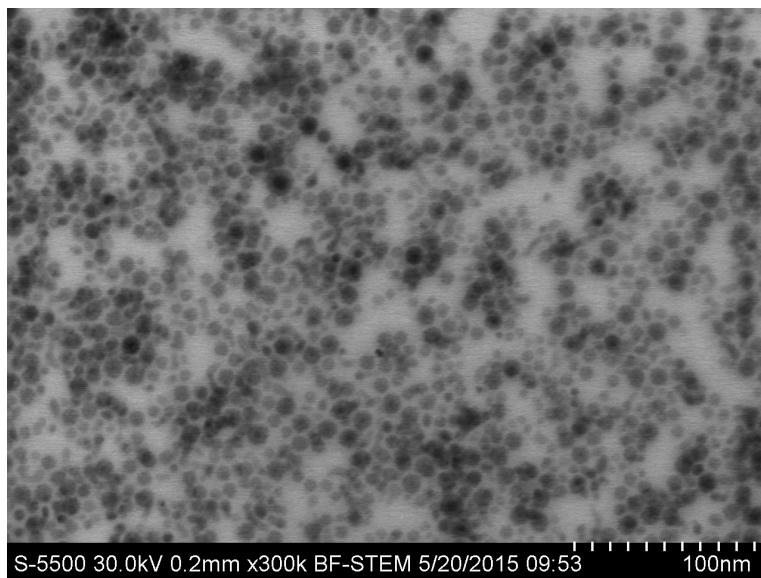
Figure E.1: S(T)EM 260Fe: A closeup of the FeNPs illlustrated in Figure 5.3a.

E.2 200Vu reduced

(a)   (b)
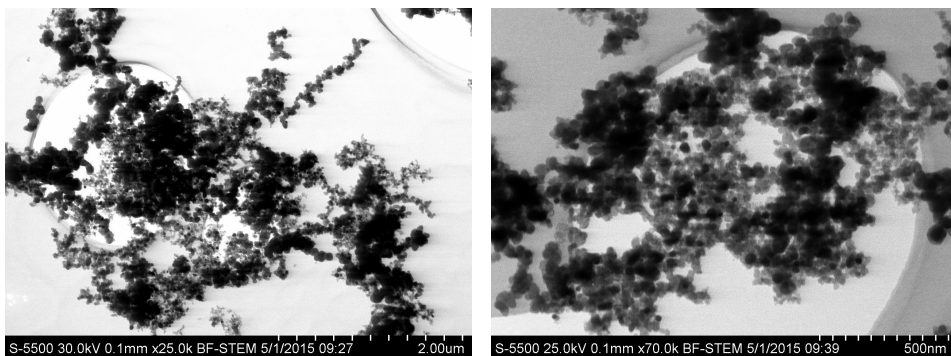
Figure E.2: S(T)EM 200VuRed: Support with FeNPs

E.3   200Fe24h

(a)   **(b)**
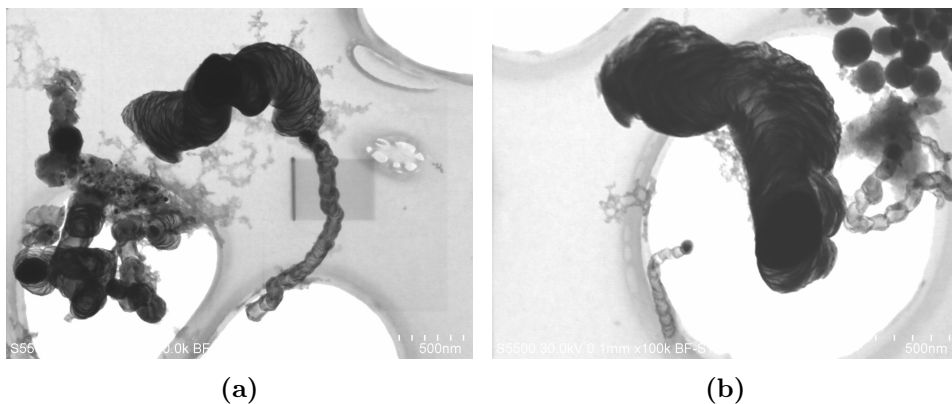
Figure E.3: S(T)EM 200Fe24h: (a) a overview of some thickened N-CNFs and one
with bamboo structure (b) a thickened N-CNFs, two with bamboo
structure and freestanding FeNPs.

(a)   **(b)**
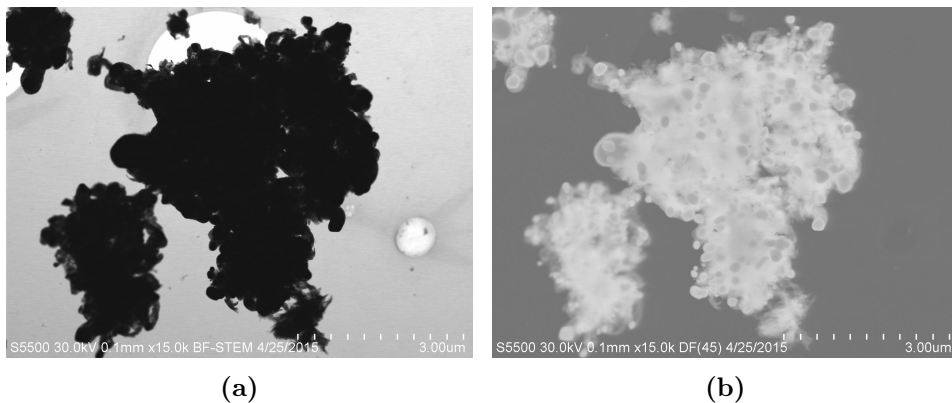
Figure E.4: S(T)EM 200Fe24h: N-CNF cluster in (a) BF mode (b) DF mode.
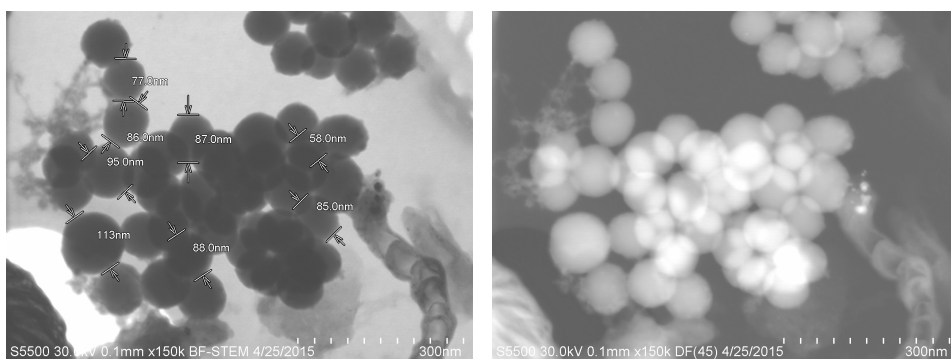
Figure E.5: S(T)EM 200Fe24h: Agglomerated FeNPs with an average diameter of about 86 nm in both dark field and bright field.

E.4 200ExG24h
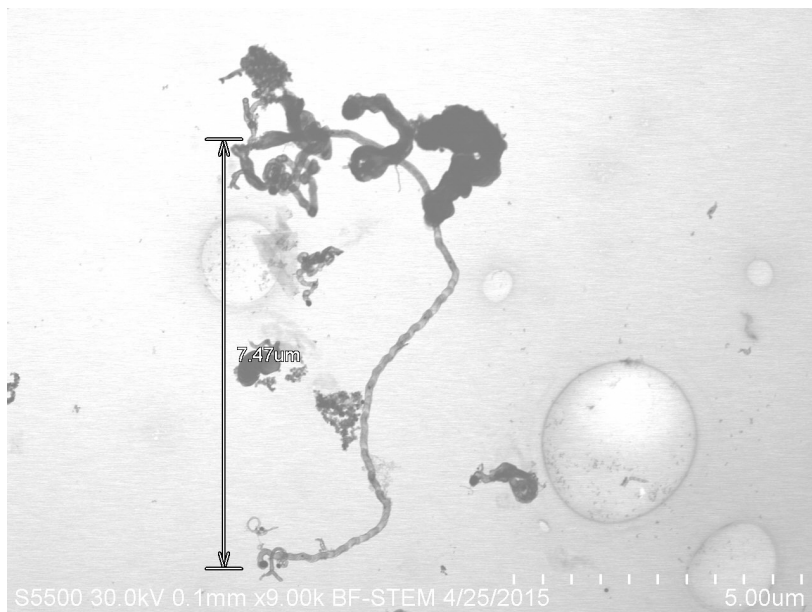
Figure E.6: S(T)EM 200ExG24h: A 7.47 µm long N-CNF with strucuture and some larger thickened N-CNFs in the upper part.
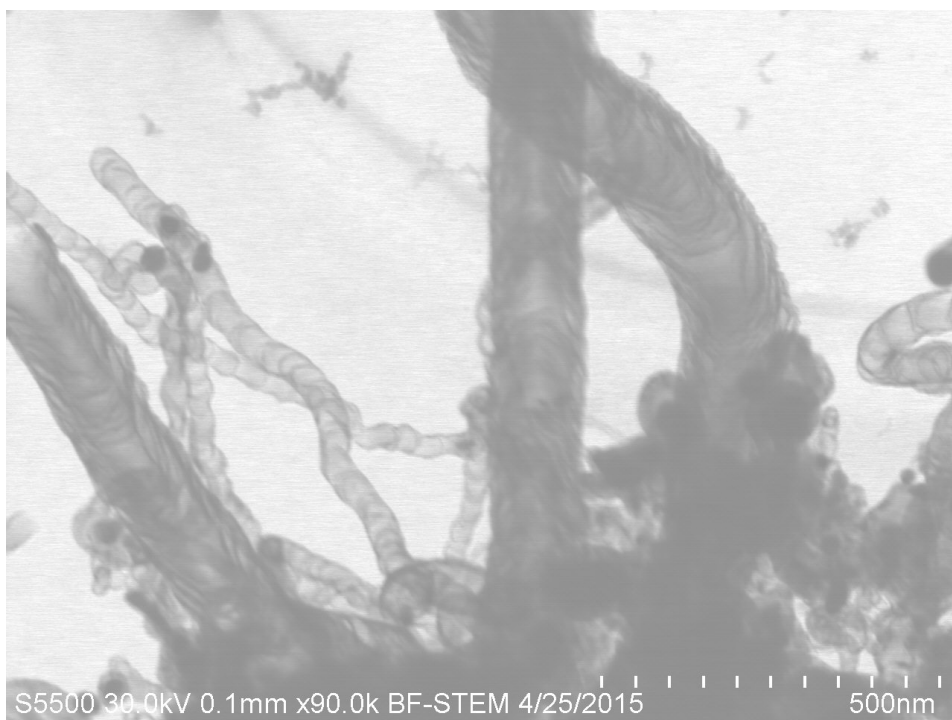
Figure E.7: S(T)EM 200ExG24h: N-CNFs with FeNPs on top and bamboo (in the back) and fishbone structure (in the front).
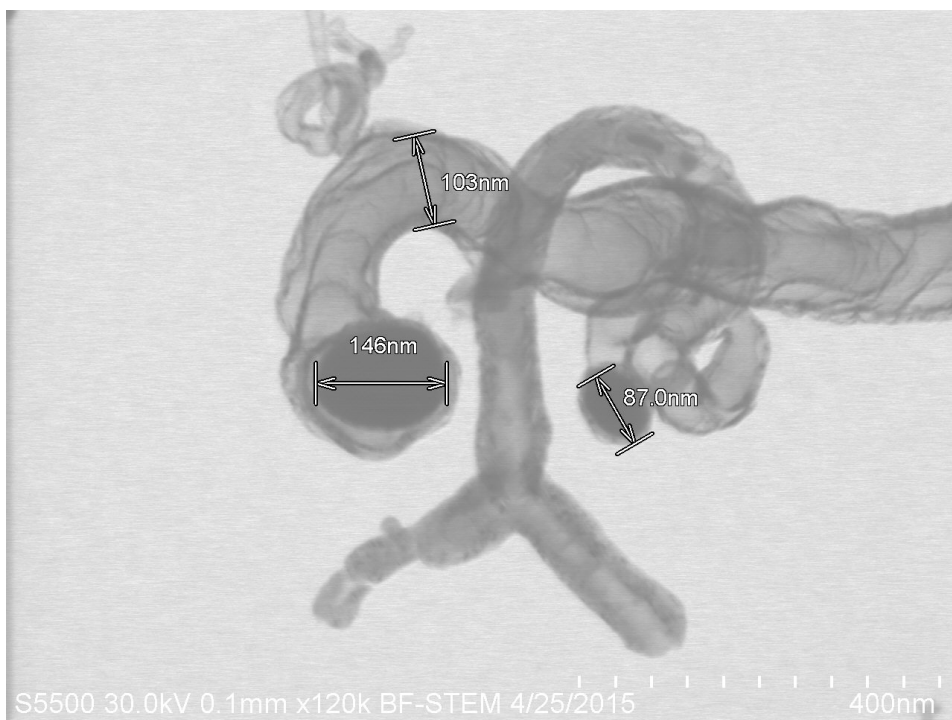
Figure E.8: S(T)EM 200ExG24h: A closeup of Figure 5.18a. Two N-CNFs with indicated FeNP diameter and fiber diameter. The largest N-CNF has tendency towards bamboo structure with clearly visible compartments, and the smaller has a hybrid structure between bamboo and either MWCNT or ribbon.
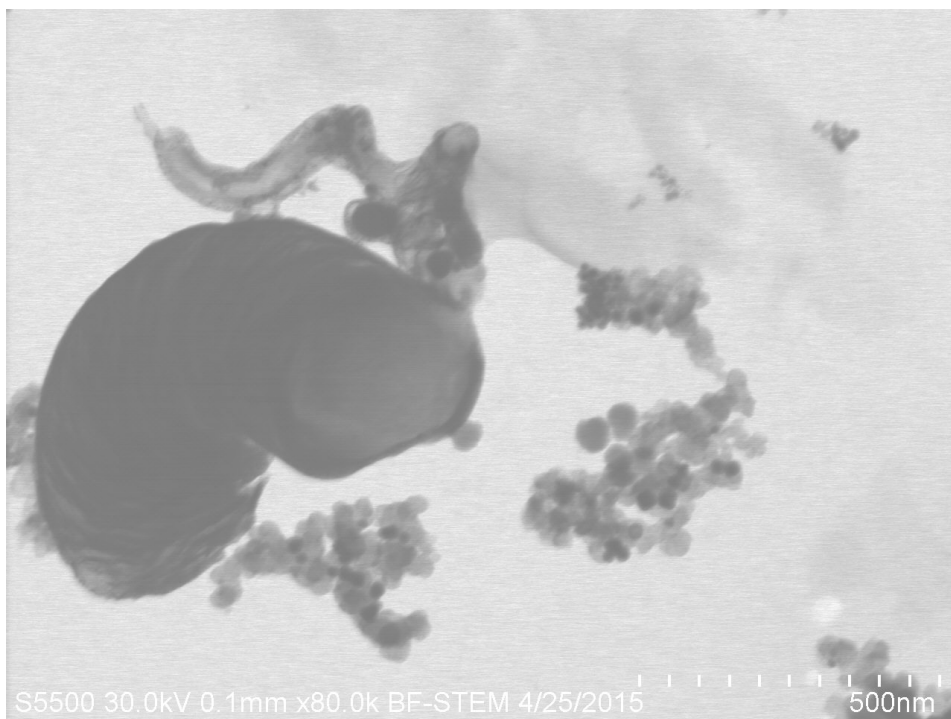
Figure E.9: S(T)EM 200ExG24h: A large thickened N-CNFs, smaller N-CNFs and FeNPs deposited on support.

(a)   (b)
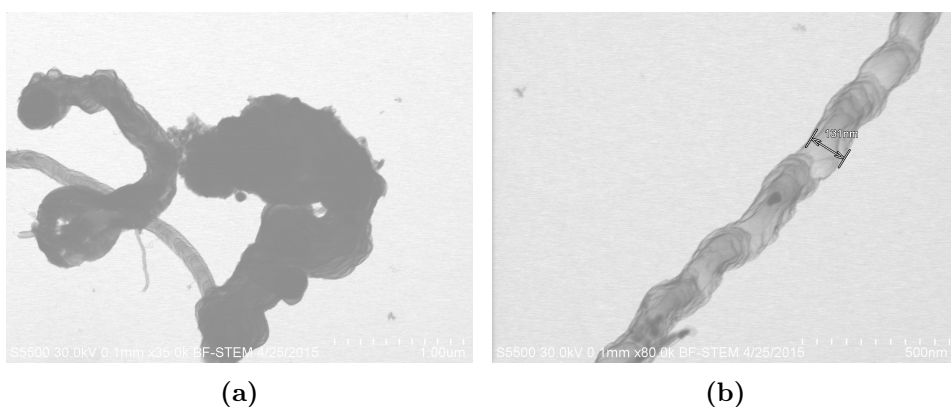
Figure E.10: S(T)EM 200ExG24h: (a) thickened N-CNFs and a bamboo structure (b) bamboo structure with a diameter of 131 nm and an entrapped FeNP.
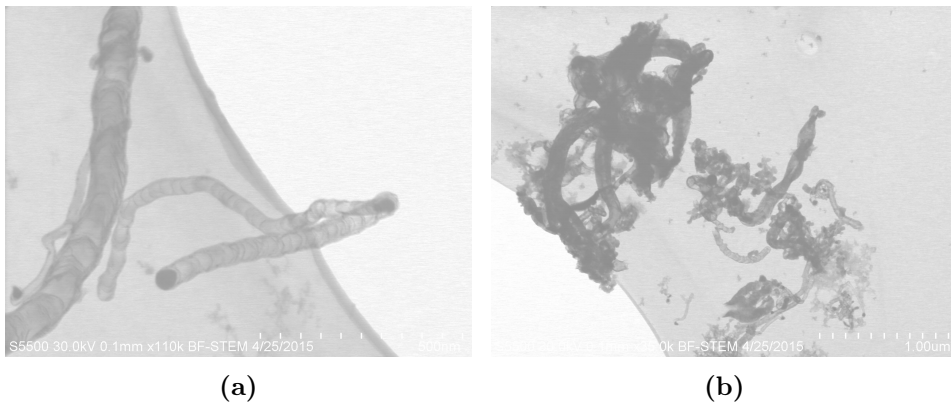
<div align="center">(a)   (b)</div>

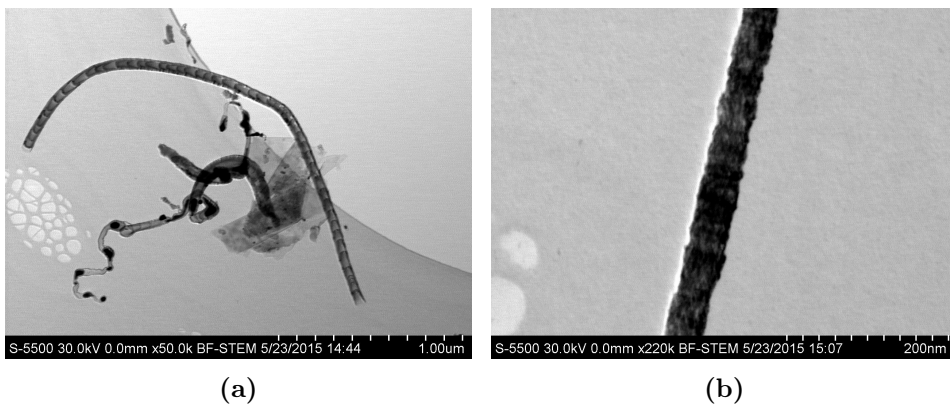**Figure E.11:** S(T)EM 200ExG24h: (a) bamboo structure (b) thickened N-CNFs, bamboo and MWCNTs.

E.5 ExGM24h

(a)   (b)

Figure E.12: S(T)EM ExGM24h: (a) bamboo structure and a grahpite flake (b) fishbone structure.
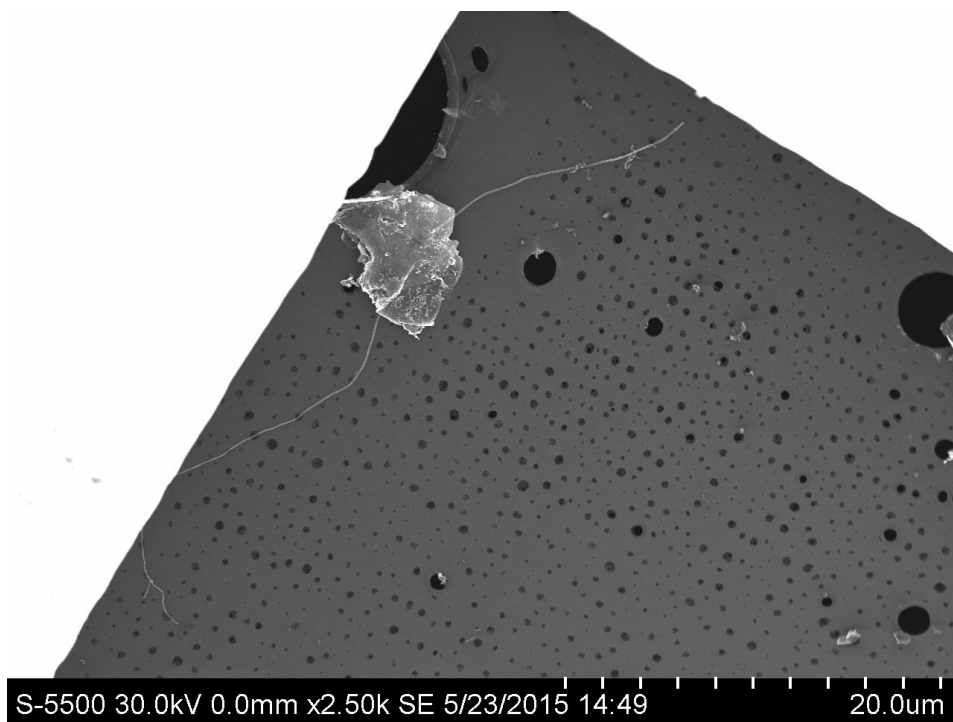
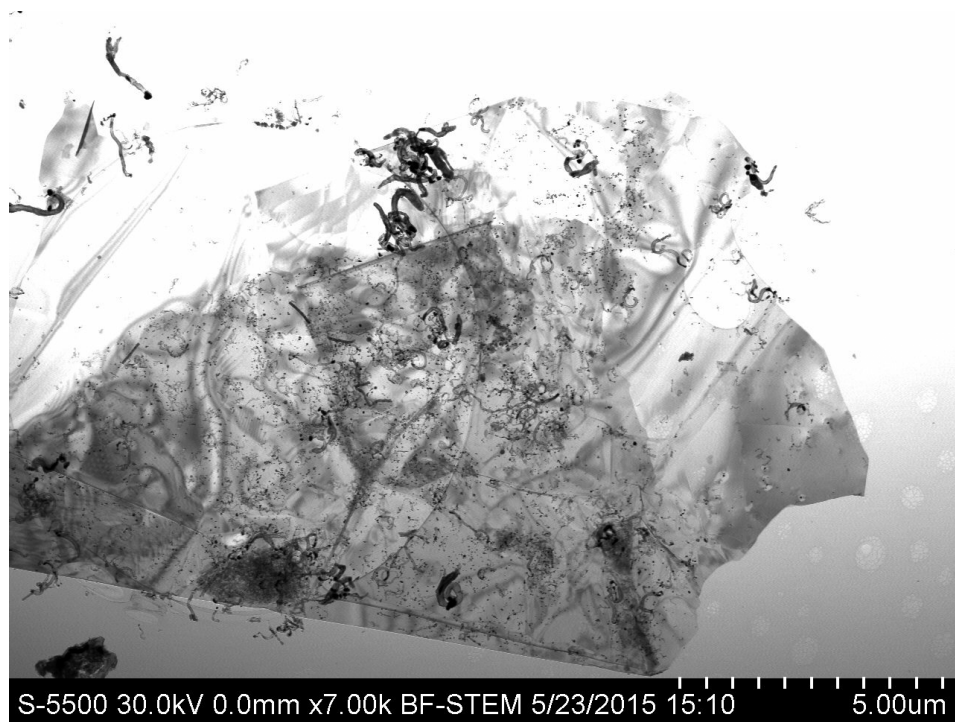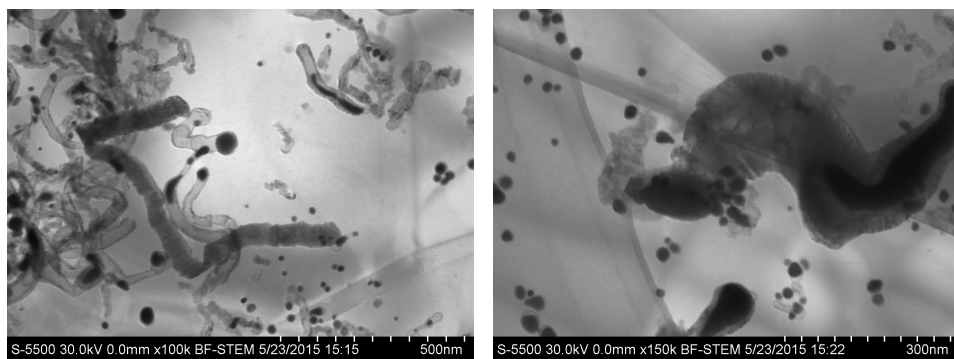**Figure E.13:** S(T)EM ExGM24h: a 40 µm long N-CNF with bamboo structure.

S-5500 30.0kV 0.0mm x7.00k BF-STEM 5/23/2015 15:10   5.00um

Figure E.14: S(T)EM ExGM24h: N-CNFs on support. An overview of Figure E.13 .

S-5500 30.0kV 0.0mm x100k BF-STEM 5/23/2015 15:15   500nm

S-5500 30.0kV 0.0mm x150k BF-STEM 5/23/2015 15:22   300nm

(a)   **(b)**

Figure E.15: S(T)EM ExGM24h: (a) platelet, MWCNT and bamboo structure (b) MWCNT with molten particle.

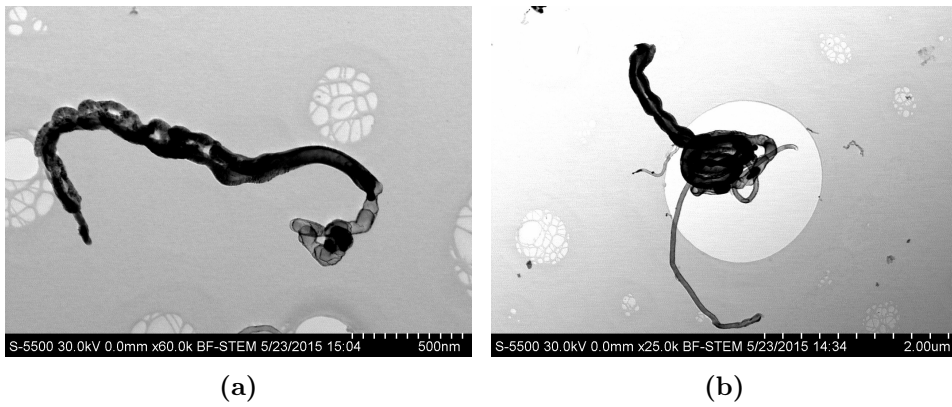(a)   (b)

Figure E.16: S(T)EM ExGM24h: Two distorted structures (a) bamboo at top
together with a iron particle and a thickened fiber at the end (b)
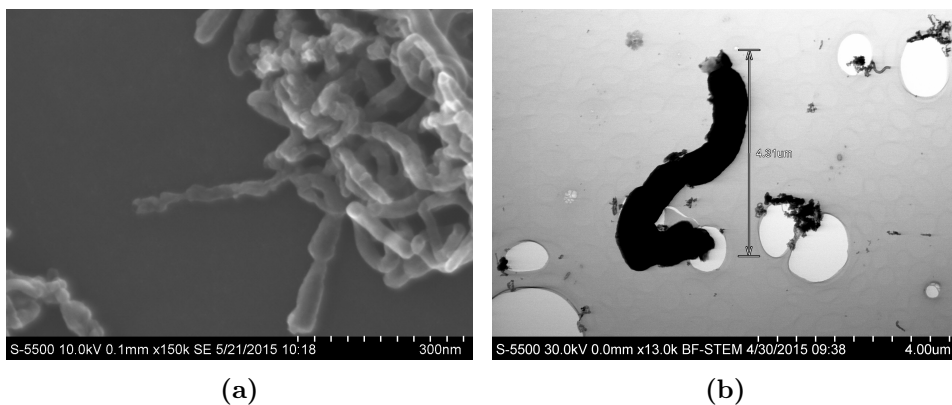fishbone structure together with a curved thickened MWCNT.

E.6   200Vu24h

<div align="center">(a)</div>

<div align="center">(b)</div>

Figure E.17: 200Vu24h: (a) small fibers with strange strucutre , (b) a thick N-CNFs with a length of 4.31 μm and a diameter of 820 nm
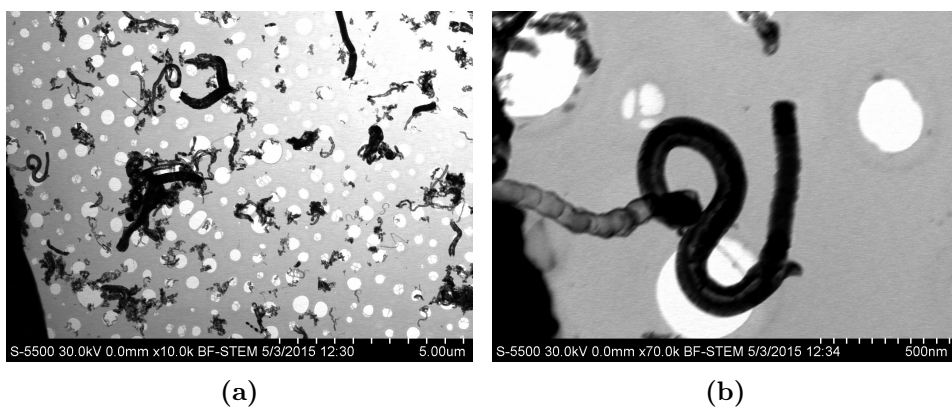
E.7   VuM24h

<div align="center">(a)</div>

<div align="center">(b)</div>

Figure E.18: S(T)EM VuM24h: (a) an overview of the sample (b) two fibers with bamboo structure and MWCNT.
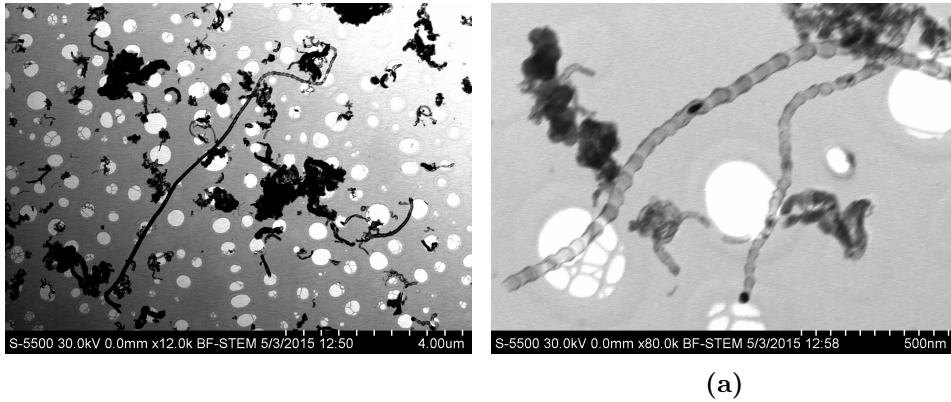
(a)

Figure E.19: S(T)EM VuM24h: (a) 7.49 μm long N-CNF with bamboo structure at the top and fishbone at the end (b) two N-CNFs with bamboo structure.

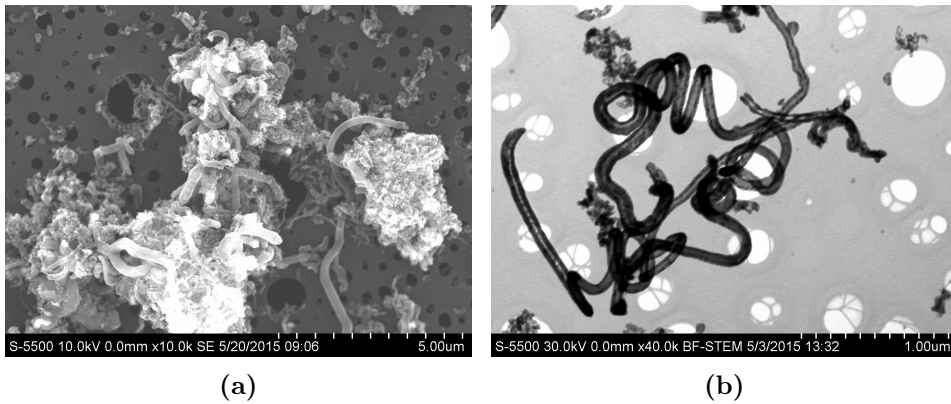**(a)** **(b)**

Figure E.20: S(T)EM VuM24h: (a) SE image of N-CNFs on support (b) long coiled MWCNT fiber.
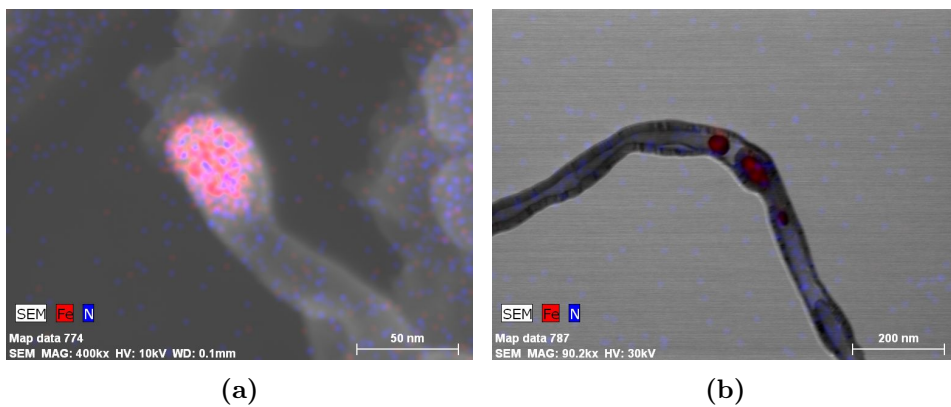
E.8   EDX

Figure E.21: EDX (a) 200Vu24h: a FeNP on the tip of a N-CNF, (b) ExGM24h: an EDX scan of Figure 5.21a.

Individual linear sweep voltammogram

This appendix illustrates the individual inear sweep voltagrammogram for all samples, including the background, disk and corrected measurements.
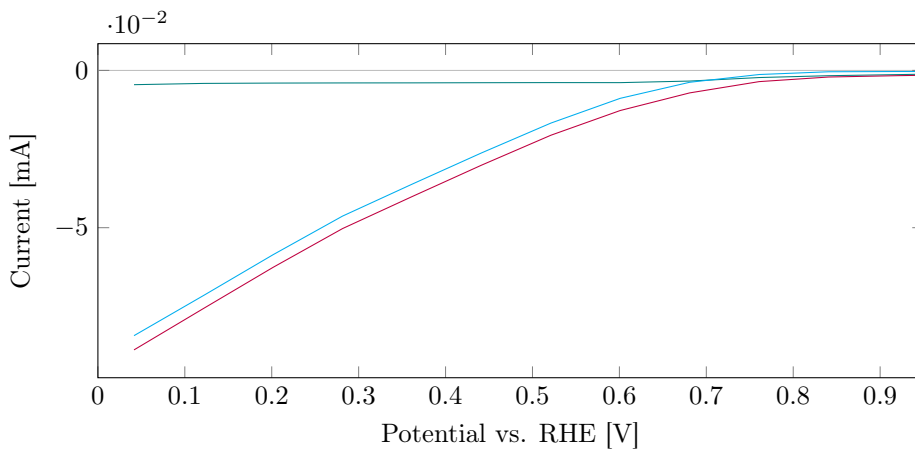
F.1   200Fe24h

Figure F.1: Linear sweep voltagrammogram 200Fe24h: background ——,
disk ——, corrected ——. The measurements were performed at a
scan rate of $5\,\mathrm{mV/s}$ and a rotation rate of $1600\,\mathrm{rpm}$ in a O_2 satu-
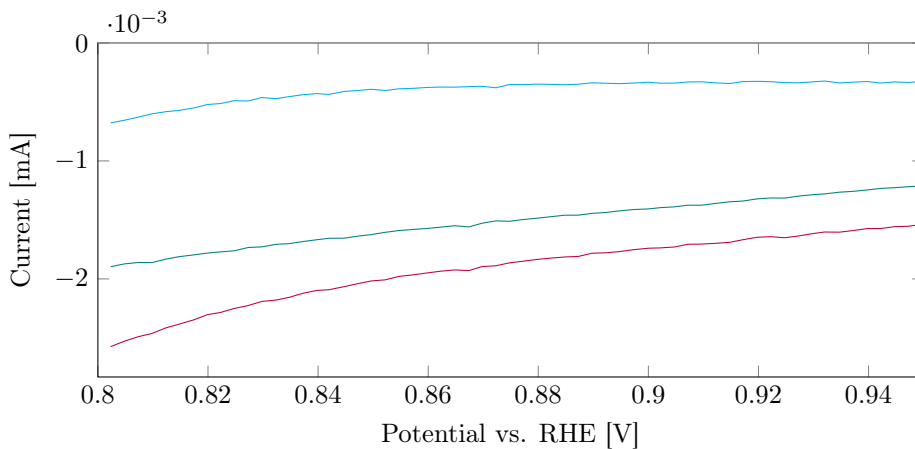rated electrolyte.

Figure F.2: Linear sweep voltagrammogram close up 200Fe24h: background ——,
disk ——, corrected ——. The measurements were performed at a
scan rate of $5\,\mathrm{mV/s}$ and a rotation rate of $1600\,\mathrm{rpm}$ in a O_2 saturated
electrolyte.

F.2   200ExG24h

Figure F.3: Linear sweep voltagrammogram 200ExG24h: background ———,
disk ———, corrected ———. The measurements were performed at a
scan rate of $5\,\mathrm{mV/s}$ and a rotation rate of $1600\,\mathrm{rpm}$ in a O_2 satu-
rated electrolyte.

Figure F.4: Linear sweep voltagrammogram close up 200ExG24h: back-
ground ———, disk ———, corrected ———. The measurements were per-
formed at a scan rate of $5\,\mathrm{mV/s}$ and a rotation rate of $1600\,\mathrm{rpm}$ in a
O_2 saturated electrolyte.

F.3   ExGM24h

Figure F.5: Linear sweep voltagrammogram ExGM24h: background ⎯⎯,
disk ⎯⎯, corrected ⎯⎯. The measurements were performed at a
scan rate of $5\,\mathrm{mV/s}$ and a rotation rate of $1600\,\mathrm{rpm}$ in a O_2 satu-
rated electrolyte.

Figure F.6: Linear sweep voltagrammogram close up ExGM24h: back-
ground ⎯⎯, disk ⎯⎯, corrected ⎯⎯. The measurements were per-
formed at a scan rate of $5\,\mathrm{mV/s}$ and a rotation rate of $1600\,\mathrm{rpm}$ in a
O_2 saturated electrolyte.

F.4   200Vu24h

Figure F.7: Linear sweep voltagrammogram 200Vu24h: background ——,
disk ——, corrected ——. The measurements were performed at a
scan rate of $5\,mV/s$ and a rotation rate of $1600\,rpm$ in a O_2 satu-
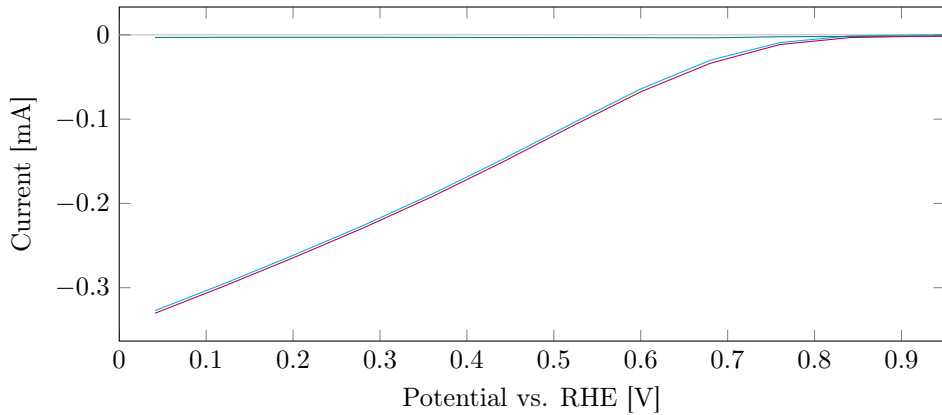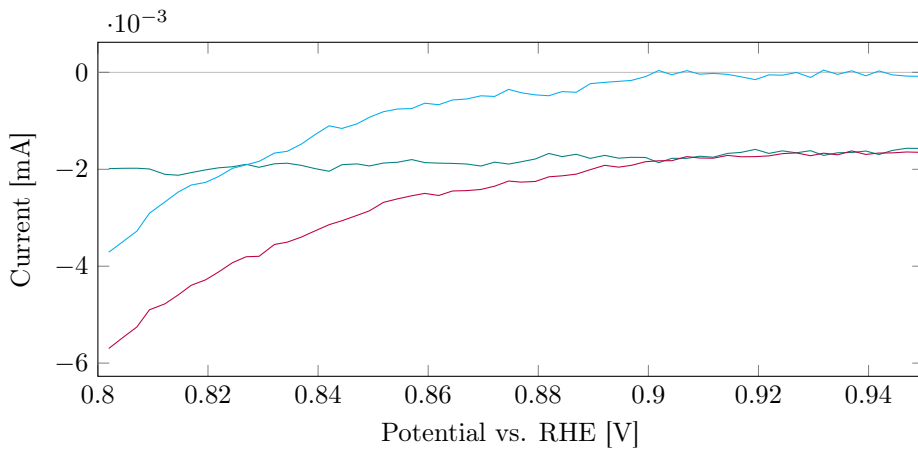rated electrolyte.

Figure F.8: Linear sweep voltagrammogram close up 200Vu24h: back-
ground ——, disk ——, corrected ——. The measurements were per-
formed at a scan rate of $5\,mV/s$ and a rotation rate of $1600\,rpm$ in a
O_2 saturated electrolyte.
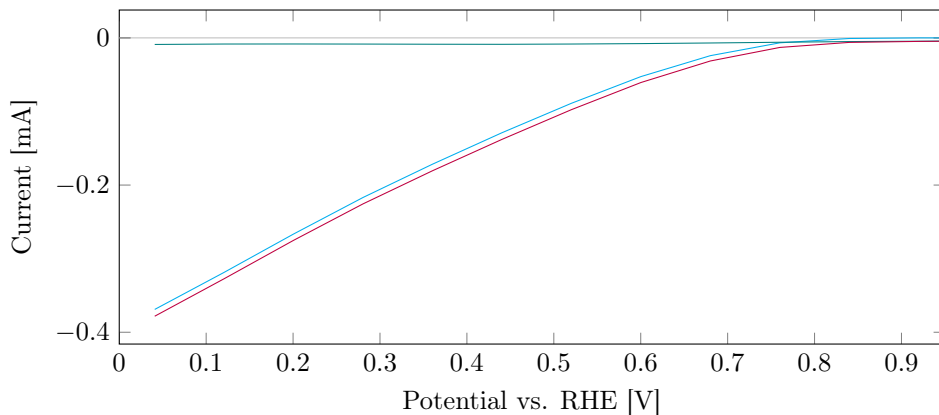
F.5   VuM24h

Figure F.9: Linear sweep voltagrammogram VuM24h: background ——,
disk ——, corrected ——. The measurements were performed at a
scan rate of 5 mV/s and a rotation rate of 1600 rpm in a O_2 satu-
rated electrolyte.

Figure F.10: Linear sweep voltagrammogram close up VuM24h: back-
ground ——, disk ——, corrected ——. The measurements were
performed at a scan rate of 5 mV/s and a rotation rate of 1600 rpm
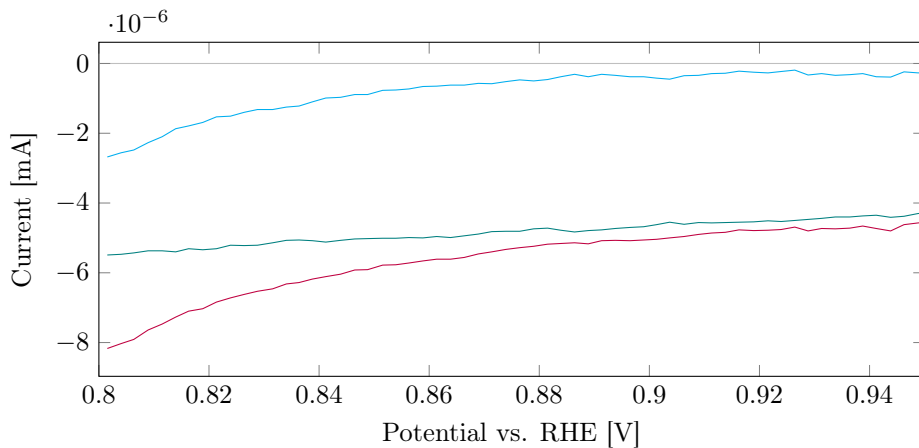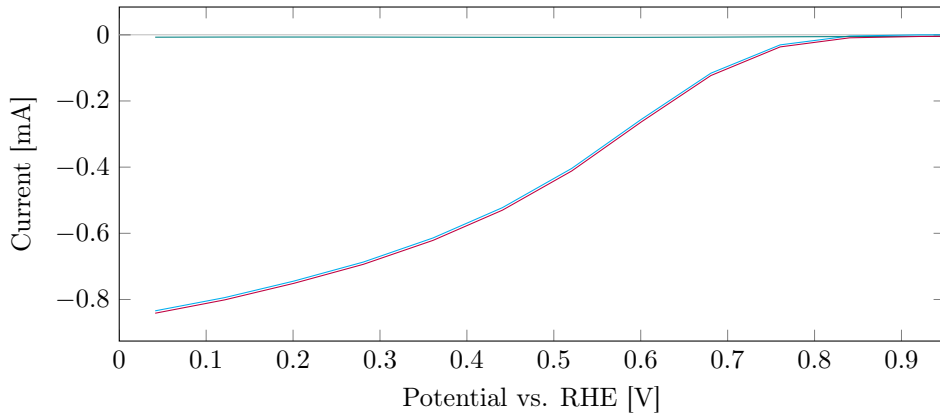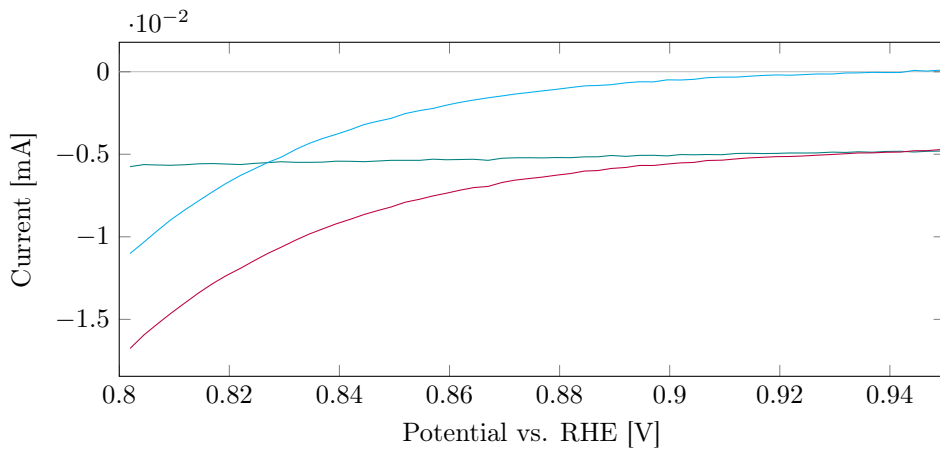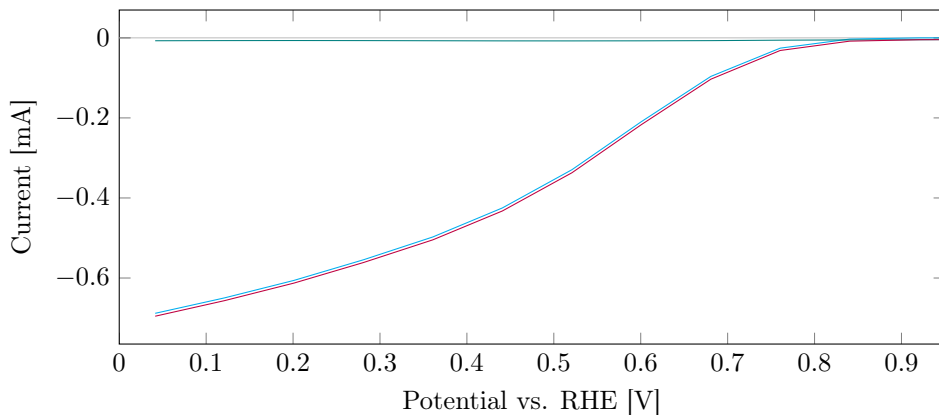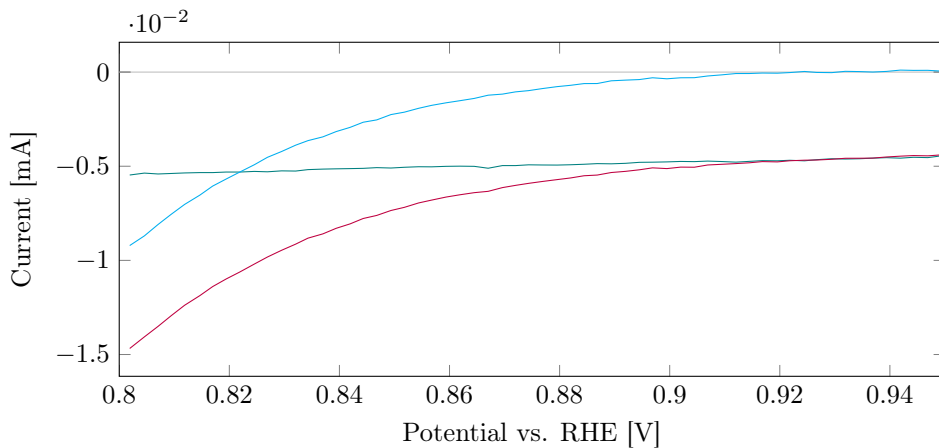in a O_2 saturated electrolyte.

Appendix G

Risk assessment

NTNU		
	Prepared by	Number	Date
	HSE section	HMSRV-26/01	01.12.2006
	Approved by	Page	Replaces
HSE	The Rector	1 out of 2	15.12.2003

Hazardous activity identification process

Unit: **Chemical Engineering**   **Date: 23.01.2015**

Line Manager: **Edd Anders Blekkan**

Participants in the identification process (including their function):
Magnus Rønning, Anne Helene Barsnes, Marthe Emelie Buan,
Navaneethan Muthuswamy, Karin Wigen Dragsten

(supervisor, student, co-supervisor, others)

Short description of the main activity/main process: **Master project for student Anne Helene Barsnes,**
Project title: Doped carbon nanostructures as metal-free
catalysts in the oxygen reduction reaction

Signatures: **Responsible supervisor:** _____   **Student:** _____

ID nr.	Activity/process	Responsible person	Laws, regulations etc.	Existing documentation	Existing safety measures	Comment
1	Synthesis of nitrogen-doped carbon nanofibers	Anne Helene Barsnes	AIML	Apparatus card, safety datasheet	Safety goggles, protective cloves, lab coat	
2	Catalyst characterization (BET)	Anne Helene Barsnes	AIML	Apparatus card, safety datasheet	Safety goggles, nitrile cloves, lab coat	
3	Catalyst characterization (TGA)	Anne Helene Barsnes	AIML	Apparatus card, safety datasheet	Safety goggles, protective cloves, lab coat, gas detector system	
4	Synthesis of iron nanoparticles	Anne Helene Barsnes	AIML	Safety datasheet, procedure	Safety goggles, protective cloves, lab coat,	Executet at Nanolab

NTNU		Prepared by		Number	Date	
● HSE	Hazardous activity identification process	HSE section		HMSRV-26/01	01.12.2006	
		Approved by		Page	Replaces	
		The Rector		2 out of 2	15.12.2003	

5	Scanning transmission electron microscop (STEM)	Anne Helene Barsnes	AIML	Apparatus card, safety datasheet	Safety goggles, protective cloves, lab coat	Executet at Nanolab
6	Electrochemical characterization of carbon nanostructures	Anne Helene Barsnes	AIML	Apparatus card, safety datasheet	Safety goggles, protective cloves, lab coat	Executet at IMT
7	Impregnation of support with iron nanoparticles and iron nitrate	Anne Helene Barsnes	AIML	Apparatus card, safety datasheet	Safety goggles, protective cloves, lab coat	
8	Removing iron from a sample	Anne Helene Barsnes	AIML	Apparatus card, safety datasheet	Safety goggles, protective cloves, lab coat	

NTNU		Prepared by		Number	Date
HSE/KS	Risk assessment	HSE section		HMSRV2603E	04.02.2011
		Approved by		Page	Replaces
		The Rector		3 out of 4	01.12.2006

Unit: Catalysis group, IKP
Line manager: Magnus Rønning
Participants in the risk assessment (including their function): Anne Helene Barsnes

Date: 15.09.14

ID no.	Activity from the identification process form	Potential undesirable incident/strain	Likelihood (1-5)	Consequence: Human (A-E)	Consequence: Environ ment (A-E)	Consequence: Economy/ material (A-E)	Risk value	Comments/status Suggested measures
1	Synthesis of carbon nanostructures	a. Spill of chemicals	3	A			3A	Use safety glasses, lab coat and protectove gloves.
		b. Inhalation of catalyst powder	2	C			2C	Avoid gas leaks by using gas detectors.
		c. Inhalation of CO	2	B			2B	Use a dust mask when handling the catalyst powder.
		d.						
2	Characterization of the catalyst - BET	a. Spill of liquid nitrogen	2	B			2B	Use safety glasses, lab coat and protective gloves
		b. Inhalation of catalyst powder	2	B			2B	
3	Characterization of the catalyst - TGA	a. Hot parts	3	A			3A	Make sure that all parts have cooled down before touching anything.
4	Synthesis of iron nanoparticle	a. Spill of chemicals	3	A			3A	Use safety glasses, lab coat and protective gloves and work in a fume hood.
		b. Inhalation of gases	1	B			1B	
		c. Exposure of skin and eyes to gases	1	B			1B	
		d. Inhalation of iron nanoparticles	2	B			2B	Training was provided by Gurvinder Singh.
5	Scanning transmission electron microscop (STEM)	a. Electromagnetic fields	1	B			1B	Training was provided by Nanolab
		b. High voltage	1	E			1E	
6	Electrochemical characterization of carbon nanostructures	a. Spill of chemicals	3	A			3A	Use safety glasses, lab coat and nitrile gloves.
		b. Spill of acid	3	C			3C	Use a dust mask and work in a fume hood.
		c. Inhalation of catalyst powder and fumes	2	B			2B	Keep the potentiostat off when
			1	C			1C	

NTNU HSE/KS	Risk assessment	Prepared by	Number	Date
		HSE section	HMSRV2603E	04.02.2011
		Approved by	Page	Replaces
		The Rector	4 out of 4	01.12.2006

		c. Electrical shock from potentiostat				connecting. Training was provided by Marthe Buan
7	Impregnation of support with iron nanoparticles and iron nitrate	a. Inhalation of support	1	B	1B	Use safety glasses, lab coat and protective gloves and work in a fume hood.
		b. Spill of chemicals	3	A	3A	
8	Removing iron from a sample	a. Spill of acid	3	B	3C	Use safety glasses, lab coat and protective gloves and work in a fume hood.
		b. Fire damage from an oil bath	2	B	3B	

Likelihood, e.g.:
1. *Minimal*
2. *Low*
3. *Medium*
4. *High*
5. *Very high*

Consequence, e.g.:
A. *Safe*
B. *Relatively safe*
C. *Dangerous*
D. *Critical*
E. *Very critical*

Risk value (each one to be estimated separately):
Human = Likelihood x Human Consequence
Environmental = Likelihood x Environmental consequence
Financial/material = Likelihood x Consequence for Economy/materiel

Potential undesirable incident/strain

Identify possible incidents and conditions that may lead to situations that pose a hazard to people, the environment and any materiel/equipment involved.

Criteria for the assessment of likelihood and consequence in relation to fieldwork

Each activity is assessed according to a worst-case scenario. Likelihood and consequence are to be assessed separately for each potential undesirable incident. Before starting on the quantification, the participants should agree what they understand by the assessment criteria:

Likelihood

Minimal 1	Low 2	Medium 3	High 4	Very high 5
Once every 50 years or less	Once every 10 years or less	Once a year or less	Once a month or less	Once a week

Consequence

Grading	Human	Environment	Financial/material
E Very critical	May produce fatality/ies	Very prolonged, non-reversible damage	Shutdown of work >1 year.
D	Permanent injury, may produce	Prolonged damage. Long	Shutdown of work 0.5-1 year.

NTNU

HSE/KS

Risk assessment

Prepared by	Number	Date
HSE section	HMSRV2603E	04.02.2011
Approved by	Page	Replaces
The Rector	5 out of 4	01.12.2006

Critical	serious serious health damage/sickness	recovery time.
C Dangerous	Serious personal injury	Minor damage. Long recovery time	Shutdown of work < 1 month
B Relatively safe	Injury that requires medical treatment	Minor damage. Short recovery time	Shutdown of work < 1week
A Safe	Injury that requires first aid	Insignificant damage. Short recovery time	Shutdown of work < 1day

The unit makes its own decision as to whether opting to fill in or not consequences for economy/materiel, for example if the unit is going to use particularly valuable equipment. It is up to the individual unit to choose the assessment criteria for this column.

Risk = Likelihood x Consequence
Please calculate the risk value for "Human", "Environment" and, if chosen, "Economy/materiel", separately.

About the column "Comments/status, suggested preventative and corrective measures":
Measures can impact on both likelihood and consequences. Prioritise measures that can prevent the incident from occurring; in other words, likelihood-reducing measures are to be prioritised above greater emergency preparedness, i.e. consequence-reducing measures.

MATRIX FOR RISK ASSESSMENTS AT NTNU

CONSEQUENCE					
Very critical (E)					
Critical (D)					
Danger-ous (C)	1c, 2c				
Relativ. safe(B)	1b	1d, 2b			

NTNU	Risk assessment	Prepared by	Number	Date
		HSE section	HMSRV2603E	04.02.2011
		Approved by	Page	Replaces
HSE/KS		The Rector	6 out of 4	01.12.2006

Safe(A)		1a, 2a,3a		
	Minimal	Low	Medium	High	Very high

LIKELIHOOD

Principle over accept criterion. Explanation of colors used in risk matrix.

Farge	Beskrivelse
Rød	Unacceptable risk. Action must be carried out to minimize risk.
Gul	Assessment area. Action must be evaluated.
Grønn	Acceptable risk. Action might be evaluated from other conciderations.